

# **Quantitative Ultrasound Characterization and Monitoring of Locally Advanced Breast Cancer**

**by Hadi Tadayyon**

A thesis submitted in conformity with the requirements  
for the degree of Doctor of Philosophy

**Department of Medical Biophysics  
University of Toronto**

© Copyright Hadi Tadayyon 2015

# Quantitative Ultrasound Characterization and Monitoring of Locally Advanced Breast Cancer

Hadi Tadayyon

Doctor of Philosophy

Department of Medical Biophysics

University of Toronto

2015

## Abstract

Traditional assessment of tumour response to cancer therapy is based on tumour size reduction, which takes several weeks to become clinically significant. In this thesis, novel ultrasound backscatter signal analysis and machine learning techniques were developed to characterize breast tumours and detect early changes correlated to response.

In the first study, tumour cell death was induced in human breast cancer tumour-bearing mice, using human mimicking chemotherapy drugs. Treatment-related changes in quantitative ultrasound (QUS) parameters, including change in average acoustic concentration (AAC) and heterogeneity index, revealed a strong correlation to histologically determined cell death extent ( $r^2=0.64$ ). In the second study, radiofrequency (RF) ultrasound data were acquired from locally advanced breast cancer (LABC) patients prior to treatment. Results suggested that a multiparameter QUS model can sensitively (88%) and specifically (91%) differentiate breast tumours from surrounding normal tissue. Furthermore, a local texture - based QUS model was demonstrated as a promising tumour grade predictor (86% accuracy).

In the final study, ultrasound RF data were acquired from LABC patients prior to treatment, at 3 times during the treatment (weeks 1, 4, 8), and prior to surgery. Tumour response classification analysis using a multiparameter QUS model of midband fit (MBF), spectral slope (SS), and spacing among scatterers (SAS) demonstrated desirable classification performance at 4 weeks into treatment ( $80 \pm 5\%$ ). Secondly, the QUS classification model demonstrated a significant difference in survival rates of responding and nonresponding patients at weeks 1 and 4 ( $p=0.035$ , and  $0.027$ , respectively).

In summary, the incorporation of QUS assessment of the breast during or after an ultrasound-guided breast biopsy session may potentially permit cross-verification of the histopathological findings. Furthermore, patients undergoing neoadjuvant chemotherapy can potentially benefit from a weekly QUS assessment in order to evaluate their early tumour response so that the appropriate treatment intervention can be made if the patient was nonresponding.

## Acknowledgements

The primary acknowledgement and gratitude extends to Dr. Gregory Czarnota, who provided valuable scientific ideas, guidance, and feedback throughout my thesis work and used enthusiastic words such as “good work” with every progress I made. I would like to also extend my gratitude toward my senior lab members and colleagues, Ali Sadeghi-Naini, Lakshmanan Sannachi, and Mehrdad Gangeh, for their valuable help in data analysis methodologies and fruitful scientific discussions. I also greatly benefited from the help of Azza Al-Mahrouki with optical microscopy, histological data interpretation, and insightful biology discussions.

I would like to also extend a general thank-you to all members of the Czarnota lab as supportive colleagues and friends, who made my time in the lab enjoyable. I found the scientific lab meetings and occasional social gatherings to be a great experience. My experience with my lab mates demonstrated that regular scientific and social discussions (during breaks) are necessary for the morale and well-being of a researcher.

A vital component of my research success was my PhD committee, consisting of Dr. Michael Kolios, Dr. Anne Martel, and Dr. Greg Stanisz. With their critical examination of my progress and constructive feedback, I grew as a researcher and a critical thinker. Dr. Michael Oelze at the University of Illinois was also a part of my PhD success, who kindly shared his laboratory’s MATLAB program for quantitative ultrasound analysis and with whom I had fruitful discussions about quantitative ultrasound scattering models and its application to cell death detection.

I would like to also extend my gratitude toward my family, including my father Mohammad Tadayyon, mother, Marzieh Sari Aslani, sister, Hoda Tadayon, and wife, Narges Nooripoor for their unconditional love and companionship in both good and hard times during my PhD journey. This thesis was partially supported by NSERC Alexander Graham Bell Postgraduate Scholarship.

## List of Abbreviations

AAC	Average acoustic concentration
AI	Apoptotic Index
ACE	Attenuation coefficient estimate
AR	Autoregressive model
ASD	Average scatterer diameter
BSC	Backscatter coefficient
CDF	Cell death fraction
CON	Contrast texture feature
COR	Correlation texture feature
dBr	Decibels relative to reference
DCE-MRI	Dynamic contrast enhanced MRI
DOI	Diffuse Optical Imaging
DW-MRI	Diffusion-weighted MRI
ENE	Energy texture feature
ER	Estrogen receptor
FDG	Fluoro-deoxyglucose
FF	Form factor (scattering model)
FFSM	Fluid-filled sphere model
FFT	Fast Fourier transform
GLCM	Grey-level co-occurrence matrix
HER2	Human epithelial growth factor receptor 2
HI	Heterogeneity index
HOM	Homogeneity texture feature
ISEL	In situ end labeling
KNN	K nearest neighbour
LABC	Locally Advanced Breast Cancer
MASD	Minimum average standard deviation
MBF	Midband-fit of power spectrum
MRI	Magnetic Resonance Imaging
PET	Position emission tomography

PR	Progesterone receptor
QUIS	Quantitative ultrasound
RECIST	Response Evaluation Criteria in Solid Tumours
ROC	Receiver-operator characteristics
ROI	Region of interest
RF	Radiofrequency
SAC	Spectral autocorrelation
SAS	Spacing among scatterers
SGM	Spherical Gaussian model
SI	Spectral intercept (0-MHz intercept)
SS	Spectral slope
TUNEL	Terminal deoxynucleotidyl transferase deoxyuridine-triphosphatase nick end labeling

## Contents

Abstract .....	II
Acknowledgements .....	IV
List of Abbreviations .....	V
List of Tables .....	X
List of Figures .....	XII
1 Introduction .....	1
1.1 Overview of locally advanced breast cancer management .....	2
1.2 Cancer therapy response assessment and the role of ultrasound .....	3
1.3 Basic principles of ultrasonic scattering in biological tissues .....	5
1.4 Ultrasound radiofrequency spectrum .....	7
1.5 Scatterer spacing estimation using spectral autocorrelation .....	9
1.6 The backscatter coefficient and estimation of its parameters .....	12
1.7 Frequency-dependent acoustic attenuation .....	13
1.8 Statistical texture analysis .....	15
1.9 Ultrasound detection of cell death .....	17
1.10 Quantitative ultrasound parameters investigated .....	22
1.11 Thesis overview and hypothesis .....	23
2 Correlation between QUS and cell death <i>in vivo</i> at the clinically relevant frequency range ...	26
2.1 Overview .....	27
2.2 Introduction .....	28
2.3 Methods .....	31
2.3.1 Experimental procedures .....	31
2.3.2 Quantitative ultrasound analysis .....	32
2.3.3 Histology analysis .....	33

2.3.4 Statistical Analysis.....	34
2.4 Results.....	35
2.4.1 Histological assessment of treatment effects .....	35
2.4.2 Tumour volume analysis.....	37
2.4.3 Tissue microstructure models .....	37
2.4.4 Ultrasonic scattering properties of cell death.....	42
2.5 Discussion and Conclusions .....	47
3 Quantitative ultrasound characterization of locally advanced breast cancer .....	51
3.1 Overview.....	52
3.2 Introduction.....	53
3.3 Methods.....	55
3.3.1 Overview.....	55
3.3.2 Ultrasound data acquisition and processing.....	56
3.3.3 Quantitative ultrasound analysis .....	59
3.3.4 Statistical textural analysis of quantitative ultrasound maps .....	59
3.3.5 Tissue classification algorithm .....	60
3.4 Results.....	61
3.4.1 QUS analysis of tumour versus normal tissue .....	61
3.4.2 QUS analysis of tumour grades .....	63
3.5 Discussion.....	69
4 Quantitative ultrasound assessment of breast tumour response to chemotherapy .....	72
4.1 Overview.....	73
4.2 Introduction.....	74
4.3 Methods.....	76
4.3.1 Ultrasound data acquisition and processing.....	76
4.3.2 Quantitative ultrasound data analysis .....	77

4.3.3 Classification and statistical analyses .....	78
4.4 Results.....	79
4.5 Discussion.....	91
5 Summary and future directions .....	95
5.1 Summary and conclusions of thesis.....	96
5.2 Future directions .....	98
Appendix.....	102
Analytical solution for the scattering from solid spheres .....	103
Patient characteristics.....	106
Transducer characterization and validation of scatterer size and attenuation estimation .....	112
Overview and background .....	112
Methods.....	113
Ultrasound imaging systems .....	113
Transducer characterization .....	113
Phantom construction.....	114
Attenuation coefficient estimation <i>in vivo</i> .....	115
Backscatter coefficient and scatterer size estimation.....	115
Results .....	116
Transducer characterization .....	116
Attenuation coefficient estimation <i>in vivo</i> .....	117
Backscatter coefficient and scatterer size estimation <i>in vivo</i> .....	118
Discussion .....	126
References .....	127

## List of Tables

Table 1-1. Investigated QUS parameters, their definition, and their link to biology. ....	22
Table 2-1. Comparison of ASDs ( $\mu\text{m}$ ) and AACs ( $\text{dBr/cm}^3$ ) estimated using the SGM and FFSM models at low and high frequencies (LF and HF) with mean histological measurement of tumour cell size. $R^2$ is a measure of the goodness-of-fit of the model BSCs to the measured BSCs. $\pm$ represents standard deviations of the parameter over the tumour samples. Estimates were obtained from all tumours prior to treatment. ....	39
Table 2-2. Stepwise multiple regression results. The second column presents the standardized coefficient of each model and the third column presents the model's correlation to CDF ( $r^2$ ) ....	43
Table 2-3. Stepwise multiple regression results for the two cases - with and without tumour volume normalization (separated by a horizontal line). The second column presents the standardized coefficient of each parameter and the third column presents the parameter's correlation to CDF ( $r^2$ ). NS indicates non-significant results ( $p>0.05$ ). ....	44
Table 3-1. Patient characteristics. ER is estrogen receptor, PR is progesterone receptor, HER2 is the human epithelial growth factor receptor 2, IDC is invasive ductal carcinoma, and IMC is invasive micropapillary carcinoma. Tumour size refers to the longest diameter of the tumour...	58
Table 3-2. Classifier performances using different combinations of advanced QUS parameters for tumour versus normal tissue classification - (ASD, AAC), (ASD, SAS), (AAC, SAS) and (ASD, AAC, SAS). AUC - area under the ROC curve.....	63
Table 3-3. Summary of classification performances for optimal parameters obtained from sequential feature selection from all means, all textures, and all means and textures. All results were obtained by leave-one-out cross-validation. ....	65
Table 3-4. Discriminant function structure vector for optimal QUS means and textures. Coefficients represent the correlation between each parameter and the obtained discriminant function. Parameters are listed in order of decreasing absolute coefficient. ....	66
Table 4-1. Summary of patient characteristics. IDC = invasive ductal carcinoma, ILC = Invasive lobular carcinoma, BTS = bulk tumour shrinkage (percent change in tumour size). ....	84

Table 4-2. A comparison of the classification performances (accuracy) of different QUS parameters using the KNN classifier, at weeks 1, 4 and 8. The bold entry indicates the best performance. Reported values are mean and standard deviation of the accuracies obtained by running the classification 10 times using 10 random samples of responders.....	88
Table 4-3. A comparison of the classification results obtained based on tumour size alone (RECIST criteria), based on changes in QUS parameters, and based on changes in QUS parameters plus week 0 QUS parameters. $\Delta$ QUS represents [ $\Delta$ MBF $\Delta$ SS $\Delta$ SAS] and QUS <sub>w0</sub> represents [MBF <sub>w0</sub> SS <sub>w0</sub> SAS <sub>w0</sub> ]. The last row presents the p-value significance of the difference between the mean accuracies of $\Delta$ QUS and $\Delta$ QUS + QUS <sub>w0</sub> models. Reported values are mean and standard deviation of the accuracies obtained by running the classification 10 times using 10 bootstrap samples from responder group. For QUS results, sensitivity and specificity numbers have denominator of 16 and accuracy numbers have denominator of 32.....	88
Table 4-4. Clinical/histopathological characteristics of misclassified patients at week 4. The majority were HER2 negative patients (indicated in bold), and the few HER2 positive patients (indicated in italics) all received HER2 receptor-targeted treatments such as Herceptin and Trastuzumab.....	90

## List of Figures

- Figure 1-1. A schematic plot of the normalized power spectrum with linear regression applied to the – 6dB transducer bandwidth (4.5 – 9 MHz). dBr is defined as decibels relative to reference. Adapted from [36]..... 8
- Figure 1-2. (A) Typical power spectrum estimated using the AR model from a human breast tumour. (B) Corresponding spectral autocorrelation functions for different AR model order ( $p = 10-100$ ). At lower orders ( $p < 50$ ), no peaks can be detected. At  $p = 100$ , false peaks appear..... 11
- Figure 1-3. Signals used in the measurement of frequency dependent attenuation. The sample is sandwiched between a thin mylar membrane and a quartz optical flat. By measuring the RF signal, both with (b) and without (a) the sample present, it is possible to compute the frequency dependent attenuation coefficient which is based on the ratio of the magnitude spectra of these two signals. Adapted from [42]. ..... 15
- Figure 1-4. Process of GLCM computation. The left matrix is an 3-bit grayscale image and the right matrix is the corresponding GLCM constructed using a distance of one pixel and an angle of  $0^0$ . Adapted from [47]. ..... 16
- Figure 1-5. Integrated backscatter coefficient versus nuclear diameter of a cell. The data were acquired from whole cells, with the diameter of the cell nucleus plotted along the x-axis. The square denotes the MT-1 cell line for which the nuclear diameter was measured by visual inspection of the microscopy images of whole cells. Adapted from [43]. ..... 19
- Figure 1-6. Results of photodynamic therapy on *in vivo* xenograft tumours. Tumours were examined using 26-MHz ultrasound before treatment and at different times after administration of PDT ( $n = 3$  animals per time). Ultrasound data collection consisted of acquiring B-scan images (A) in addition to spectroscopic data for quantitative analyses of backscattered ultrasound (B,C). At 24 h, there was an increase in backscatter that was detected in ultrasound images, as well as in spectroscopic data. (D) TUNEL sections at  $40\times$  magnification. Typical changes of apoptosis were observed, including nuclear coalescence and fragmentation, as the function of time. At 48 h, nearly half of the cells in the treated area had lost their nuclei as in a final stage of

apoptotic cell death. These changes explain the detected changes in variables related to the size of scatterers in the tissue by ultrasound. Adapted from [25]. ..... 21

Figure 1-7. Scattering simulation with pseudo-regular spacing of cells. Left: a typical pseudo-regular cell array with random loss of nuclei. This array was used as input data for the simulation. Predictions of the average signal amplitude if, in a random way throughout the cell, a fraction of the nuclei, or its fragments, have disappeared during apoptosis. Adapted from [49].21

Figure 2-1. (A-D) Histology images of representative control, 4-hour, 12-hour, 24-hour, and 48-hour chemotherapy-treated MDA-231 tumours, from left to right, respectively. (A) Low-magnification H&E stained sections. (B) Low-magnification ISEL stained sections (C) High-magnification H& E stained section to highlight nuclear material. (D) High-magnification ISEL section to highlight fragmented DNA. The control tumour features rapidly dividing cells with large nuclei. The treated tumours feature reduced nuclear size (nuclear condensation), fragmented nuclei, and dead cellular components filling the extracellular space (brown stains). The low-magnification scale bar represents 1 mm. The high-magnification scale bar represents 25  $\mu$ m. (E) Plots of mean cell and nucleus diameters versus treatment time (0 to 48 hours), estimated from H& E histology sections. Error bars represent standard error of the mean. (F) Plot of the mean cell death fractions versus time. Error bars represent the standard error across the tumour samples for each time condition. Statistical significance: \* =  $p < 0.05$ . ..... 36

Figure 2-2. Plot of *in vivo* tumour volumes before (pre) and at predefined length of time after chemotherapy injection (post). Percent errors of the initial tumour volumes for each group were 74%, 27%, 40%, 20%, and 67%, for control, 4-hour, 12-hour, 24-hour, and 48-hour groups, respectively. ..... 37

Figure 2-3. Illustration of the spatial distribution of  $R^2$  goodness of fits of the SGM and FFSM models over different tumour areas. Presented are  $R^2$  images overlaid on analyzed tumour ROIs over three tumour cross-sections: upper limb, tumour center, and lower limb. Data is presented from the low-frequency study with (A)  $2 \times 2$  mm RF windows and (B)  $3 \times 3$  mm RF windows.41

Figure 2-4. Combined low and high frequency plots of measured BSC and theoretical BSCs based on the SGM and FFSM models obtained from an animal in the 24-hour treatment group.

Left: pre-treatment. Right: post-treatment. The BSCs were obtained from an RF window at the center of the tumour ROI. Corresponding  $R^2$  goodness of fit values are shown below the plots. 42

Figure 2-5. Pre- and post- treatment (24h) images of the central cross section of a sample MDA-231 tumour which received chemotherapy treatment. (A) and (B) show ASD and AAC images overlaid on the B-mode image obtained from the high-frequency and low frequency systems, respectively, and (C) shows low and high magnification ISEL-stained histology sections of the tumour post treatment. B-mode scale bar represents 2 mm. Low magnification represents 1mm. High magnification represents 25 $\mu$ m..... 45

Figure 2-6. Results of QUS analysis of cell death. (A) Plot of  $\Delta$ AAC versus time from treatment onset obtained using the low and high frequency systems. Error bars represent the standard error across the tumour samples for each time condition. Statistical significance: \* =  $p < 0.05$ . (B) Scatter plot of CDF versus the predictive model ( $\Delta$ AAC,  $\Delta$ HIA<sub>ASD</sub>),  $r^2=0.639$ . (C) Scatter plot of CDF versus the predictive model ( $\Delta$ AAC,  $\Delta$ HIA<sub>ASD</sub>, and  $V_i$ ),  $r^2 = 0.744$ . 47

Figure 3-1. 2-D scatter plot of SAS versus AAC of tumours and normal tissues. The class dividing curve represents the quadratic discriminant function. .... 62

Figure 3-2. Receiver operator characteristics curves for the different parameter sets. Set A: means and textures of MBF, SS, SI, and SAS, plus ACE. Set B: means and textures of ASD, AAC, and SAS, plus ACE. Set C, all parameter means and textures included. .... 67

Figure 3-3. One-dimensional scatter plot of the hybrid QUS Biomarker versus tumour aggressiveness. Each point represents the hybrid QUS value of each patient. The horizontal lines represent the means of the groups..... 67

Figure 3-4. Representative images of grade I, II, and III breast tumours. (A) B-mode images of the tumour regions, where the tumours appear as hypoechoic masses. (B) Corresponding hybrid QUS biomarker images of the tumours obtained from optimized linear combination of original QUS means and textures. A common scale bar was used to include the range for all three tumours (C) Same images as (B) but with the use of individual scale bars to show the tumour heterogeneity (D) Hematoxylin and eosin stained histopathology images of the tumours. Scale bars: 1 cm (US), 100  $\mu$ m (hist). .... 68

Figure 4-1. Representative B-mode images (A), MBF images (B), power spectra (C left) before and 4 weeks after the start of chemotherapy treatment and hematoxylin and eosin histology histology images (C right) of an example responding breast tumour. Data in the left column represent pre-treatment data, obtained prior to treatment initiation, and data in the right column represent week 4 data. US scale bar represents 1 cm, histology scale bar represents 100  $\mu$ m..... 85

Figure 4-2. Representative B-mode images (A), MBF images (B), power spectra (C left) before and 4 weeks after the start of chemotherapy treatment and hematoxylin and eosin histology histology images (C right) of an example nonresponding breast tumour. Data in the left column represent pre-treatment data, obtained prior to treatment initiation, and data in the right column represent week 4 data. US scale bar represents 1 cm, histology scale bar represents 100  $\mu$ m..... 86

Figure 4-3. Comparison between QUS parameters (A-G) and the RECIST-based tumour size reduction (H) for tracking patient tumours during chemotherapy. QUS and RECIST values were averaged over responder (blue diamond) and non-responder (red square) groups, and plotted over the treatment time. Patients were grouped based on their pathological clinical response determined post-chemotherapy. All values were normalized to week 0 by subtraction. Error bars represent standard error of the mean..... 88

Figure 4-4. Kaplan-Meier survival curves for responding (solid line) and nonresponding (dashed line) patients. (A) Patients were classified based on clinical/histopathological information. (B,C,D) Patients were classified based on the QUS biomarkers (including week 0 data) obtained at weeks 1, 4, and 8, respectively..... 89

Figure 5-1. Softvue Ultrasound computed tomography system. The system comprises of over 2000 transducer elements arranged in a ring which operate both in transmission and reflections modes. Adapted from Delphinus Medical Technologies (<http://www.delphinusmt.com/our-technology/softvue-system>) ..... 101

Figure 5-2. Using a patented 360 degree rotating concave ultrasound transducer, SonixEmbrace Research captures realistic, uncompressed images of a breast, while the patient lies in a comfortable, prone position. The system captures gigabytes of raw data, which is ideal for cancer detection research and treatment monitoring. Adapted from Analogic Ultrasound (<http://www.analogicultrasound.com/research/clinical/applications/breast-cancer>) ..... 101

# 1 Introduction

## 1.1 Overview of locally advanced breast cancer management

Breast cancer continues to be the predominant form of cancer affecting Canadian women over the age of 20. In 2013, 23, 800 Canadian women were diagnosed with breast cancer, and an estimated 5000 women died [1]. Locally advanced breast cancer (LABC) is a relatively aggressive subtype of breast cancer that includes stage 3 tumours (T3N0 and T3N1) 5 cm or larger often with involvement of the axillary lymph nodes, skin, and/or chest wall. Despite management efforts using systemic therapy, surgery, and radiotherapy, the prognosis of LABC patients is relatively poor with five-year survival rates below 50% [2]. Women at high risk of having or developing breast cancer are screened with combined mammography and ultrasound [3], and based on the findings, a breast biopsy may be recommended to the patient in order to obtain a definitive diagnosis. As clinical studies have shown, the preferred modality for staging LABC, in addition to biopsy, is magnetic resonance imaging (MRI), owing to its superior ability to visualize extent of disease, multicentricity, and mammographically occult cancers [4]. However, ultrasound is emerging as an adjunct modality for locoregional staging of LABC diseases due its good spatial resolution, cost effectiveness, and availability [5].

LABC is generally inoperable and requires upfront chemotherapy treatment for local and metastatic control and to facilitate breast conserving surgery. LABC is a heterogeneous disease encompassing a wide range from low-grade ER/PR/HER2 positive breast cancers to high-grade ER/PR/HER2 negative breast cancers. The typical management workflow for these patients is neoadjuvant chemotherapy, followed by surgery (lumpectomy or mastectomy), and then by radiation therapy. Chemotherapy is often administered using a combination of taxanes, anthracyclines, fluorouracil, and cyclophosphamide. Taxane drugs are plant-derived drugs that act as microtubule disrupters, thereby inhibiting the process of cell division. Anthracyclines are a bacteria-derived class of drugs that inhibit DNA and RNA synthesis in cells, by intercalating the base pairs of the DNA/RNA strands. Chemotherapy administration is typically fractionated (into cycles) in order to help patients recover from drug effects. The administration schedule is typically once every 2 or 3 weeks and the duration varies from 18 to 24 weeks.

Patients with similar tumour types often respond differently to the same chemotherapy drug; thus, switching to a more aggressive drug as a result of poor response to treatment is not uncommon in LABC patients. Conventional methods of clinical tumour response assessment involve tracking

changes in tumour size (longest diameter) using the guidelines provided by Response Evaluation Criteria in Solid Tumours (RECIST) [6]. This can be achieved by intratreatment measurements of tumour dimensions by clinical examination, X-ray mammography, MRI, and/or conventional ultrasound imaging. However, bulk mass diminishments do not typically occur until several weeks to a few months after treatment initiation, despite cytotoxic effects induced by the treatment [7]. Thus, the introduction of an imaging modality capable of differentiating between responding and nonresponding patients in the first days/weeks of a lengthy treatment regimen, would allow clinicians to rapidly determine the effectiveness of a cancer drug, resulting in improved patient prognosis.

## 1.2 Cancer therapy response assessment and the role of ultrasound

The currently accepted method of response assessment is based on a reduction in the sum of the largest diameters of target lesions or the largest diameter of unifocal disease [6]. However, clinically detectable tumour shrinkage does not typically occur until several weeks to months into treatment. Consequently, imaging assessments of tumour biology and biochemistry have led to the discovery of novel biomarkers that can provide earlier indications of tumour response to therapy [7]. Research in early detection of breast cancer response to anticancer therapy has led to discoveries in both image-based and chemical-based biomarkers. In a prospective clinical study, Chang *et al.* monitored levels of apoptotic index (AI) and Ki-67 in breast cancer patients undergoing chemotherapy through flow cytometric and immunocytochemical analyses of fine needle aspiration samples obtained from the breast tumours [8]. Whereas AI represents the number fraction of apoptotic cells identified through terminal deoxynucleotidyl transferase deoxyuridine-triphosphatase nick end labeling (TUNEL), staining for DNA fragmentation, Ki-67 represents cancer cell proliferation. In that study, an increase in AI after 1-3 days, and a decrease in Ki-67 after 21 days, all significant, were found in responding patients compared to nonresponding ones. In another study by Nishimura et al. [9], a higher Ki-67 index was found to be associated with poorer disease-free survival of breast cancer patients.

As for image-based markers, diffusion-weighted MRI (DW-MRI) has been demonstrated clinically to predict response of breast tumours as early as after 1 cycle of chemotherapy. It is used

to measure the apparent diffusion coefficient corresponding to changes in the Brownian motion of water in the tumour tissue, which is thought to increase in responding tumours due to a decrease in tumour cellularity [10]. Tumours are known to have higher glucose metabolism than other tissues. On this basis, in nuclear imaging, a longitudinal PET imaging study on breast cancer used fluorodeoxyglucose (FDG) contrast agent to enhance the tumour region and track its metabolism during chemotherapy treatment [11]. The study demonstrated that responding tumours could be detectable after one cycle of chemotherapy. Additionally, diffuse optical imaging (DOI) studies on breast cancer have demonstrated a significant increase in hemoglobin concentration, water percentage, and tissue optical index, in responding patients as early as one week after chemotherapy treatment initiation [12]. The utility of these modalities in the clinic, however, is limited due to long wait times and the requirement of contrast agents in the case of MRI, poor resolution and limited penetration in the case of DOI, and health concerns over the use of radioactive material in the case of PET.

Ultrasound is commonly used in the clinic for screening, diagnosis, and image-guided procedures, due to its relatively low cost, short imaging time, high resolution, radiation-free nature, and intrinsic tumour contrast which does not require injection of any contrast agents. Brightness mode (B-mode) imaging, which provides grayscale intensity images generated by reflections from different tissue interfaces, is the standard mode of ultrasound imaging used by sonographers and radiologists. However, the frequency dependent information from tissue echo signals is lost during conversion of the raw ultrasound backscatter radiofrequency (RF) signal to B-mode images. Quantitative ultrasound tissue characterization encompasses a wide spectrum of signal analysis techniques applied to the RF ultrasound data (and sometimes applied to B-mode images) to extract parameters which can characterize various tissue abnormalities such as those of the prostate, lymph nodes, eye, as well as the myocardium [13]–[16].

Advantages of analyzing the RF data as opposed to the B-mode data include instrument-independent parameter estimations through normalization and correction for frequency-dependent effects such as attenuation. The most frequently used tissue characterization techniques in the frequency domain are linear regression spectral analysis and backscatter coefficient (BSC) estimation. According to the theoretical formulation of ultrasound scattering, the tissue power spectrum is affected by parameters such as size and number density of the constituent scatterers [17]. Thus, based on inherent differences in the microstructures of different tissues, parameters

obtained from the tissue power spectrum, including midband fit (MBF), spectral intercept (SI), and spectral slope (SS), have enabled the characterization of abnormalities of different tissues such as prostate, liver, eye, myocardium, and lymph nodes [14], [16], [18]–[20]. Additionally, BSC parameters including average scatterer diameter (ASD) and average acoustic concentration (AAC) have been used to characterize mouse models of breast cancer, characterize and monitor clinical breast cancer during treatment, and characterize malignant versus non-malignant lymph nodes [16], [21]–[24]. For convenience hereafter, the term QUS will refer to ultrasound tissue characterization techniques based on frequency-dependent backscatter analysis, including RF spectrum and BSC analyses.

In addition to characterizing tissue abnormalities, QUS techniques have been used to detect cell death. Using high-frequency ultrasound (20–25 MHz) imaging, previous *in vivo* studies have demonstrated that MBF and SS increase as a result of cell death induced by photodynamic therapy [25] and radiation therapy [26] of mouse xenograft tumours. Such increases in spectral characteristics were found to be associated histologically with morphological changes in the dying cell, including nuclear condensation and fragmentation. As well, parallel ultrasound observations were made at a clinically relevant ultrasound frequency range (4.5–9 MHz) when xenograft breast cancer tumours were treated with chemotherapy [27]. This finding suggested the potential for a new application of QUS: predicting tumour response to anticancer therapy using QUS techniques through surrogate measures of tumour cell death.

More recently, ultrasound imaging applications have been extended to include therapy response monitoring, particularly in breast cancer imaging. In a pilot study by Sadeghi-Naini *et al.* [28], quantitative ultrasound spectral parameters, including MBF, SS, and SI were extracted from RF ultrasound backscatter data obtained retrospectively from responding and nonresponding breast tumours. Using the combination of MBF and SI parameters, 100% sensitivity and 83% specificity to the detection of response of the tumours to chemotherapy was demonstrated.

### 1.3 Basic principles of ultrasonic scattering in biological tissues

There are three well-established scattering models: the Faran theory for solid spheres and cylinders [29], the fluid-filled sphere model [30], and the Gaussian model (eq. 22 in [31]). The Faran theory

is the most accurate model when the exact scatterer geometry is known, and thus commonly used for characterizing tissue-mimicking ultrasound phantoms which contain glass beads [32]. This theory gives the closed form solution of the scattered pressure by a solid sphere (or cylinder) when irradiated by an incident plane wave. The caveat of Faran's theory is the analytical complexity. Because of this, analytically simpler models have been developed by assuming weak scattering (ignoring multiple scattering) and ignoring shear wave propagation. These models are called form factor models. A form factor is a measure of frequency-dependent scattering based on the shape, size and mechanical properties of the constituent scatterers. Particularly, the Gaussian form factor (FF), expressed by equation 0, has been used frequently to model scattering by soft tissues [14–16] as it represents a distribution of gradually changing acoustic impedance between the scatterer and the background material. The fluid-filled sphere form factor (equation 1.2) represents scattering from a fluid-filled scatterer in a fluid-like medium. The models are expressed as follows [31]:

$$F_{Gauss}(2k) = e^{-0.827k^2a^2} \quad 1.1.$$

$$F_{FFS}(2k) = \left[ \frac{J_1(2ka)}{\frac{2}{3}ka} \right]^2 \quad 1.2.$$

In the above formulas,  $J_1$  is the spherical Bessel function of the first kind and first order,  $k = \frac{2\pi f}{c}$  is the wavenumber,  $c$  is sound speed,  $f$  is frequency, and  $a$  is scatterer radius. The parameter usually measured for estimating scatterer properties is the BSC. The BSC is a frequency-dependent function that represents the backscattered power per unit solid angle normalized to incident intensity [33]. Result validations often involve comparison of the measured BSC to a theoretical model, which incorporates the form factor (FF). A BSC can be related to a form factor,  $F(k, a)$ , by the following relation [34],

$$\sigma_b(k) = \frac{\bar{n}}{9} k^4 a^6 \gamma^2 F(k, a) \quad 1.3.$$

where  $\bar{n}\gamma^2$  is the average acoustic concentration, AAC,  $k = \frac{2\pi f}{c}$  is the wave number,  $a$  is the scatterer radius, and  $\gamma^2$  is the mean square deviation between the impedance of the scatterers and the surrounding medium. In this equation, impedance is the product of density ( $\rho$ ) and speed ( $c$ ).

## 1.4 Ultrasound radiofrequency spectrum

As previously mentioned, analysis of the frequency content of the backscattered tissue signal permits characterization of the tissue in terms of its microstructure. By modeling the tissue echo power spectrum (ultrasound radiofrequency spectrum) as a linear approximation of the Fourier transform of the acoustic impedance autocorrelation, Lizzi *et al.* demonstrated that SS is related to the scatterer size and SI and MBF can be related to the scatterer concentration [17]. These parameters are estimated from a linear regression analysis of the tissue power spectrum within the usable bandwidth (usually corresponding to  $-6$  dB range). An ultrasound RF image region of interest (ROI) usually consists of smaller blocks (windows) in which the power spectra are calculated. Figure 1-1 presents a schematic plot of the normalized power spectrum in an RF window, corresponding linear regression line, and a graphical description of the spectral parameters. The amplitude line spectrum,  $A_l(f, z_l)$ , of a gated RF line segment,  $z_l$ , can be calculated using the reference phantom technique [35], as shown in equation 1.4. In this equation,  $A_s(f, z_l)$  is the fast Fourier transform (FFT) of an RF line segment of the sample after gating with a Hanning window, and  $A_r(f, z_l)$  is the FFT of the gated RF signal from a calibration reference. The log power spectrum,  $S(f)$ , can then be computed by averaging the squared magnitudes of the amplitude line spectra laterally across the window, compensating for sample and reference attenuation, and taking the log of the result, as presented in equation 1.5 [35]. The attenuation coefficients of the sample and reference are  $\alpha_s$  and  $\alpha_r$ , respectively;  $R$  is the range (transducer to proximal edge of window); and  $\Delta z$  is the window length (axial).

$$A_l(f, z_l) = \frac{A_s(f, z_l)}{A_r(f, z_l)} \quad 1.4.$$

$$S(f) = \log_{10} \frac{1}{N} \sum_{l=1}^N |A_l(f, z_l)|^2 e^{-4(\alpha_s - \alpha_r)(R + \frac{\Delta z}{2})} \quad 1.5.$$

While  $A_r(f, z_l)$  can refer to the spectrum of a planar reflector or a phantom, in this thesis, a phantom is used as the reference for RF spectral analysis in order to facilitate depth-dependent corrections.

A line of best fit, using least squares, can be found for the normalized power spectrum within the -6 dB frequency bandwidth as per Lizzi's method [17],

$$S(f) = SSf + SI \quad 1.6.$$

$$MBF = S(f_c) \quad 1.7.$$

where  $SS$  and  $SI$  are the slope and extrapolated 0-MHz intercept of the line of best fit, and  $MBF$  is the solution of the line-approximated power spectrum at the center of the frequency bandwidth (i.e., 6.75 MHz in the example plot). The bandwidth was determined from the power spectrum of a reference phantom.

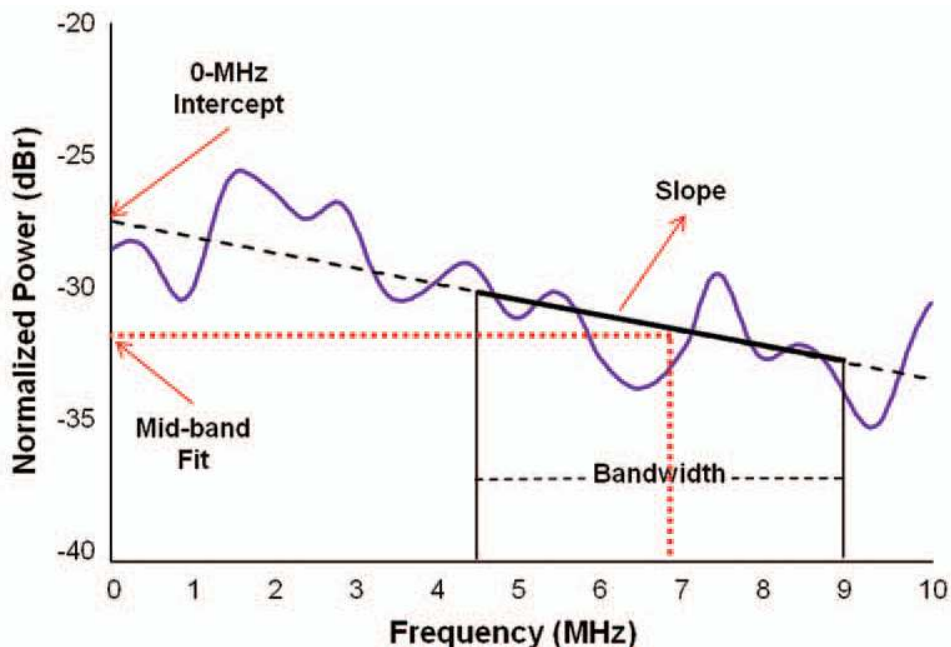


**Figure 1-1.** A schematic plot of the normalized power spectrum with linear regression applied to the –6dB transducer bandwidth (4.5 – 9 MHz). dBr is defined as decibels relative to reference. Adapted from [36].

## 1.5 Scatterer spacing estimation using spectral autocorrelation

Scatterer spacing, also known as spacing among scatterers (SAS), is defined as the distance between regularly spaced or periodic scatterers in a medium. It is computed from the autocorrelation of the power spectrum estimated by the autoregressive (AR) model. This method has been demonstrated to detect distance between periodic scatterers in tissue microstructures having lower orders of regularity [37], such as those of the liver, for characterization of liver diseases [38]–[40]. The AR model predicts the output of a stationary stochastic process as a linear combination of previous samples of its output, and is defined as [41],

$$\hat{e}_s[t] = \sum_{k=1}^p a_k \hat{e}_s[t - k] + w[t], \quad 1.8.$$

where  $a_k, k = 1, \dots, p$  are the AR coefficients,  $w[t]$  is a white noise input sequence, and  $p$  is the order of the AR model. The power spectrum,  $|X(f)|^2$ , can be obtained by Fourier transforming both sides of equation 1.8 to yield [42],

$$|X(f)|^2 = \frac{\delta^2}{|1 + \sum_{k=1}^p a_k e^{-j2\pi f k}|^2}, \quad 1.9.$$

where  $\delta$  is the standard deviation of the white noise. As demonstrated in equation 1.10, the normalized power spectrum,  $S(f)$ , can be obtained in a manner similar to that shown in the previous section, except that the numerator was an AR-estimated power spectrum ( $|X(f)|^2$ ) and the denominator was echo data from a polished Plexiglas surface,  $e_r(t_n)$ . The subscript “n” represents discrete depth intervals  $n = 1, 2, \dots, 6 \text{ cm}$ . Also  $e_r(t_n)$  was independent of lateral location,  $x_i$ , as the power spectra of the reflector echoes were averaged across the RF lines over the image width to obtain a smooth mean power spectrum. This was done to obtain a good signal-to-noise ratio and to average out any microscopic variances in the planar reflector's surface.

$$S(f, x_i) = \frac{\sum_{i=N}^M |X(f, x_i)|^2}{\sum_{i=0}^L |FFT(e_r(t_n))|^2}, n = 1, 2, \dots, 6 \text{ cm}. \quad 1.10.$$

Finally, the autocorrelation of the normalized AR power spectrum,  $R_{ff}(\Delta f)$ , was computed using equation 1.11,

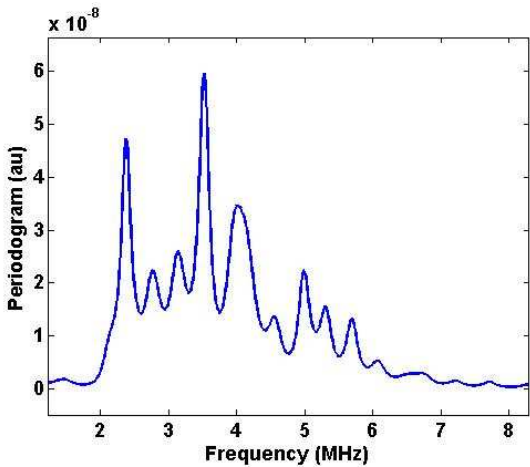
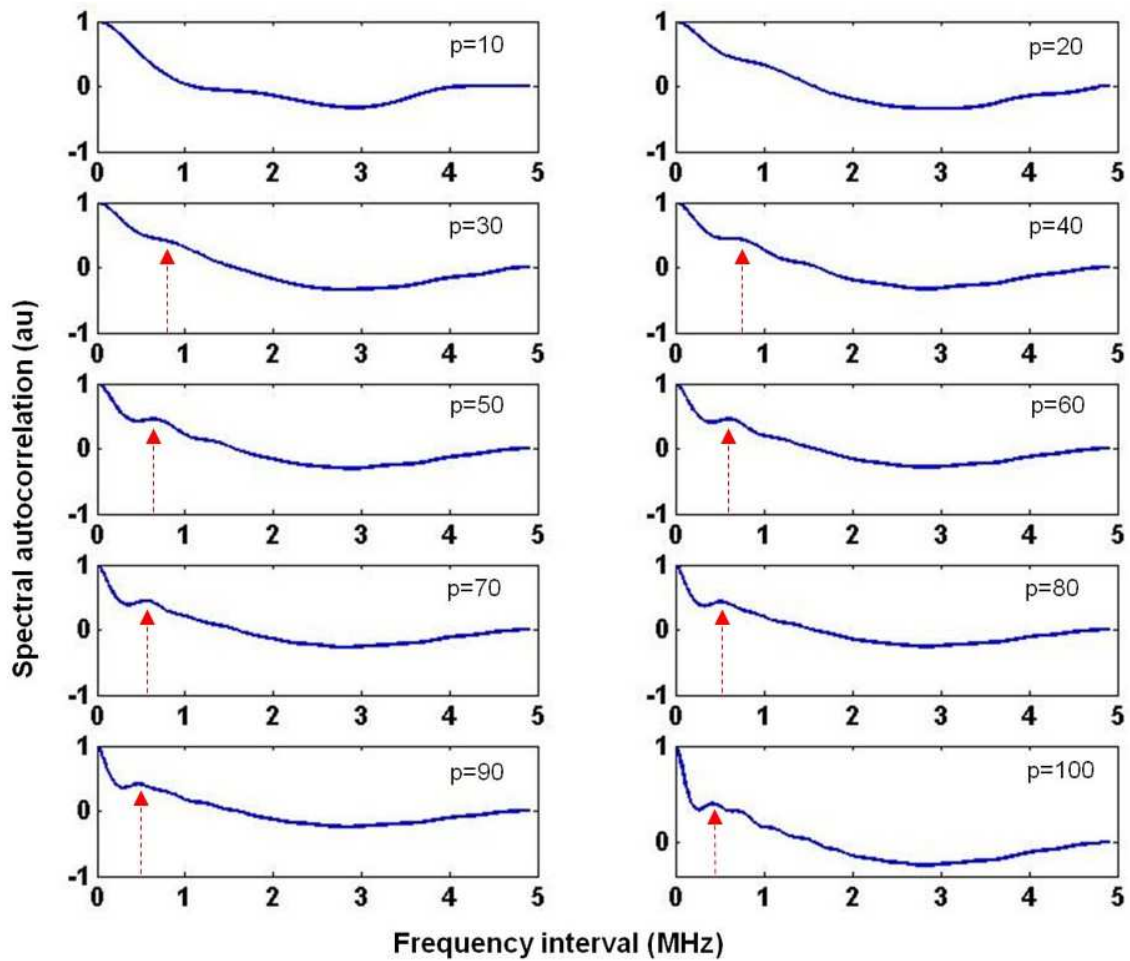
$$R_{ff}(\Delta f) = \sum_{\Delta f=1}^N S(f)S(f - \Delta f), \quad 1.11.$$

which is termed the spectral autocorrelation (SAC). The SAS corresponds to the frequency lag,  $\Delta f_p$ , at which the first peak in the SAC occurs,

$$SAS = \frac{c}{2\Delta f_p}, \quad 1.12.$$

where  $c$  is the mean speed of sound in the tissue of interest. For normal tissue ROIs, which encompassed mainly glandular tissue, a speed of sound of 1455 m/s is assumed while for tumour ROIs, a speed of sound of 1540 m/s is assumed. These values are consistent with tomography measurements of the speed of sound in the breast [43].

Figure 1-2A presents an example AR-estimated power spectrum from a human breast tumour ROI, and Figure 1-2B presents the corresponding SAC plots computed using different model order ( $p$ ) values, varying from  $p = 10$  to 100. The arrows indicate the location of the first peak, from which SAS is computed. It can be observed that at lower  $p$  values, the SAC peaks are difficult or impossible to discern due to the low power spectrum resolution. As  $p$  increases, and therefore the number of AR coefficients increases, the peak becomes more discernable. However, if  $p$  becomes too large, i.e. 100 or larger, multiple peaks start to appear, resulting in false peak detection. In this thesis,  $p = 50$  was found to be the optimal balance between power spectrum resolution and false peak detection and was selected for all SAC and SAS computations in the breast tissue.

**A****B**

**Figure 1-2.** (A) Typical power spectrum estimated using the AR model from a human breast tumour. (B) Corresponding spectral autocorrelation functions for different AR model order ( $p = 10-100$ ). At lower orders ( $p < 50$ ), no peaks can be detected. At  $p = 100$ , false peaks appear.

## 1.6 The backscatter coefficient and estimation of its parameters

Scatterer property estimation (i.e., scatterer size and acoustic concentration) in tissue characterization involves finding an optimal match between a theoretical model and the experimentally derived values of the BSC curve by varying the parameters of the model. The theoretical formulation was already defined in equation 1.3. Next the BSC must be determined experimentally ( $\hat{\sigma}_b$ ) from the obtained RF data.  $\hat{\sigma}_b$  can be computed from the normalized power spectrum at the focus,  $S_F(f)$ , after applying a scaling factor consisting of transducer aperture area ( $A_0$ ) and target distance ( $R^2$ ), as presented in equation 1.13 [34]. Note that  $S_F(f)$  is the planar reflector normalized power spectrum obtained by placing the transducer's focus in the centre of the sample. Whereas the aperture area of a single-element focused transducer can be simply calculated as  $\pi r^2$  ( $r$  = radius of the aperture), an array transducer has a synthetic aperture which requires knowledge of the range-dependent aperture opening function to compute its area. This function defines the number of receive elements as a function of depth (axial distance from the transducer surface). With this knowledge, one can obtain the aperture area at focal depth. This method of BSC estimation requires prior repeated measurements of planar reflector echo at all depths for which the sample windows are located. Alternatively, a reference phantom can be used to estimate the BSC of a sample given the known BSC of the phantom,  $\sigma_{br}(f)$ , and the phantom-normalized power spectrum,  $S(f)$ , using equation 1.14 [35].

$$\sigma_{br}(f) = \frac{1.45R^2}{A_0} S_F(f), \quad 1.13.$$

$$\hat{\sigma}_b(f) = S(f)\sigma_{br}(f)e^{4(\alpha_s - \alpha_r)(R + \frac{\Delta z}{2})} \quad 1.14.$$

Once the  $\hat{\sigma}_b(f)$  corresponding to an ROI in the sample has been obtained, the ASD from the ROI can be estimated by minimization of the average standard deviation (MASD) between the estimated and theoretical BSCs as follows (ref [31], equation 43):

$$MASD = \min \left( \frac{1}{m} \sum_{i=1}^m X_i - \bar{X} \right) \quad 1.15.$$

$$X_i = \log\left(\frac{\widehat{\sigma}_b(f_i)}{\sigma_b(a, f_i)}\right) \quad 1.16.$$

$$\bar{X} = \frac{1}{N} \sum_{i=1}^N X_i \quad 1.17.$$

where  $f_i, i = 1, \dots, m$  is the frequency vector for which FFT data have been computed within the -6 dB system bandwidth. Finally, ASD is derived as the average scatterer diameter ( $2a$ ) of the theoretical BSC,  $\sigma_b(a, f_i)$ , corresponding to the MASD. Once the ASD has been obtained by model fitting, one can estimate the AAC ( $\bar{n}\gamma^2$ ) by substituting  $\hat{\sigma}_b$  for  $\sigma_b$  in equation 1.3 and solving for  $\bar{n}\gamma^2$ . In order to validate the estimation of ASD using this fitting algorithm, I applied this algorithm on an ultrasound phantom consisting of glass microspheres embedded in agar gel. The glass microspheres served as the scatterers with a known size distribution. I used Faran's theory of sound scattering from solid spheres [29] to predict the scattering from the phantom and performed fitting between this function and the measured BSC (obtained using our linear array transducer) to estimate the ASD. Details of the methods and results are provided in the Appendix under "Transducer characterization and validation of scatterer size and attenuation estimation". Details about Faran's theory can be found in the Appendix under "Analytical solution for scattering from solid spheres".

## 1.7 Frequency-dependent acoustic attenuation

The power spectrum and BSC measurements are affected by the inherent frequency-dependent attenuation of intervening tissues, and, if not corrected, will yield inaccurate estimates of scattering properties. Frequency-dependent attenuation has been shown to be a useful parameter in characterizing tissues, especially tumours and normal tissues of the breast [44]. Additionally, a previous clinical study found large variations in the attenuation coefficient values among breast tumours ( $1.16 \pm 0.8$ dB/cm/MHz) [22]. Attenuation loss from homogeneous samples can be estimated by an insertion-loss method [44]. Figure 1-3 illustrates the insertion-loss technique. In this method, an ultrasonic pulse is transmitted from the transducer toward a planar reflector which is coupled with degassed water. The power spectrum of the transmitted pulse,  $S_X(f)$ , is computed from the RF echo of the reflector. Then, the attenuating sample is placed between the transducer and the reflector to evaluate the change in the reflected power spectrum ( $S_Y(f)$ ) as a result of

adding the sample. The attenuation coefficient ( $\alpha$ ) is found from the log difference of attenuated ( $A_y(f)$ ) and un-attenuated ( $A_x(f)$ ) amplitude spectra, written as [45],

$$\alpha(f) = \alpha_r(f) + \frac{20}{2d} \log \left( \frac{A_x(f)}{A_y(f)} \right) \quad 1.18.$$

where  $\alpha_r$  is the attenuation function of the reference medium (typically PBS or degassed water)  $d$  is the thickness of the attenuating sample in the longitudinal sound propagation direction, and the factor of 2 accounts for the round trip of the ultrasound wave. For breast tissues, the power law relationships lie in the range of  $n = 0.8$  to  $1.9$  [44]. Whereas for a homogeneous sample the attenuation coefficient holds throughout the sample, equation 1.18 does not apply to the local attenuation coefficient of a heterogeneous sample. A more rigorous method is required to estimate the local attenuation coefficients in a homogeneous region of a heterogeneous sample. To achieve this, Labyed *et al.* developed the reference phantom algorithm, a method of estimating the local attenuation coefficient of a locally homogeneous region in an ultrasound image by estimating the rate of change in the spectral magnitude with depth and frequency relative to a reference medium with a known attenuation coefficient [46]. I validated this method of attenuation coefficient estimation using a reference phantom. Details of the validation work is provided in the Appendix under “Transducer characterization and validation of scatterer size and attenuation estimation.”

Once the attenuation for the sample of interest has been found, the power spectra calculations can be corrected for attenuation by multiplying by the term [47],

$$A(f) = e^{4\alpha f^n d} \quad 1.19.$$

where  $n$  is the exponent of the frequency power law, varying depending on the tissue. The correction term must be used for every attenuating layer the ultrasound passes through, including water (although the attenuation of water is negligible at low frequencies).

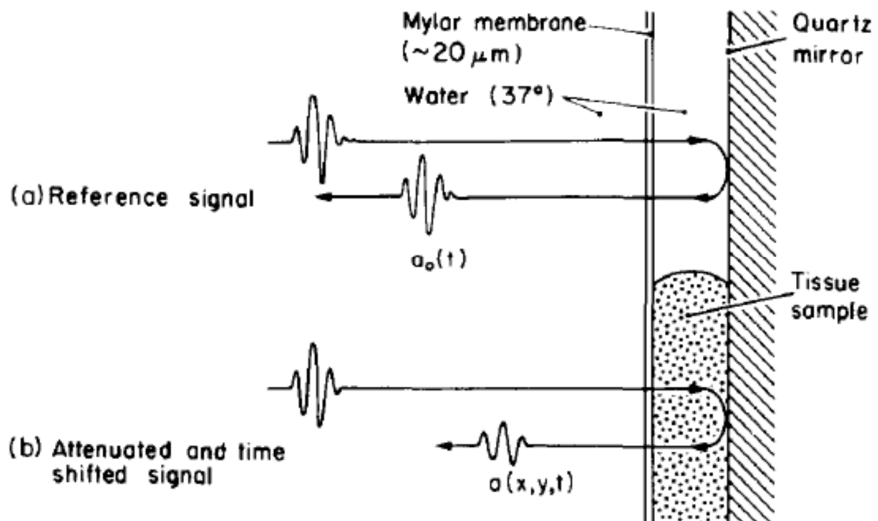


**Figure 1-3.** Signals used in the measurement of frequency dependent attenuation. The sample is sandwiched between a thin mylar membrane and a quartz optical flat. By measuring the RF signal, both with (b) and without (a) the sample present, it is possible to compute the frequency dependent attenuation coefficient which is based on the ratio of the magnitude spectra of these two signals. Adapted from [44].

## 1.8 Statistical texture analysis

The concept of texture analysis on digital images dates back to 1973, when Haralick *et al.* formulated the gray-level co-occurrence matrix (GLCM) and used it to identify different types of landscapes in aerial photographs [48]. The GLCM describes the angular relationship between neighbouring pixels as well as the distance between them. An example of the construction of a GLCM is presented in Figure 1-4. In this example, the source image is a 3-bit (8-levels) grayscale image. Therefore, the GLCM must be 8-by-8 pixels. Each element in the GLCM represents the number of occurrences of a certain spatial pixel combination in the source image. In this example, the combination of 1, 1 occurs once. Therefore, a 1 will be placed in row 1, column 1, of the GLCM. Looking further, the combination of 1, 2 occurs twice in the image. Therefore, a value of 2 will be placed in row 1, column 2 of the GLCM, and so on.

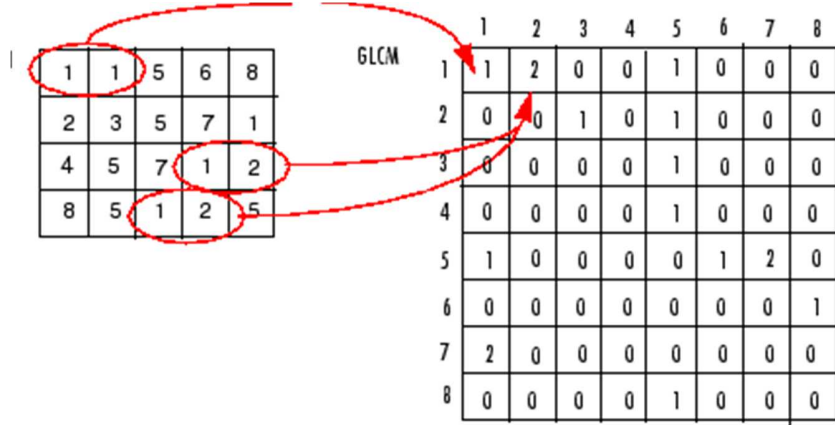


**Figure 1-4.** Process of GLCM computation. The left matrix is an 3-bit grayscale image and the right matrix is the corresponding GLCM constructed using a distance of one pixel and an angle of  $0^0$ . Adapted from [49].

Based on the statistical information provided by a GLCM, 14 textural features can be obtained. For this thesis, four of these features were used, those most relevant to tissue characterization: contrast, correlation, homogeneity, and energy. These are defined below.

$$CON = \sum_{i=j=0}^{N_g-1} (i-j)^2 \sum_{i=1}^{N_g} \sum_{j=1}^{N_g} p(i,j) \quad 1.20.$$

$$ENE = \sum_{i=1}^{N_g} \sum_{j=1}^{N_g} p(i,j)^2 \quad 1.21.$$

$$HOM = \sum_{i=1}^{N_g} \sum_{j=1}^{N_g} \frac{p(i,j)}{1 + |i - j|} \quad 1.22.$$

$$COR = \frac{\sum_{i=1}^{N_g} \sum_{j=1}^{N_g} (i - \mu_i)(j - \mu_j)p(i,j)}{\sigma_i \sigma_j} \quad 1.23.$$

where  $p(i,j)$  is an element in a  $N_g \times N_g$  GLCM, where  $N_g$  is the number of gray levels,  $\mu_i, \sigma_i$  are the mean and standard deviation of the  $i$ 'th row of the GLCM, and  $\mu_j, \sigma_j$  are the mean and standard

deviation of the j'th column of the GLCM. The contrast parameter represents a measure of difference between the lowest and highest intensities in a set of pixels. The energy parameter measures the frequency of occurrence of pixel pairs and quantifies its power (square of the frequency of gray-level transitions). The homogeneity parameter measures the incidence of pixel pairs of different intensities. As the frequency of pixel pairs with close intensities increases, homogeneity increases. The correlation parameter measures the intensity correlation between pixel pairs.

## 1.9 Ultrasound detection of cell death

In addition to characterizing tissue abnormalities, QUS techniques have been used to detect cell death. In an initial study using high frequency (40 MHz) ultrasound, where acute myeloid leukemia cells were treated with cisplatin (a chemotherapeutic agent), a 25-to-50 fold increase in the US backscatter intensity was observed in apoptotic cells compared to viable cells. This observation led to the hypothesis that the cell nucleus is the source of ultrasound scattering, and that it is the morphological changes occurring in the nucleus during apoptosis that causes such ultrasound backscatter changes. This hypothesis was investigated by Taggart *et al.* [45], where they demonstrated experimentally that cells with larger nuclear diameters express higher integrated backscatter coefficients (Figure 1-5). Recalling that SS is theoretically related to scatterer size and MBF can be related to scatterer concentration, these parameters have been proven to be sensitive to morphological changes that occur in cells during cell death due to nuclear changes. Particularly, *in-vivo* studies demonstrated, using high-frequency ultrasound (20-25 MHz) imaging, that MBF and SS increase as a result of cell death induced by photodynamic therapy [25] and radiation therapy [26] of mouse xenograft tumours. Such increases in spectral characteristics were found to be associated histologically with morphological changes in the dying cell, including nuclear condensation and fragmentation. However, SS changes are dependent on the mode of cell death. Whereas SS has been found generally to increase predominantly in tumours that undergo apoptosis, it has remained relatively constant in tumours where there is a mixture of cell death modes and decreased when there is mitotic arrest due to an increase in cell size [50]. Figure 1-6 illustrates changes in B-mode images (A) caused by photodynamic therapy at different times (1, 3, 6, 12, 24, and 48 hours), the resulting MBF and SS changes (B and C respectively), and

corresponding magnified TUNEL sections (D). The B-mode images demonstrate a gradual increase in the backscatter intensity in the tumour, peaking at 24 hours, and dropping slightly at 48 hours. Similarly, the SS monotonically increased until 24 hours, leveling off at 48 hours. The MBF increased monotonically until 12 hours, after which it decreased steadily until 48 hours. In terms of histology, the TUNEL sections demonstrate increasing areas of fragmented nuclei filling the extracellular space (brown stains) and loss of nuclei (blue stains) as time passes, indicating an increase in cell death. However, those studies were performed using high frequency (20 MHz and above) ultrasound imaging, which is limited by penetration depth ( $\sim$ 2 cm). Deep-lying breast tumours will not be visible in ultrasound images produced at such frequencies. A more recent study used low frequency (7 MHz) ultrasound imaging to examine the effects of cell death *in vivo* [27]. The study demonstrated that when a mouse bearing a human breast tumour (MDA-MB231) is treated with chemotherapy, the tumour-associated MBF and SI levels increase fairly proportionally with cell death ( $R^2 = 0.67$  and 0.61, respectively). An explanation for changes in ultrasound backscatter properties resulting from cell death have been proposed by Hunt *et al.*, via an ultrasound scattering simulation study with pseudo-regular spacing of cells [51]. Hunt *et al.* theorized that the spatial organization of cells in a biological tissue is similar to the spatial organization of the atoms/molecules in an imperfect crystal, and thus the backscattered signal from such tissue is formed from constructive and destructive interference of the scattering from the cells, due to the pseudo-regular spacing of cells. Figure 1-7B demonstrates that as more nuclei are randomly lost (i.e., through nuclear fragmentation and nuclear degradation stages of cell death), the backscatter signal amplitude increases to a certain point (40% nuclei loss), after which the amplitude drops. The aforementioned theory and simulation can explain the trend seen in the MBF versus time curve (Figure 1-6B)—time-dependent changes in the MBF result from changes in the spatial organization of the nuclei due to nuclear condensation, fragmentation, and degradation (degradation causes the drop). As SS has been shown to be inversely related to scatterer size [52], the increase in SS (Figure 1-6C) can be explained by the decrease in the size of the scatterers due to nuclear fragmentation.

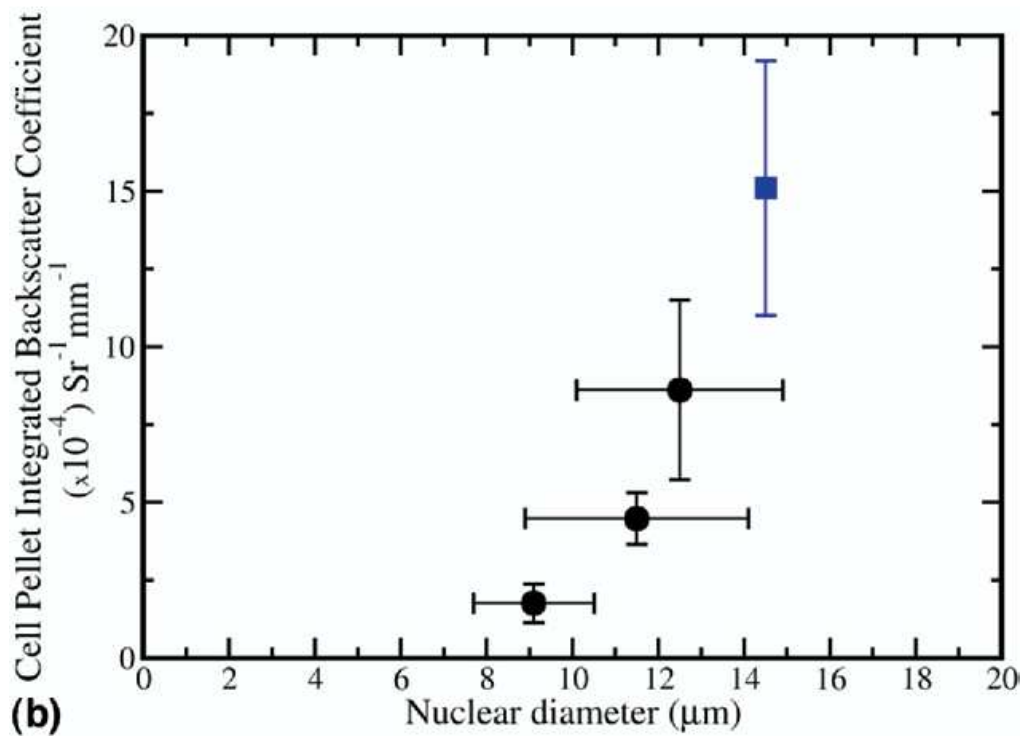


**Figure 1-5.** Integrated backscatter coefficient versus nuclear diameter of a cell. The data were acquired from whole cells, with the diameter of the cell nucleus plotted along the x-axis. The square denotes the MT-1 cell line for which the nuclear diameter was measured by visual inspection of the microscopy images of whole cells. Adapted from [45].

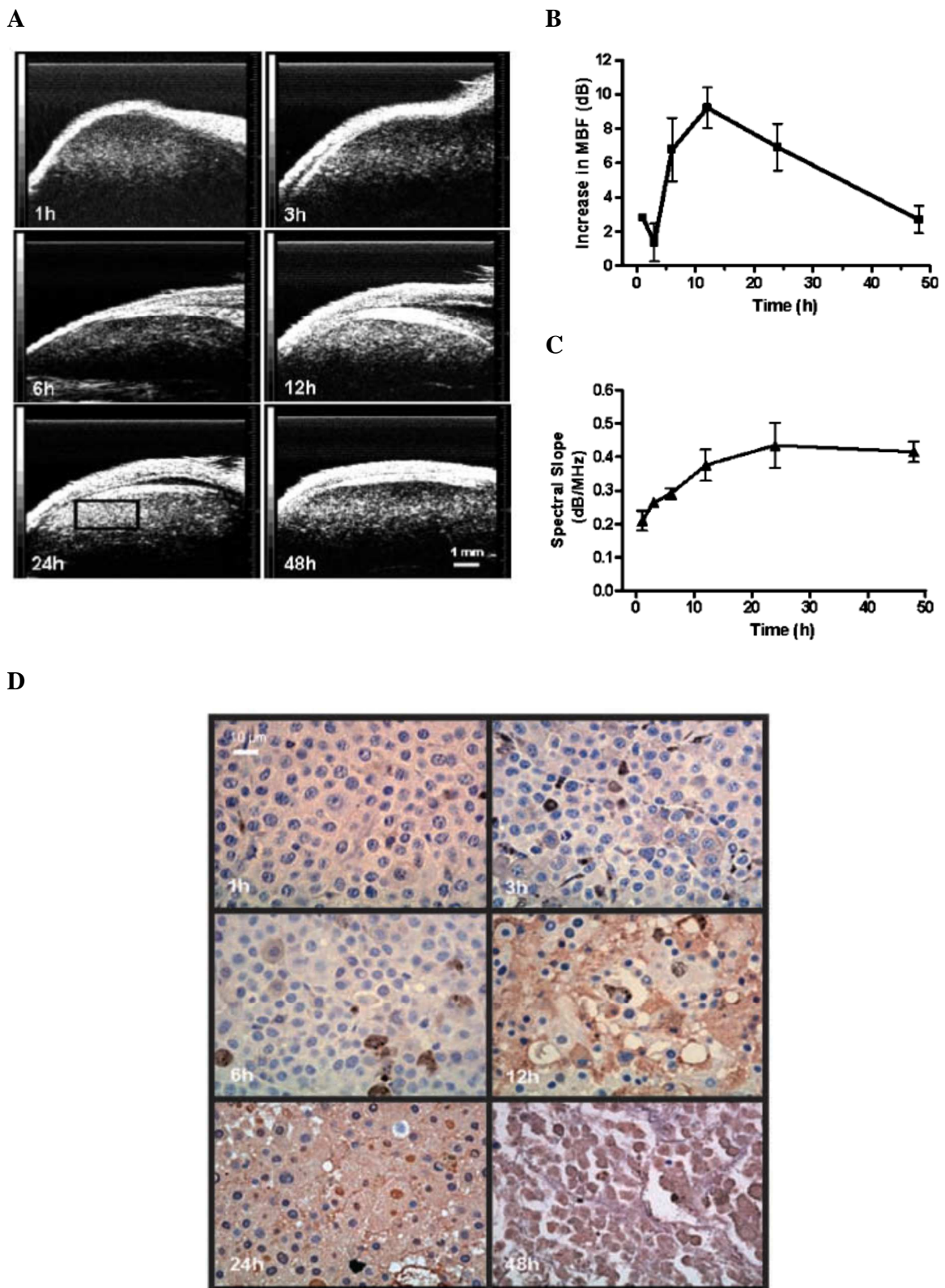


**Figure 1-6.** Results of photodynamic therapy on *in vivo* xenograft tumours. Tumours were examined using 26-MHz ultrasound before treatment and at different times after administration of PDT ( $n = 3$  animals per time). Ultrasound data collection consisted of acquiring B-scan images (A) in addition to spectroscopic data for quantitative analyses of backscattered ultrasound (B,C). At 24 h, there was an increase in backscatter that was detected in ultrasound images, as well as in spectroscopic data. (D) TUNEL sections at  $40\times$  magnification. Typical changes of apoptosis were observed, including nuclear coalescence and fragmentation, as the function of time. At 48 h, nearly half of the cells in the treated area had lost their nuclei as in a final stage of apoptotic cell death. These changes explain the detected changes in variables related to the size of scatterers in the tissue by ultrasound. Adapted from [25].

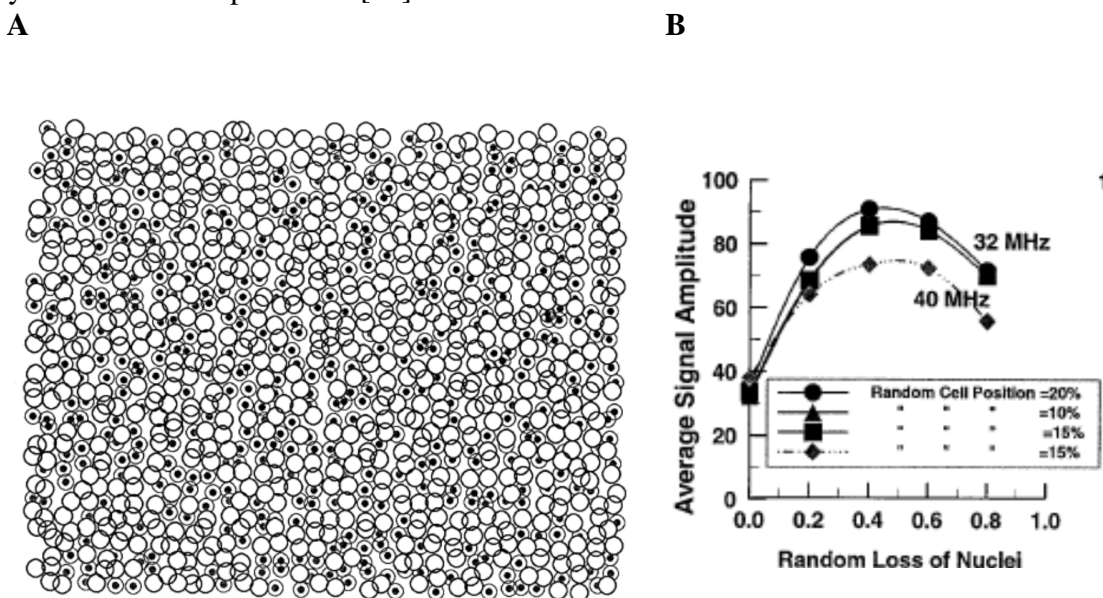


**Figure 1-7.** Scattering simulation with pseudo-regular spacing of cells. Left: a typical pseudo-regular cell array with random loss of nuclei. This array was used as input data for the simulation. Predictions of the average signal amplitude if, in a random way throughout the cell, a fraction of the nuclei, or its fragments, have disappeared during apoptosis. Adapted from [51].

## 1.10 Quantitative ultrasound parameters investigated

In this thesis, I examined QUS parameters related to breast tissue microstructural and macrostructural properties in order to noninvasively characterize breast tumours and their response to therapy. A summarized list of all investigated QUS parameters and their relation to tissue properties is provided in Table 1-1.

**Table 1-1.** Investigated QUS parameters, their definition, and their link to biology.

Parameter	Abbreviation	Definition and link to biology
Attenuation Coefficient Estimate	ACE	<ul style="list-style-type: none"> <li>• Depth and frequency dependent rate of decrease in acoustic energy</li> <li>• Related to tissue composition and density.</li> </ul>
Average Acoustic Concentration	AAC	<ul style="list-style-type: none"> <li>• Product of scatterer number density and mean squared variation in acoustic impedance between scatterer and background</li> <li>• Changes in organization of diffuse tissue microstructures can lead to changes in this parameter</li> </ul>
Average Scatterer Diameter	ASD	<ul style="list-style-type: none"> <li>• Average diameter of a spherical scatterer or effective diameter of a scatterer with an acoustic impedance distribution that follows a Gaussian function.</li> <li>• Can be related to the size/shape of a cell or cell cluster when the size is comparable to the wavelength of the transmitted acoustic wave</li> </ul>
Midband Fit	MBF	<ul style="list-style-type: none"> <li>• Value of the power spectrum regression line at the center of the frequency bandwidth</li> <li>• Related to acoustic concentration, scatterer size, and attenuation, and thus affected by size, composition, and distribution of tissue microstructure</li> </ul>
Spacing Among Scatterers	SAS	<ul style="list-style-type: none"> <li>• A feature of the periodicity of the power spectrum that gives the mean distance between regularly spaced scatterers</li> <li>• Can be related to distance between lobuli glandula mammaria of the breast [42]</li> </ul>
Spectral Intercept (Zero-MHz Intercept)	SI	<ul style="list-style-type: none"> <li>• Zero-MHz intercept of the power spectrum regression line</li> <li>• Similar to MBF but independent of attenuation</li> </ul>
Spectral Slope	SS	<ul style="list-style-type: none"> <li>• Slope of the power spectrum regression line</li> <li>• Related to the scatterer size</li> </ul>

## 1.11 Thesis overview and hypothesis

This thesis investigates the potential of quantitative ultrasound parameters extracted from conventional-frequency (6 MHz) ultrasound data in making early prediction of breast tumour response to chemotherapy treatment lasting seven months. Towards this end, three objectives were explored.

**Objective 1 (Chapter 2): A study of the correlation between high- and low-frequency ultrasound parameter changes and extent of cell death *in vivo* using human breast tumours grown in severe combined immunodeficient (SCID) mice.** This study was performed using two ultrasound imaging systems: a high-frequency (25 MHz) and a low frequency (7 MHz) system. The study began by implementing two existing scattering models—the spherical Gaussian and fluid-filled sphere models—that may potentially be used to estimate ASD from tumours *in vivo*. At each frequency, the models were compared against each other in terms of goodness of fit to the measured BSC, the proximity of estimated ASDs to tumour cell size, and the strength of the correlation between the extracted parameters and the extent of cell death determined histologically.

The work presented in Chapter 2 was based on the following manuscript:

H. Tadayyon, L. Sannachi, A. Sadeghi-Naini, A. Al-Mahrouki, W. Tran, M.C. Kolios, and G.J. Czarnota, "Quantification of ultrasonic scattering properties of *in vivo* breast cancer cell death induced by chemotherapy treatment" *Physics in Medicine and Biology*, under revision as of July 2015.

**Objective 2 (Chapter 3): Characterization of LABC tumours in terms of their ASD and AAC, determined using the method developed in Chapter 3 and using the optimal scattering model found in Chapter 2.** The characterization study used clinical ultrasound (6 MHz) to examine normal breast tissue and different grades of LABC breast tumours. In addition to classical QUS parameters MBF, SS, and SI, this study examined the periodicity feature (SAS) of LABC tumours via spectral autocorrelation analysis. For characterization of tumour grades, the attenuation coefficient estimate (ACE) of the tumours was also determined as an additional characterization parameter. Characterization results were evaluated using the linear and quadratic discriminant classifiers.

- a. First I examined the mean values of the QUS parametric maps (of ASD, AAC, ACE, SAS, MBF, SS, and SI) for characterization of normal breast tissues and different grades of tumours.
- b. Second, I examined the textural features of QUS maps (contrast, correlation, energy, homogeneity) as alternative characterization parameters.
- c. Third, I examined the combination of mean and texture features of QUS maps for characterization, and compared its classification performance to means and textures alone (cases a and b).

The work presented in Chapter 3 was based on the following manuscripts:

H. Tadayyon, A. Sadeghi-Naini, L. Wirtzfeld, F. C. Wright, and G. Czarnota, “Quantitative ultrasound characterization of locally advanced breast cancer by estimation of its scatterer properties.,” *Med. Phys.*, vol. 41, no. 1, p. 012903, Jan. 2014 (published).

H. Tadayyon, A. Sadeghi-Naini, and G.J. Czarnota, “Non-Invasive Characterization of Locally Advanced Breast Cancer using Textural Analysis of Ultrasound Spectral Parametric Images”, *Translational Oncology*, vol. 7, no. 6, Dec. 2014 (published).

**Objective 3 (Chapter 4): To determine the optimal set of quantitative ultrasound parameters in making early prediction of breast tumour response to chemotherapy treatment lasting several months.** This was achieved by extracting ASD and AAC parameters from the optimal scattering model developed in Chapter 2, obtained from the tumour ROI, and tracking them over treatment time. In addition, classical (MBF, SS, SI), spectral autocorrelation (SAS), and ACE parameters were examined. For classification, the data (ultrasound and histopathology) were divided into two groups—treatment responders and nonresponders. The K-nearest-neighbour classifier was used to discriminate between responding tumours and nonresponding tumours. The performance of the classifier was measured using cross-validation and sensitivity, specificity, and accuracy.

This work presented in Chapter 4 was based on the following manuscript (in preparation): H. Tadayyon, L. Sannachi, M. Gangeh, A. Sadeghi-Naini, M. Trudeau, and G.J. Czarnota, "Quantitative Ultrasound Assessment of Breast Tumour Response to Chemotherapy Using a Multi-Parameter Approach", To be submitted to Onco Target August 2015.

## **2 Correlation between QUS and cell death *in vivo* at the clinically relevant frequency range**

## 2.1 Overview

*Introduction:* QUS parameters based on form factor models were investigated as potential biomarkers of cell death in breast tumour (MDA-231) xenografts treated with chemotherapy.

*Methods:* RF data were acquired from xenografted MDA-231 breast cancer tumours (n=20) before and after injection of chemotherapy drugs, at two ultrasound frequencies - 7 MHz and 20 MHz. Four different treatment times were investigated – 4, 12, 24, and 48 hours after injection. Untreated control group mice were imaged at 0 hours and 24 hours. RF Spectral analysis involved estimating the BSC from regions of interest in the center of the tumour, to which form factor models were fitted, resulting in estimates of ASD and AAC. Changes in QUS parameters, including  $\Delta$ ASD,  $\Delta$ AAC, and changes in heterogeneity indices (HI) of ASD and AAC were compared with the extent of cell death obtained from tumour histopathology. Two form factor models - the spherical Gaussian model (SGM) and the fluid-filled sphere model (FFSM) - were compared in terms of correlation of extracted parameters to the extent of cell death.

*Results:* The  $\Delta$ AAC parameter extracted from the SGM was found to be the most effective cell death biomarker (at the lower frequency range, for  $\Delta$ AAC,  $r^2_{SGM}=0.40$ ,  $r^2_{FFSM}=0.10$ ). At both frequencies, AAC in the treated tumours increased statistically significantly ( $p <0.05$ ) 24 hours after injection, compared to control tumours. Furthermore, stepwise multiple linear regression analysis of the low-frequency data revealed that the linear combination of  $\Delta$ AAC,  $\Delta$ HI<sub>ASD</sub>, and initial tumour volume provided the strongest correlation to cell death ( $r^2 = 0.74$ ).

*Conclusion:* The Gaussian form factor model based estimates of  $\Delta$ AAC and  $\Delta$ HI<sub>ASD</sub> combined with initial tumour volume can potentially be used to track the extent of cell death at clinically relevant frequencies (7 MHz). The 20 MHz results agreed with previous findings in which parameters related to the backscatter intensity (i.e. AAC) increased with cell death. The findings suggested that, in addition to the BSC parameter  $\Delta$ AAC, tumour heterogeneity and initial tumour volume are important factors in the prediction of cell death response.

## 2.2 Introduction

Locally advanced breast cancer is characterized as a 5 cm or larger tumour often with involvement of the axillary lymph nodes, skin, and/or chest wall. This disease is generally inoperable and requires up-front chemotherapy treatment for local and metastatic control. Despite advancements in therapeutics and the availability of a spectrum of drugs including targeted and systemic drugs, tumour response is not consistently positive. This makes the early assessment of tumour response to treatment potentially beneficial for refractory patients, as the treatment type and/or regimen can in principle be changed to a more effective treatment/regimen while avoiding adverse side effects and unnecessary costs. Currently accepted methods of response assessment are based on a reduction in the sum of largest diameters of target lesions or the largest diameter of unifocal disease [6]. However, clinically detectable tumour shrinkage does not typically occur until several weeks to months into treatment and assessments are only usually made using imaging months after the completion of treatment. In this light, imaging assessments of tumour biology and biochemistry have led to the discovery of novel biomarkers that can provide earlier indications of tumour response to therapy [7]. For instance, DW-MRI has been demonstrated clinically to predict response of breast tumours as early as after 1 cycle of chemotherapy. It is used to measure changes in the Brownian motion of water in the tumour tissue, which is thought to increase in responding tumours, due to a decrease in tumour cellularity [10]. In nuclear imaging, longitudinal PET imaging studies on breast cancer have shown a reduced fluorodeoxyglucose (FDG) uptake in responding tumours, detectable after one cycle of chemotherapy [11]. Additionally, diffuse optical imaging (DOI) studies on breast cancer have demonstrated a significant increase in hemoglobin concentration, water percentage, and tissue optical index, in responding patients as early as one week after chemotherapy treatment initiation [12]. The utility of these modalities in the clinic, however, is limited due to the requirement of contrast agents, low resolution, and health concerns related to the repeated use of radioactive material. In contrast, ultrasound offers short image acquisition times, relatively low cost, ionizing-radiation-free imaging, relatively high resolution images, and endogenous tumour contrast, the latter which eliminates the need for injection of external contrast agents. For these reasons, ultrasound has received recent widespread attention as a non-invasive therapy monitoring tool in addition to its well established diagnostic and visualization capabilities.

One of the ultrasonically detectable markers of tumour response is apoptotic cell death. The first QUS studies of cell death induced by a chemotherapeutic agent demonstrated *in vitro*, that cell death causes an increase in ultrasound echogenicity [53], [54]. These ultrasonic changes were later quantified by system-independent parameters including integrated backscatter coefficient (IBSC), MBF, and SS, all of which demonstrated an increase as a result of cell death [55]. This observation was experimentally determined to be related to the nuclear condensation and fragmentation that occur during apoptosis. The same ultrasonic pattern was observed in animal cancer models *in vivo*, which indicated significant increases in MBF and SS resulting from photodynamic therapy [25], or radiation therapy [26] of mouse tumour xenografts. More recently, a study on the low frequency (7 MHz) QUS assessment of an animal model of breast cancer treated with chemotherapy demonstrated that increases in the MBF and SI, but not SS, are strongly correlated to increases in cell death [27]. The MBF, SI, and SS parameters have been used in the past for other tissue characterization purposes, including the detection of prostate cancer, malignancies in lymph nodes, uveal melanoma, and liver disease [12] – [15]. By modelling the ultrasonic power spectrum as a linear approximation of the acoustic impedance autocorrelation, Lizzi *et al.* demonstrated that the SS is related to the scatterer size, SI is related to scatterer size and acoustic concentration, and MBF is related to the scatterer size, acoustic concentration, and attenuation [17]. Furthermore, the fitting of advanced form factor models to ultrasonic tissue backscatter has permitted the direct estimation of scattering properties of tissues, including average scatterer diameter ASD and AAC. A form factor is proportional to the Fourier transform of the spatial autocorrelation of the relative acoustic impedance between the scatterer and the background. The AAC parameter is a product of scatterer number density and the acoustic impedance of the scatterers relative to the background. These parameters have been demonstrated to be useful in differentiating between tumour types *in vivo*, including sarcoma versus carcinoma [57], and carcinoma versus fibroadenoma [21]. More recently, a clinical QUS study demonstrated significant increases in AAC in breast tumours of patients who responded well to chemotherapy treatment, compared to those who did not respond well, as early as one week after the start of treatment [23].

Various form factor models have been developed to describe tissue scattering, including the spherical Gaussian model (SGM) and the fluid-filled sphere model (FFSM) [31]. The SGM describes random scattering and a continuous variation of acoustic impedance between the scatterer and its surrounding, and whose impedance autocorrelation follows a Gaussian curve. In

contrast, the FFSM describes scattering by randomly distributed fluid-filled spheres, in which the cell nuclei are considered scatterers and the cytoplasm and the extracellular material are assumed to be background material. Good fits have been observed with both models depending from which kind of tissue ultrasound data is being obtained. Regardless, extensive evidence demonstrates that nuclear material contributes to backscattered ultrasound signals. There are multiple sources of experimental evidence suggesting the role of nuclear structure in potentially influencing significantly ultrasound backscatter signals. This evidence spans work *in vitro*, cellular experiments with cellular structure modifying agents, investigations of different cell types with different nuclear sizes, and work with isolated nuclei from viable and apoptotic nuclei [45], [53], [58].

In the work that has been examined to date on QUS detection of cell death, most experiments have been conducted at high ultrasound frequencies (above 20 MHz), and those conducted at lower ultrasound frequencies (<10 MHz) have used linear regression-based spectral analysis. At frequencies above 20 MHz, tissue penetration depth is affected by attenuation and primarily small-animal imaging has been performed. Clinical ultrasound imaging techniques employ linear array transducers operating at a lower frequency range (1-10 MHz), which more readily permit imaging of deeper tissue structures in breasts, kidneys, and livers, but with lower resolutions ( $150 \mu\text{m} - 1.5 \text{ mm}$ ). In addition, linear regression spectral analysis relies on a linear frequency dependence of the tissue power spectrum over the usable frequency range, which may not be appropriate for some tissues. On the other hand, solving the inverse scattering problem (i.e. estimating the scattering properties from knowledge of the backscattering model and the measured backscatter) permits direct estimation of scattering properties which may better reflect tissue composition, thereby permitting a comparison of scatterer property estimates with underlying tissue microstructure. If a set of acoustic parameters sensitive to cell death can be extracted from *in vivo* tumours using low frequency ultrasound, this makes potentially possible the non-invasive ultrasound monitoring of patients undergoing anti-cancer treatments.

Recently, several QUS parameters including means and texture features of MBF, SS, and SI and envelope statistics parameters were investigated as potential biomarkers of cell death *in vivo* [27]. However, in that study, one *in situ* end labeling (ISEL)-stained histology image from the central cross-section of the tumour was used to evaluate cell death extent, whereas QUS parameters were evaluated from multiple sections across the tumour. To obtain a better correspondence between

histology and ultrasound, I examined cell death extent from five ISEL sections across the tumour and from 5-10 ultrasound planes, I evaluated the corresponding ultrasound scattering properties of tumours undergoing cell death by estimating advanced parameters from factor-based scattering models. In addition, this study also examined the heterogeneity indices (HIs) of AAC and ASD (the standard deviations of AAC and ASD images) and initial tumour volume ( $V_i$ ) as potentially contributing factors to cell death response.

The overall objective of this study was to determine the optimal scattering model for estimating scattering properties of mouse models of breast tumours (SGM or FFSM) based on goodness of fit and scatterer size estimates, and using the optimal model's parameters to track their time-dependent cell death responses. Volumetric RF data were examined from human breast tumour xenograft-bearing mice which were treated with chemotherapy. In order to determine which model to use for scatterer properties estimation, two models, the SGM and the FFSM, were applied and compared in terms of ASD agreement with histological features, goodness-of-fit of the models to measured backscatter data, and the correlation of the extracted parameters to histologically determined cell death extent. Backscatter coefficients from tumour regions of interest (ROI) were estimated before and after treatment and form factor-based BSCs were fitted to the measured BSC to estimate ASD and AAC parameters. Statistical tests were performed to compare changes in ASD and AAC related to treatment against those related to tumour progression in control tumours. Multiple regression analyses were performed on changes in ultrasonic scattering properties and the extent of cell death observed histologically.

## 2.3 Methods

### 2.3.1 Experimental procedures

The experimental protocol was approved by the institution's animal care committee for humane and ethical use of laboratory animals. Human breast cancer cell line tumours (MDA-MB231, American Type Culture Collection, Manassas, Virginia, USA) were established by injection of  $1 \times 10^6$  cells in 50  $\mu$ L of PBS into the hind legs of severe combined immunodeficiency disease (SCID) mice and were permitted to grow to ~1 cm solid tumours. During treatment and imaging, mice were anaesthetized with 100 mg/kg ketamine, 5 mg/kg of xylazine and 1 mg/kg of

acepromazine (CDMV, St. Hyacinthe Quebec, Canada). Chemotherapeutic agents Paclitaxel and Doxorubicin (100mg/m<sup>2</sup>, 50mg/m<sup>2</sup>, respectively) were injected intravenously through the tail. Pulse-echo imaging was performed prior to injection and a predetermined amount of time after injection. Experimentation used 20 animals equally divided into 5 groups (n=4). The first 4 groups were the treatment groups with 4, 12, 24, and 48 hours of wait time after chemotherapy injection, respectively, and the fifth group served as untreated control tumours. Low and high-frequency ultrasound data were acquired using two imaging systems - a Sonix RP system (Sonix RP, Ultrasonix, Vancouver, Canada) operating a 7 MHz linear array transducer (L14-5/38) focused at 1.5 cm depth, with data sampled at 40 MHz, and a Vevo 770 system (Visual Sonics, Toronto, Canada) utilizing a 20 MHz transducer (RMV-710B) focused at 9 mm depth, and sampled at 420 MHz. Both systems were used to collect volumetric data with scan plane separations of ~0.5 mm in the conventional-frequency ultrasound and ~0.1 mm in the high-frequency ultrasound, depending on the size of the tumour. Tumour volumes were estimated by approximating the tumour volume as an ellipsoid and measuring the three axes (2a, 2b, and 2c) from *in vivo* three-dimensional B-mode images obtained using the high frequency ultrasound system, and using the formula  $\frac{4}{3}\pi abc$  to estimate the volume. The images obtained from the high frequency system were used for anatomical measurements since that system provided high resolution tumour images and more accurate tumour delineation.

### 2.3.2 Quantitative ultrasound analysis

For analyses, rectangular ROIs were selected from 5-10 tumour cross sections. These ROIs accounted for approximately 2/3 of the tumour cross sectional area in ultrasound images (approximately 5-10 × 5-10 × 5-10 mm). A sliding window analysis was performed on each ROI using Hanning-gated RF windows of 2 × 2 mm size for low frequency data, and 0.62 × 0.62 mm size for high frequency data, with 80% overlap between adjacent windows in both axial and lateral directions. The axial length of the RF segments were selected to cover approximately 10 wavelengths, which corresponded to the minimum size required to obtain reliable spectral estimates which are independent of window length (10 wavelengths) [59]. Each window spanned 13 RF scan lines in the low-frequency images and 11 RF scan lines in high-frequency images, respectively. The mean sample power spectrum of each RF window was computed by taking the squared magnitude of the FFT of the gated RF signal from every scan line and averaging the result across the scan lines. The normalized power spectrum,  $S(f)$ , was obtained using the reference

phantom technique (equation 1.5). Spectral normalization removes system-dependent effects such as transducer transfer function, beam forming, and diffraction artifacts. The reference material used for spectral calibrations was a well characterized phantom consisting of glass microspheres (5-40  $\mu\text{m}$ ) embedded in agar gel. The phantom was loaned from The Bioacoustics Research Laboratory, University of Illinois at Urbana-Champaign, for which details are available in the literature (phantom F1, table 2, in [60]). The reference BSC,  $\sigma_{br}$ , was measured using pulse-echo technique and planar reflector (plexiglas) calibration, using equation 1.13, and was cross-verified with the theoretical solution (see Appendix, p. 101). The measurement agreed with the theory (Fig. 7 of [60]). The estimated sample BSC,  $\widehat{\sigma_b}$ , was obtained using the reference phantom technique (equation 1.14). The SGM model (equation 0) was selected as the BSC model, for which  $\sigma_b$  functions were calculated for a range of candidate scatterer radii (1-200 $\mu\text{m}$ ). Scatterer properties, including ASD and AAC, were estimated through MASD fitting of  $\sigma_b$  onto  $\widehat{\sigma_b}$ . This method was described in section 1.6. The attenuation coefficient of the phantom was 0.15 dB/cm-MHz, which was determined through an insertion-loss experiment and fitting a straight line through the attenuation versus frequency data over the two system bandwidths (3-9 MHz and 10 – 25 MHz) [44]. The normalized power spectrum was then compensated for frequency-dependent attenuation using the point-by-point compensation method [31], assuming published attenuation coefficients of 2 dB/cm/MHz and 0.6 dB/cm/MHz for skin [61] and tumour [26], respectively. Two QUS features were defined from the parametric images of ASD and AAC – mean and heterogeneity index (HI). HI was defined as the standard deviation of the parametric image, as per Nam et al [22]. For comparison with cell death extent, changes in mean ASD and AAC ( $\Delta\text{ASD}$ ,  $\Delta\text{AAC}$ ), and changes in HI of ASD and AAC ( $\Delta\text{HI}_{\text{ASD}}$ ,  $\Delta\text{HI}_{\text{AAC}}$ ) before and after treatment administration were considered. The mean coefficient of determination,  $\langle R^2 \rangle$ , which indicates the goodness of fit between measured and a theoretically derived backscatter coefficient was also calculated. Finally, QUS parametric images were constructed by superimposing colored pixels, whose colors were associated with QUS parameter estimate values and locations associated with the sliding window locations, on the original grey scale B-mode image of the tumour [34].

### 2.3.3 Histology analysis

Histology analysis was performed on excised tumour sections which were fixed in 5% formalin (volume/volume) in PBS. Each fixed specimen was sectioned into five slices stained for hematoxylin and eosin (H & E) and five slices stained for ISEL, with 50 $\mu\text{m}$  spacing. The cell death

fraction (CDF) of each tumour was determined, using ImageJ (National Institutes of Health, Bethesda, MD) by manually contouring the ISEL-positive (brown stain) area and the total tumour area and taking the ratio of the two areas. The mean CDF for each tumour was obtained by averaging the CDFs from all the five sections. High-magnification images were obtained using a Leica DC100 microscope with a 40 $\times$  objective and a Leica DC100 camera connected to a 2-GHz PC running Leica IM1000 software (Leica GmbH, Wetzlar, Germany). Areas which were identified as ISEL-positive for CDF calculation were verified under high-magnification to contain more than 50 % apoptotic cells. Mean cell and nucleus sizes were estimated by manually measuring the diameters of approximately 100 cell / nucleus samples in the ISEL-stained sections under high magnification.

### 2.3.4 Statistical Analysis

In order to evaluate of the goodness of fit of each form factor model, the mean coefficient of determination,  $\langle R^2 \rangle$ , was computed from all untreated tumours. To determine whether the changes in the ASD/AAC parameters of treated tumours were statistically significantly different from those of untreated tumours, t-tests (unpaired, two-tailed,  $\alpha=0.05$ ) or Mann-Whitney tests ( $\alpha=0.05$ ) were applied to the data, depending on the distribution type. A p-value less than 0.05 was considered to be statistically significant. Prior to performing hypothesis tests, a Shapiro-Wilk normality test was first performed on the data to determine whether to use a parametric test (t-test) or non-parametric test (Mann-Whitney). The correlations between CDF and BSC parameters were evaluated using multiple linear regression analysis. The Pearson product-moment correlation coefficient,  $r^2$  metric, was used to evaluate the strength of the correlation. For analysis of correlation between QUS and histology (CDF), two scenarios were considered: multiple regression analysis on the set ( $\Delta AAC$ ,  $\Delta ASD$ ,  $\Delta HIAAC$ ,  $\Delta HI_{ASD}$ ), and multiple regression analysis on the set ( $\Delta AAC$ ,  $\Delta ASD$ ,  $\Delta HIAAC$ ,  $\Delta HI_{ASD}$ ,  $V_i$ ). The second scenario examined the effect of initial tumour volume on the BSC parameters and hence on the prediction of cell death response.

## 2.4 Results

### 2.4.1 Histological assessment of treatment effects

Figure 2-1 presents H&E and ISEL stained sections of representative control and treatment time groups. Whereas control tumours were characterized by multiple distinct nucleoli-containing cells and microvessels, treated tumours were characterized by loss of microvessels, a decrease in the number of cells with distinct nucleoli and increase in the number of cells with condensed nuclei in H&E sections, and treated tumours also demonstrated an increase in areas of brown stains in the extracellular space in ISEL sections. The strong focal stains in the H&E and blue-brown focal stains in the ISEL sections were consistent in appearance with the nuclear condensation stage of apoptosis and the brown stains in the extracellular space in the ISEL were consistent with the appearance of fragmented DNA and cellular debris associated with the late stages of apoptosis. Both H&E and ISEL sections indicated that as time progresses from 0 to 24 hours after the onset of chemotherapy, tumours changed from a heterogeneous mixture of dead and viable cells to an almost homogeneous tissue of dead cells. At 48 hours, tumours appeared to have entered the final stages of cell death marked by nuclear degradation, as evident from a loss of cells with visible nuclei. The mean changes in cell and nucleus size with treatment time are presented in Figure 2-1E. In general, reductions in cell and nucleus size were observed resulting from chemotherapy as time progressed, apparently plateauing at 48 hours. Plots of mean cell death fraction versus treatment condition are presented in Figure 2-1F. Analysis of cell death obtained from ISEL-stained histology images revealed a monotonic increase in cell death with time from treatment onset, peaking at 24 hours, after which cell death dropped, but remained higher than cell death observed in controls. The CDF was statistically significantly increased at 24 hours and 48 hours, compared to the control group (unpaired t-test,  $p<0.05$ ).

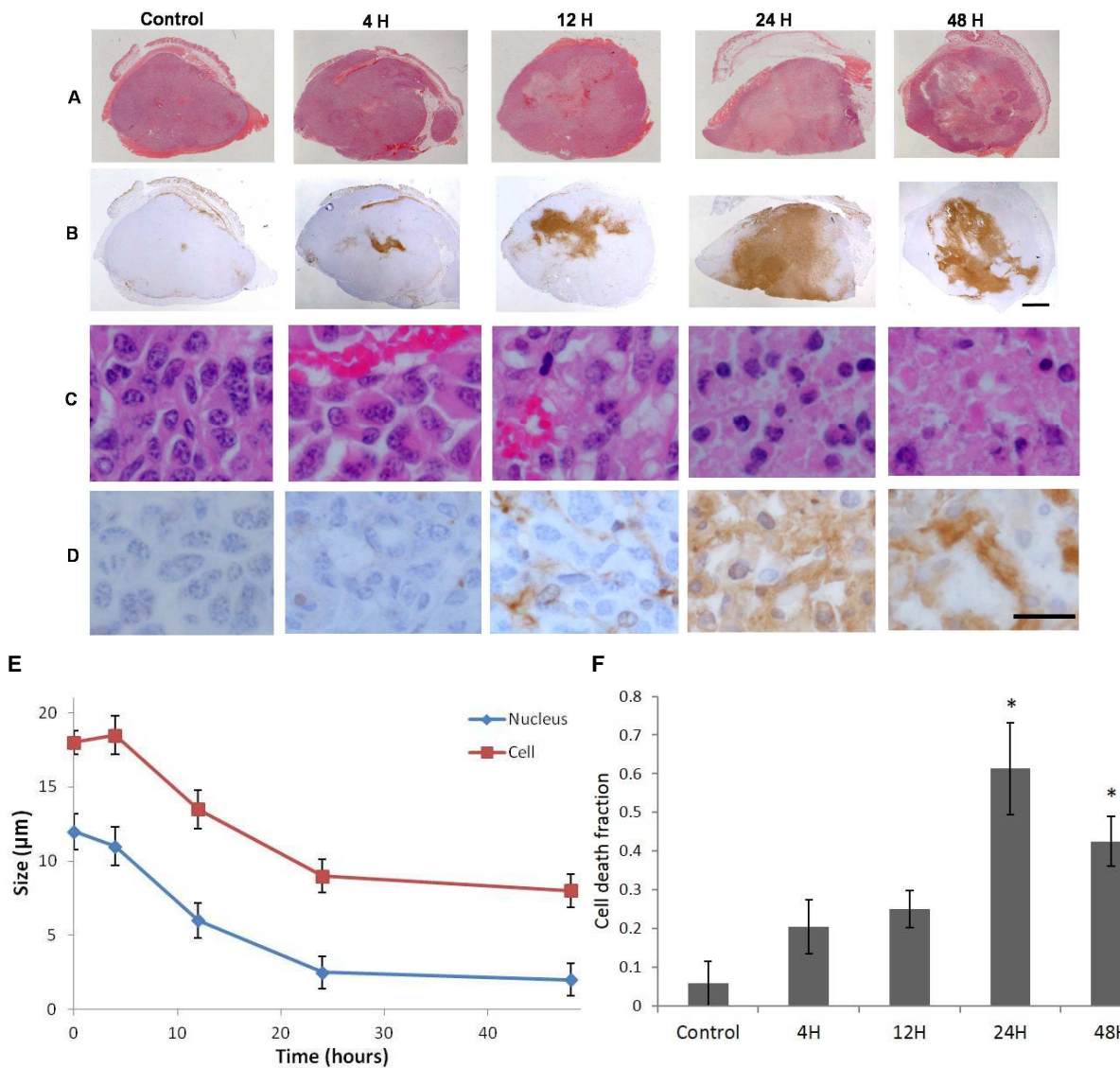


**Figure 2-1.** (A-D) Histology images of representative control, 4-hour, 12-hour, 24-hour, and 48-hour chemotherapy-treated MDA-231 tumours, from left to right, respectively. (A) Low-magnification H&E stained sections. (B) Low-magnification ISEL stained sections (C) High-magnification H& E stained section to highlight nuclear material. (D) High-magnification ISEL section to highlight fragmented DNA. The control tumour features rapidly dividing cells with large nuclei. The treated tumours feature reduced nuclear size (nuclear condensation), fragmented nuclei, and dead cellular components filling the extracellular space (brown stains). The low-magnification scale bar represents 1 mm. The high-magnification scale bar represents 25  $\mu\text{m}$ . (E) Plots of mean cell and nucleus diameters versus treatment time (0 to 48 hours), estimated from H& E histology sections. Error bars represent standard error of the mean. (F) Plot of the mean cell death fractions versus time. Error bars represent the standard error across the tumour samples for each time condition. Statistical significance: \* =  $p < 0.05$ .

## 2.4.2 Tumour volume analysis

Plots of mean *in vivo* tumour volume pre- and post-treatment for each treatment condition are presented in Figure 2-2. It is important to note that the horizontal axis does not represent a time-scale, it represents the treatment groups. The volumes were estimated based on an ellipsoid model using B-mode images obtained from the high-frequency system. Additionally, the percent error in initial tumour volumes were computed as follows: 74%, 27%, 40%, 20%, and 67%, for control, 4-hour, 12-hour, 24-hour, and 48-hour groups, respectively. Percent error of the mean initial volume was defined as the standard deviation of the initial tumour volume across animals, divided by mean initial tumour volume divided by square root of the number of animals in that group. Initial tumour volumes had large variations (varied as much as 74%). In both cases of treatment and control, tumour volume increased slightly in time, however, comparison of pre- and post-treatment volumes performed through paired t-test for each condition revealed no statistically significant differences ( $p > 0.05$ ).

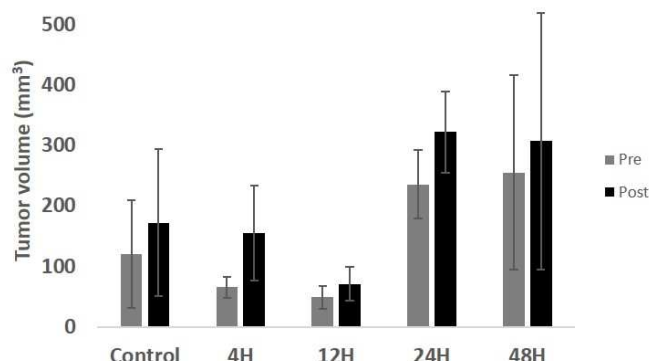


**Figure 2-2.** Plot of *in vivo* tumour volumes before (pre) and at predefined length of time after chemotherapy injection (post). Percent errors of the initial tumour volumes for each group were 74%, 27%, 40%, 20%, and 67%, for control, 4-hour, 12-hour, 24-hour, and 48-hour groups, respectively.

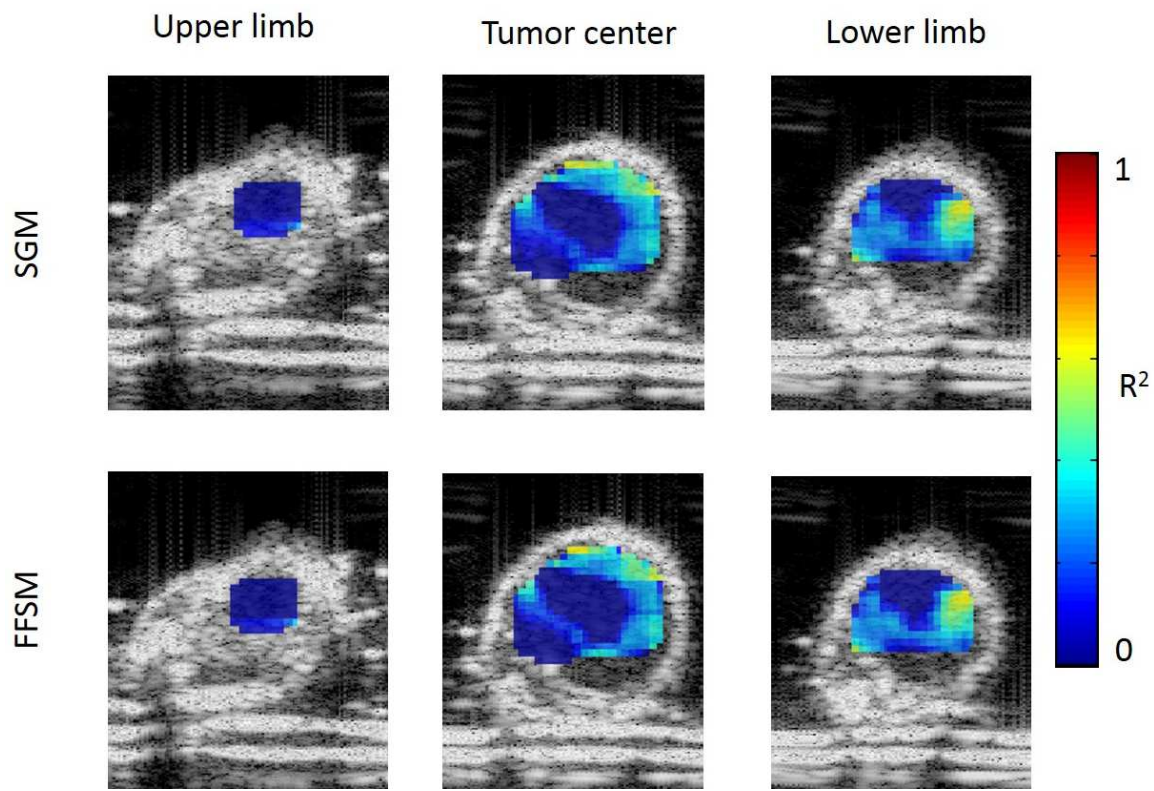
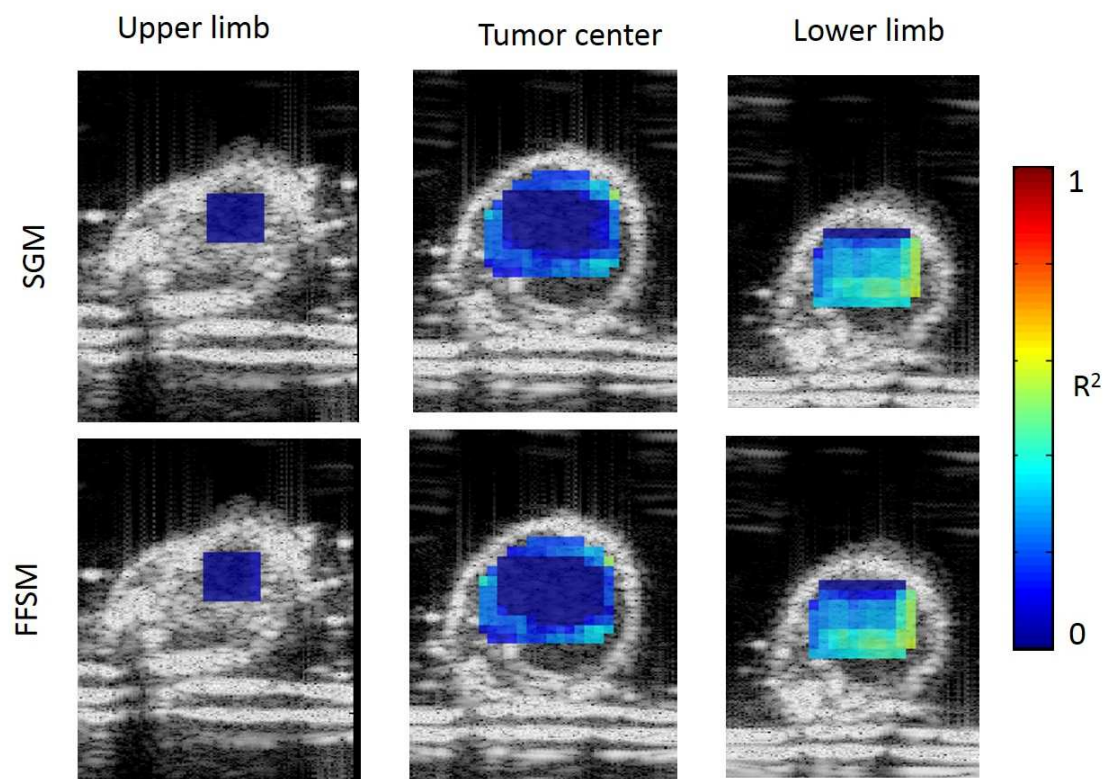
## 2.4.3 Tissue microstructure models

Tumour microstructure was examined microscopically in H&E and ISEL stained sections in order to identify and characterize structures that could inform models of ultrasonic scattering. Figure 2-1, column 1, presents H&E and ISEL sections of a representative control tumour in low magnification

and high magnification views. In the H&E sections, tumours appeared to be predominantly composed of tumour cells (purple-stained nuclei), with infrequent microvessels (red-pink stained), and connective tissue (cyan-pink stained). Microvessels were only sparsely observed and had a size of  $20 \pm 2 \mu\text{m}$ . The tumour cells dominated the tumour tissue. Both the H&E and ISEL sections show densely packed cells with high mitotic indices and large nuclei ( $18 \pm 3 \mu\text{m}$  diameter), containing visible nucleoli. Table 2-1 lists the average cell size (histology), ASD, AAC, and mean  $R^2$  ( $\langle R^2 \rangle$ ) goodness of fit values obtained from all pre-treated tumour BSC at low and high frequencies using both models. Pre-treatment data was used because it permits the characterization of MDA tumours in terms of scattering properties without the necessity to consider complex tissue microstructures which can result from cell death. At the lower frequency range, both models yielded large ASD values ( $109 \pm 12 \mu\text{m}$  for SGM,  $95 \pm 9 \mu\text{m}$  for FFSM,  $p < 0.05$ ). However, the SGM provided a better fit to the measured backscatter data ( $\langle R^2 \rangle = 0.21$ ) compared to the FFSM ( $\langle R^2 \rangle = 0.07$ ). For this reason, the SGM was used going forward and multiple linear regression analysis was performed using ASD and AAC features extracted from this model. For the high-frequency data, both models provided smaller ASD estimates ( $45 \pm 7 \mu\text{m}$  for SGM and  $38 \pm 1 \mu\text{m}$  for the FFSM), and the FFSM yielded a statistically significantly smaller ASD compared to the SGM ( $p > 0.05$ ). AAC can take on negative values, since it is expressed in  $\text{dB}/\text{cm}^3$ . The dB units arise from the logarithm applied to the BSC before MASD fitting is performed. The appropriateness of the SGM and FFSM models for representing MDA tumour backscatter characteristics may at first appear concerning due to the low  $\langle R^2 \rangle$  values. This is due to the tumour heterogeneity, resulting in a highly heterogeneous  $R^2$  distribution over the tumour volume, as demonstrated in Figure 2-3. The tumour ROI contains regions of good fit and regions of poor fit. As shown, the best model fit does not always occur in the center of the tumour, but sometimes in the periphery, in this case, the best fit occurred in the lower limb. Additionally, Figure 2-3B demonstrates that the use of a larger RF window size ( $3 \times 3 \text{mm}$ ) results in higher  $R^2$  values as compared to  $2 \times 2 \text{mm}$  window size used in this study (Figure 2-3A). However, since  $3 \times 3 \text{mm}$  was too large to fit in some of the smaller tumours, I used  $2 \times 2 \text{mm}$  as the standard window size. In the discussion section, an explanation will be provided for why reasonable scatterer size estimates can be obtained regardless of low  $R^2$  values.

**Table 2-1.** Comparison of ASDs ( $\mu\text{m}$ ) and AACs ( $\text{dBr/cm}^3$ ) estimated using the SGM and FFSM models at low and high frequencies (LF and HF) with mean histological measurement of tumour cell size.  $R^2$  is a measure of the goodness-of-fit of the model BSCs to the measured BSCs.  $\pm$  represents standard deviations of the parameter over the tumour samples. Estimates were obtained from all tumours prior to treatment.

Cell diameter ( $\mu\text{m}$ )	$18 \pm 3$					
	SGM			FFSM		
	ASD	AAC	$R^2$	ASD	AAC	$R^2$
7 MHz	$109 \pm 12$	$5 \pm 9$	0.21	$95 \pm 9$	$7.35 \pm 9$	0.07
20 MHz	$45 \pm 7$	$32 \pm 19$	0.08	$38 \pm 1$	$-11 \pm 11$	0.06

**A****B**

**Figure 2-3.** Illustration of the spatial distribution of  $R^2$  goodness of fits of the SGM and FFSM models over different tumour areas. Presented are  $R^2$  images overlaid on analyzed tumour ROIs over three tumour cross-sections: upper limb, tumour center, and lower limb. Data is presented from the low-frequency study with (A)  $2 \times 2$  mm RF windows and (B)  $3 \times 3$  mm RF windows.

Figure 2-4 presents combined low and high frequency plots of measured BSC and corresponding theoretical BSCs based on the SGM and FFSM models obtained from one of the treated tumours. The BSCs were obtained from an RF window at the center of the tumour ROI at low and high frequencies. Results are shown before and 24-hours after chemotherapy injection.  $R^2$  values ranged from 0.55 to 0.71. The FFSM model provided a better fit at high frequency at pre-treatment whereas no considerable model differences were observed post-treatment. These values were higher compared to the values reported in Table 2-1, because Table 2-1 exports the mean of mean  $R^2$  where  $R^2$  was averaged across all windows in the tumour ROI and then across all pre-treatment tumours. However, the  $R^2$  reported in Figure 2-4 were obtained from one RF window from one animal. Generally, I observed lower  $R^2$  values in more heterogeneous tumours. An increase in the BSC magnitude can be observed from pre-treatment to post-treatment at both frequency ranges. This trend is consistent with the trend observed in AAC, which will be demonstrated in the next section.

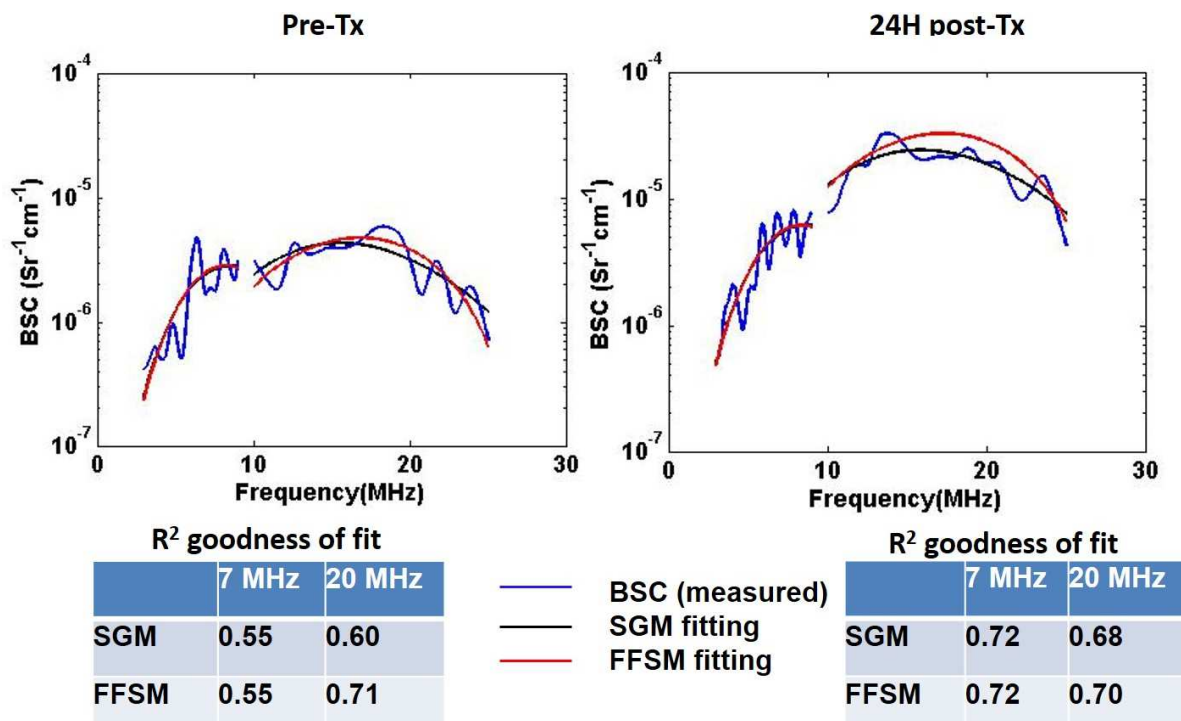


**Figure 2-4.** Combined low and high frequency plots of measured BSC and theoretical BSCs based on the SGM and FFSM models obtained from an animal in the 24-hour treatment group. Left: pre-treatment. Right: post-treatment. The BSCs were obtained from an RF window at the center of the tumour ROI. Corresponding  $R^2$  goodness of fit values are shown below the plots.

#### 2.4.4 Ultrasonic scattering properties of cell death

Figure 2-5A-B presents AAC and ASD images obtained using the SGM from high and low-frequency ultrasound imaging, respectively. The corresponding ISEL section post-treatment is also presented. The cytotoxic effect of the treatment could be readily visualized in the ISEL section (Figure 2-5C), demonstrating predominantly brown stained areas indicative of cell death. The AAC images demonstrated that AAC increases considerably as a result of cell death (statistically significant) at both frequencies, whereas the ASD was less sensitive to cell death at both frequencies.

Figure 2-6A presents mean changes in AAC corresponding to different treatment conditions (control, 4, 12, 24, and 48 hours) obtained from low and high-frequency RF data. Results demonstrated a parallel trend in the AAC changes with treatment conditions as did the CDF in Figure 2-1F. Initial observations suggested that AAC nominally increased proportionally with time, peaking at 24h, following the observations for CDF. However, an unpaired t-test revealed no statistical difference in AAC changes between 4 hours and the control groups, between 12 hours and control group, and between 48 hours and the control group. Rather, a statistically significant change could be detected only after 24 hours for both the low-frequency and high frequency data ( $p = 0.003$  and  $0.043$ , respectively).

A stepwise multiple linear regression analysis of CDF versus BSC parameters ( $\Delta AAC$ ,  $\Delta HI_{AAC}$ ,  $\Delta ASD$ ,  $\Delta HI_{ASD}$ ) revealed the single-most correlated parameter to be  $\Delta AAC$  with a correlation ( $r^2$ ) of 0.399 and the most correlated multiparameter QUS model to be a linear combination of  $\Delta AAC$  and  $\Delta HI_{ASD}$  with a correlation of 0.639, as presented in Table 2-2. Furthermore, when initial tumour volume ( $V_i$ ) was added to the model on the working hypothesis that biological changes in tumour structure associated with tumour growth may affect data, the correlation further increased to 0.744 (Table 2-2). Presented in Table 2-2, column 3, are p-values of significance of one-way ANOVA tests, demonstrating the statistical significance of the correlations between CDF and each

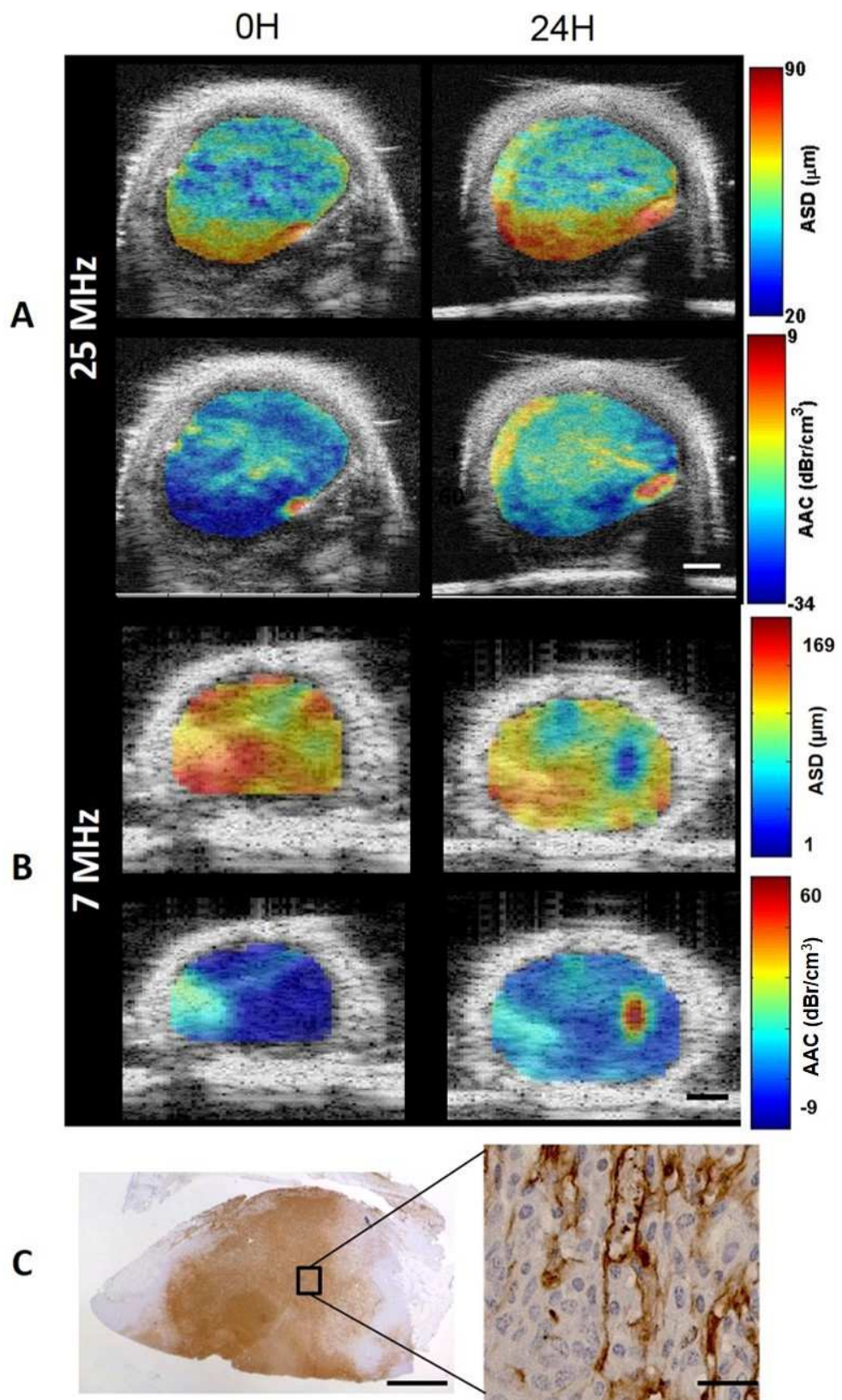
predictive model (where  $p<0.05$  indicates a significant correlation). All predictive models were found to have a statistically significant correlation. Stepwise multiple linear regression analysis of CDF versus tumour  $V_i$ -normalized BSC parameters (i.e. BSC parameter  $\times V_i$ ) determined the best predictor model to be  $\Delta AAC_{VN}$  with  $r^2=0.688$  ( $VN$  stands for volume-normalized). An immediate observation was a considerable increase in  $r^2$  attributed to the normalization of  $\Delta AAC$  to initial tumour volume (i.e. from 0.399 to 0.688). Normalization by division of each BSC parameter by  $V_i$  resulted in poorer correlation (no significant correlation). Table 2-3 lists the model parameters, their standardized coefficients, and their individual correlations to CDF for case 1, when  $V_i$  was included in the correlation analysis and case 2, when all BSC parameters were normalized to  $V_i$  prior to correlation analysis. In case 1,  $\Delta AAC$  had the strongest correlation ( $r^2 = 0.399$ ), while  $V_i$  and  $\Delta HIA_{ASD}$  had no significant correlation individually. In case 2,  $\Delta AAC_{VN}$  had the strongest correlation ( $r^2 = 0.688$ ), and addition of more parameters did not improve the correlation. In Table 2-3, column 5, one-way ANOVA p-values of significance are also presented. Despite  $\Delta HIA_{ASD}$  and  $V_{tumor}$  being statistically non-significant individually, the QUS model in case 1 was nevertheless significant ( $p<0.001$ ), as was the case for  $\Delta AAC_{VN}$  ( $p<0.001$ ). Figure 2-6B-C presents scatter plots of CDF versus model predictions with lines of least squares fit. Figure 2-6B presents the prediction obtained using the  $(\Delta AAC, \Delta HIA_{ASD})$  model whereas Figure 2-6C presents the prediction obtained using the  $(\Delta AAC, \Delta HIA_{ASD}, V_i)$  model.

**Table 2-2.** Stepwise multiple regression results. The second column presents the standardized coefficient of each model and the third column presents the model's correlation to CDF ( $r^2$ )

Predictive model	Correlation to CDF	ANOVA p-value
<b><math>\Delta AAC</math></b>	0.399	0.009
<b><math>\Delta AAC, \Delta HIA_{ASD}</math></b>	0.639	<0.001
<b><math>\Delta AAC, \Delta HIA_{ASD}, V_{tumor}</math></b>	0.744	<0.001

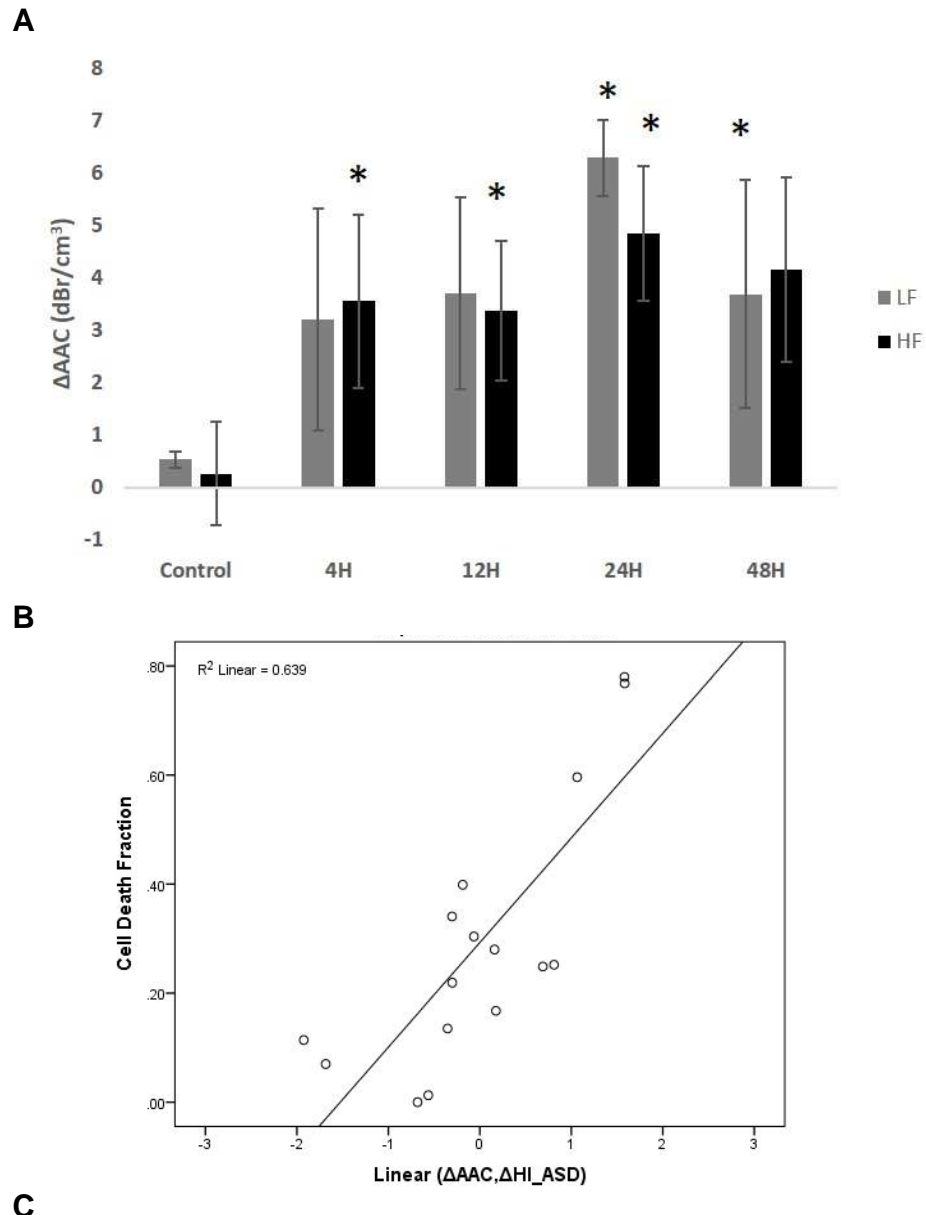
**Table 2-3.** Stepwise multiple regression results for the two cases - with and without tumour volume normalization (separated by a horizontal line). The second column presents the standardized coefficient of each parameter and the third column presents the parameter's correlation to CDF ( $r^2$ ). NS indicates non-significant results ( $p>0.05$ ).

Case	Predictive model parameter	Standardized Model Coefficient	Correlation to CDF	ANOVA p-value
Case 1	<b><math>\Delta AAC</math></b>	0.765	0.399	0.009
	<b><math>\Delta HI_{ASD}</math></b>	0.429	NS	NS
	<b><math>V_{tumor}</math></b>	0.336	NS	NS
Case 2	<b><math>\Delta AAC_{VN}</math></b>	0.829	0.688	<0.001



**Figure 2-5.** Pre- and post- treatment (24h) images of the central cross section of a sample MDA-231 tumour which received chemotherapy treatment. (A) and (B) show ASD and AAC images

overlaid on the B-mode image obtained from the high-frequency and low frequency systems, respectively, and (C) shows low and high magnification ISEL-stained histology sections of the tumour post treatment. B-mode scale bar represents 2 mm. Low magnification represents 1mm. High magnification represents 25 $\mu$ m.



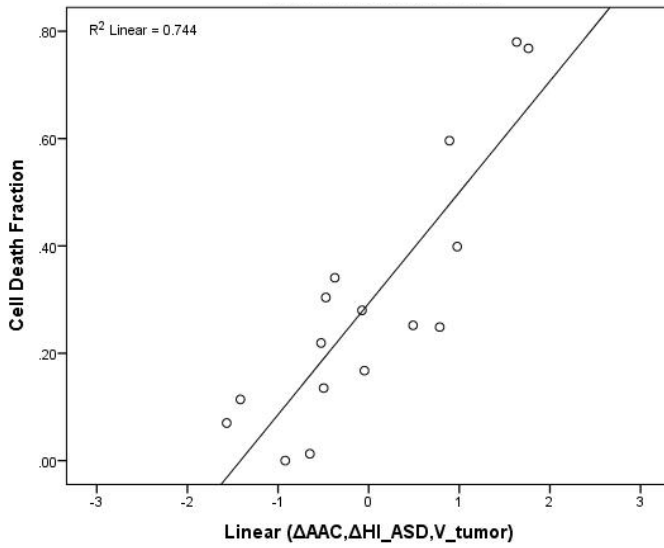


**Figure 2-6.** Results of QUS analysis of cell death. (A) Plot of  $\Delta AAC$  versus time from treatment onset obtained using the low and high frequency systems. Error bars represent the standard error across the tumour samples for each time condition. Statistical significance: \* =  $p < 0.05$ . (B) Scatter plot of CDF versus the predictive model ( $\Delta AAC$ ,  $\Delta HI_{ASD}$ ),  $r^2=0.639$ . (C) Scatter plot of CDF versus the predictive model ( $\Delta AAC$ ,  $\Delta HI_{ASD}$ , and  $V_i$ ),  $r^2 = 0.744$ .

## 2.5 Discussion and Conclusions

Ultrasound is widely preferred over currently available breast imaging modalities due to its relatively low cost, high spatial and temporal resolution, safety, and independence from external contrast agents. This study demonstrated that scattering properties can be potentially used as biomarkers of treatment response-related cancer cell death, at high (20 MHz) and low (7 MHz) ultrasound frequencies. Examination of tumour histopathology revealed clusters of tumour cells and microvessels as dominant features which could serve as potential scatterers of ultrasound with sizes of  $18 \pm 3 \mu\text{m}$ , and  $20 \pm 2 \mu\text{m}$ , respectively. Two scattering properties, ASD and AAC, were estimated using the SGM and FFSM models. Analysis of ISEL-stained histopathology revealed a progressive increase in cell death extent with time up to 24 hours from treatment initiation, after which cell death decreased due to nuclear and cellular degradation (48 hours). Changes in AAC related to cell death were consistent with changes in surrogate measures of AAC (i.e. MBF and SI) that were assessed in previous works [26], [27], and changes in backscatter intensity observed in previous *in-vitro* studies [54], [55]. In the study here, the use of a wider analysis bandwidth permitted a better characterization of the frequency-dependent backscatter of treated and untreated

tumours, by fitting advanced scattering models as opposed to applying a simple linear regression to the power spectrum within a narrow bandwidth. Physical insight into the link between low-frequency scattering properties and underlying microstructure of the dying tumours was gained to help explain previous QUS findings. It is likely that these findings stem from changes which correspond to scattering from a mixture of microvessels and larger tumour cell clusters.

Our working model of the ultrasonic scattering properties related to cell death is that nuclear changes are responsible for the increase in AAC. Since AAC is the coefficient of the BSC, it is related to the backscatter amplitude. Previous *in vitro* and *in vivo* studies suggest that changes in the magnitude and frequency dependence of ultrasound backscatter with cell death arise from coincident changes in the nuclear structure of the cell [25], [45], [53].

As tumour structure becomes more complex in association with tumour growth there are further complexities which are linked to potential sources of ultrasound backscatter. The degree of fit between the SGM and FFSM models and the measured BSC at both low and high frequency ranges were consistent with the work of others ( $R^2=0.1-0.3$ ) [57]. These previous studies have also demonstrated that the degree of model fit to the measured backscatter does not reflect the accuracy of the scatterer size estimates (i.e. agreement between scatterer size and observed microstructure) and models which fit the measurement with less than 0.50  $\langle R^2 \rangle$  can nevertheless estimate the scatterer properties reasonably well [57].

The scattering models that were applied in this study were not used to characterize scattering by individual cells, rather, it is hypothesized that clusters of tumour cells or microvessels were detected as scatterers. Immunohistochemical examination of tumours 24 hours after therapy exposure revealed positive staining covering nearly 60% of the tumour. Recall that AAC is related to the product of scatterer number density and relative acoustic impedance. Thus, the observed increases in AAC due to cell death may have been caused by changes in the acoustic impedance of the scatterers relative to the background, since nuclear fragments and cellular debris filled the extracellular space. For this reason potentially, AAC showed a stronger correlation to cell death ( $R^2_{SGM}=0.40$ ) compared to ASD ( $R^2_{SGM}$  was non-significant).

An important finding in this study was that initial tumour volume measurements demonstrated large variations (as high as 74 % of the mean value). This variation was likely due to differences

in tumour growth. The correlation between  $\Delta$ AAC and CDF improved when  $\Delta$ AAC was normalized to initial tumour volume (from 0.399 to 0.688) as this accounted for variations in initial tumour volume and therefore any effects of tumour necrotic centers. As tumours grow beyond 7–10 mm in our experience more vascularization occurs and also baseline levels of necrosis are thought to arise from transient hypoxia. The reduction in cell size observed histologically and associated with cell death could not be detected by scatterer property estimates, as the ASDs estimated by both models were considerably larger than cells (5 times larger at low frequency and 2 times larger at high frequency). In a tumour study, comparing three form factor models for characterizing mammary carcinoma and sarcoma tumours in mouse models, Oelze *et al.* demonstrated that the SGM best predicts the size of cell scatterers, although the FFSM provided better fits to the backscatter power [57]. In contrast, the high-frequency backscatter data here were fitted better with the SGM model. This suggests that depending on the tumour type, the SGM model may also describe scattering by an aggregate of cells, rather than individual cells, as was previously hypothesized by Oelze *et al.* [57].

Analysis of changes in AAC with treatment indicated greater increases in AAC estimated from low-frequency data compared to those estimated from high-frequency data, after 24 hours (nearly 2 dBr higher). This observation was consistent with previous findings *in-vitro*: in the 10–30 MHz range, cell samples treated with chemotherapy demonstrated a 5 dBr increase in backscatter amplitude, while in the 30–50 MHz range, a lesser 2 dBr increase was observed [62].

Multiple regression analysis of QUS versus CDF demonstrated the “best” single parameter based on the experiments conducted to be  $\Delta$ AAC and the “best” multiparameter model to be  $\Delta$ AAC,  $\Delta$ H<sub>i</sub>ASD, and V<sub>i</sub>. It is believed that  $\Delta$ H<sub>i</sub>ASD reflects changes in heterogeneity of the tumour in response to therapy. The improvement obtained by adding V<sub>i</sub> to the regression model suggests that initial tumour volume affects the BSC parameters and CDF and is an important parameter. The rationale is that larger tumours often develop necrotic and/or hypoxic regions which could potentially alter the acoustic scattering properties.

In a recent clinical QUS study which examined changes in AAC and ASD estimated from the FFSM fitting of the BSC from patient breast tumours, significant increases in AAC were observed as early as one week after the start of treatment [23]. However, no corresponding histopathological data was available during the treatment to compare AAC changes with microstructural changes in

the tumour. Rather, AAC changes measured during the treatment were compared with clinical response determined based on tumour size reduction at the end of the treatment which generally lasts several months. The low-, and clinically relevant - frequency pre-clinical study performed here, backed by high-frequency data, suggests that the increases in AAC observed clinically during anti-cancer treatment, is likely associated with cell death response. However, the findings of this study suggests that other factors such as tumour heterogeneity and initial tumour volume should also be taken into account when assessing tumour response.

The fact that SGM form factor fitted the measured BSC better compared to the FFSM form factor may owe to the theory that the SGM model better reflects the acoustic impedance autocorrelation function of the tumour. As mentioned previously, form factors are proportional to the Fourier transform of the spatial autocorrelation of the relative acoustic impedance between the scatterer and the background. A continuous change in acoustic impedance between the scatterer and its background, which is assumed in the SGM model, may better reflect the interface between tumour cell clusters and the extracellular matrix, as opposed to a discrete change in acoustic impedance described by the FFSM model.

In all, scatterer property-based QUS biomarkers, including  $\Delta AAC$ ,  $\Delta HIASD$ , and  $V_i$  demonstrated a favorable correlation to cell death extent (CDF). The results of this work are promising for the development of QUS imaging methods for monitoring of breast tumour response to anticancer therapy, requiring only a standard clinical US scanner equipped with QUS processing and imaging software.

### **3 Quantitative ultrasound characterization of locally advanced breast cancer**

### 3.1 Overview

Purpose: Identification of tumour pathological characteristics is an important part of breast cancer diagnosis, prognosis, and treatment planning, but currently requires biopsy as its standard. Here, I investigated a non-invasive quantitative ultrasound method for characterization of breast tumours in terms of their histological grade, which can be used with clinical diagnostic ultrasound data.

RF data from 57 locally advanced breast cancer patients were analyzed as part of this study. Among these patients, 42 normal breast tissues and 42 breast tumours were selected for characterization of normal versus cancer in the breast. For tumour grade characterization, 7 patients had grade I tumours and 50 had grade II-III tumours. Six quantitative ultrasound parameters were simultaneously extracted from tumour and normal breast tissue regions in the RF data, including mid-band fit, spectral slope, 0-MHz intercept, scatterer spacing, average scatterer diameter, and average acoustic concentration. For tumour grade characterization, a seventh parameter was included in the analysis - attenuation coefficient estimate. Histopathological information from breast biopsy was used to identify the tumour location(s) with the guidance of an oncologist during the scans. Parametric maps were generated corresponding to the region of interest, from which four textural features, including contrast, energy, homogeneity, and correlation were determined as additional potential tumour characterization parameters. Data were examined on the basis of tumour versus normal tissue and tumour subtypes based on histological grade (grade I versus grade II-III).

Results: All six quantitative ultrasound parameters were found to be statistically different between tumour and normal tissue ( $p < 0.05$ ). The combination of average acoustic concentration and mean scatterer spacing could separate tumour from normal tissue with 88% accuracy, while the addition of effective scatterer diameter to the combination did not provide substantial improvement (89% accuracy). For tumour grade characterization, linear discriminant analysis of the means of the parametric maps resulted in classification accuracy of 79 %. On the other hand, the linear combination of the texture features of the parametric maps resulted in classification accuracy of 82 %. Finally, when both the means and textures of the parametric maps were combined, the best classification accuracy was obtained (86 %).

Conclusions: Textural characteristics of quantitative ultrasound spectral parametric maps provided discriminant information about different types of breast tumours. In particular they significantly improved the results of ultrasonic tumour characterization whereas conventional mean values used alone tended to be poorer. As such, this study suggests that texture-based quantitative ultrasound

analysis of in-vivo breast tumours can provide complementary diagnostic information about tumour histological characteristics.

## 3.2 Introduction

An accurate diagnosis of breast tumours plays an important role in prognosis and therapy planning, and can improve overall survival. X-Ray mammography is currently the primary imaging modality for breast examinations. However, mammographic sensitivity declines substantially with increasing breast density particularly in young women [63]. Clinical ultrasound, when performed in conjunction with mammography, has been reported to increase diagnostic accuracy from 78% to 91% [64]. However, due to the many instrument parameters that can be chosen during an ultrasound imaging session, a comparative interpretation of conventional B-mode images becomes difficult when different imaging settings are applied or when different ultrasound machines are used. In addition, B-mode images, which are used by radiologists for breast examination, lack readily accessible information about microstructural properties of soft tissues. This information is lost when raw ultrasound data, or RF data, is converted to gray-scale pixels. QUS techniques, which examine the frequency-dependence of backscatter from tissues (from analyzed RF data), have been developed to overcome these limitations. Such techniques have been applied *in vivo* in a variety of applications to reveal information about tissue microstructure, enabling the differentiation of disease from non-disease, and the characterization of disease into its subtypes. Applications include the characterization of tissue abnormalities, such as those in the eye, prostate, and myocardium and to detect cancer in the lymph nodes [13]–[16]. Specifically, QUS parameters including ASD and AAC (related to effective scatterer number density and relative acoustic impedance) have demonstrated the potential to be used to distinguish between mouse models of mammary carcinoma and rat models of fibroadenoma. These parameters can be obtained by fitting a form factor model, such as the Gaussian form factor, to the measured backscatter coefficient [34]. In order to avoid complex model fitting, basic spectral parameters extracted via a linear regression analysis of the RF power spectrum, including MBF, SS, and SI, have also been used for tissue characterization previously [13]–[16]. By modelling the ultrasonic power spectrum as an acoustic impedance autocorrelation function, Lizzi *et al.* demonstrated that parameters, extracted from a linear fit to the power spectrum within the usable frequency bandwidth, are related to the scattering properties of the tissue of interest. In particular, they found that SS is related to effective

scatterer size, SI is related to effective scatterer size and acoustic concentration, and MBF is related to effective scatterer size, acoustic concentration, and attenuation [18]. However, power spectrum measurements are affected by the inherent frequency-dependent attenuation of intervening tissues, requiring correction for accurate estimates of scattering properties.

Frequency-dependent attenuation has also been shown to be a useful parameter in characterizing tissues, especially tumours and normal tissues of the breast [44]. Furthermore, a previous clinical study found large variations in the ACE among breast tumours ( $1.16 \pm 0.8$  dB/cm/MHz), suggesting different tumour types [22]. Another parameter, SAS, has been investigated as a tissue characterization parameter when the tissue of interest contains detectable periodicity in its structural organization. Previous studies have investigated the potential of SAS mainly for characterizing diffuse diseases of the liver [38]–[40]. More recently, scatterer spacing has also been applied to characterize human breast tumours in terms of normal breast tissue, fibroadenoma, simple carcinoma, and infiltrating papillary carcinoma [42]. However, subtle differences were found between the scatterer spacing values estimated from these tissue types.

Whereas the conventional quantitative ultrasound spectral parameters discussed above describe the frequency-dependent properties of tissue microstructure, an analysis of textural characteristics of QUS-based parametric maps can potentially provide second order statistics by quantifying the patterns of gray-level transitions. Texture-based parameters carry high-order discriminative information about patterns of neighbouring pixels in an image, and have been applied in the past on B-mode ultrasound for discriminating between benign and malignant breast tumours [65], [66]. The principle behind this tissue classification technique is that malignant tumours tend to present as heterogeneous internal echoes, whereas benign masses often demonstrate homogeneous internal echoes. Textural analysis techniques aim at extracting the tissue internal echo properties or "texture", based on the ultrasonic gray-level transitions, and hence can define differentiable characteristics in this application. However, previous studies [65], [66] have used conventional B-mode images for textural analysis, which may present undesirable variations in textural estimates due to variations in instruments settings, ultrasound beam diffraction, and attenuation effects. Such limitations can be addressed by performing texture analysis on quantitative ultrasound parametric images for which these artefacts have been compensated. This method was first applied successfully by Sadeghi-Naini *et al.* to characterize tumour cell death responses to chemotherapy *in vivo* [27] and was adapted here to investigate more subtle differences in tumour characteristics.

This study investigates, for the first time, the capacity of the textural characteristics of quantitative ultrasound parametric maps to characterize breast tumours comprehensively in terms of differentiating from normal breast tissues and in terms of their histological grade. Applying textural analysis on ultrasound spectral parametric maps rather than on B-mode images (as employed in previous techniques by other investigators) allows for instrument-independent characterization of tissues. Results here suggest that large tumours can be graded with 82% accuracy using textural features of spectral parametric maps, and a further classification accuracy of 88% can be obtained using the combination of means of the parametric maps and textural parameters. Thus, this work paves the path for the development of a systematic computer-aided breast tumour characterization methodology using non-invasive QUS techniques.

### 3.3 Methods

#### 3.3.1 Overview

The breast tissue characterization technique used here was a two-stage process involving QUS parameter estimation followed by classification. Given a tumour region of interest (ROI) in a breast ultrasound image, QUS parameters including MBF, SS, SI, SAS, ASD, AAC, and ACE were computed from its RF data. In addition to the mean of the parametric map, textural features including contrast, correlation, energy, and homogeneity were determined from the parametric map based on a gray level co-occurrence matrix (GLCM) [48].

A total of 31 parameters were considered for characterization: means from six parametric maps (MBF, SS, SI, SAS, ASD, AAC), a single-value parameter (ACE), and four texture features per parametric map ( $4 \times 6 = 24$  texture features in total). The Fisher linear classifier [67] was used to classify tissues using different QUS parameter combinations. Finally, a leave-one-out analysis was performed on the classification of grade I versus grade II-III tumours and metrics such as grade I prediction rate, grade II-III prediction rate, accuracy, and area under the receiver-operator characteristic curve were used to evaluate the classification results. The rationale for separating grade I tumours from grade II and III tumours was that patients with grade I tumours are low-risk patients compared to patients with grade II and III tumours, in terms of their management.

### 3.3.2 Ultrasound data acquisition and processing

LABC patients ( $N=57$ ,  $N_{G1}=7$ ,  $N_{GII-III}=50$ ) were recruited in this study for non-invasive tumour grading. For analysis of the QUS characteristics of breast tumours versus normal breast tissues, the first 42 patients were analyzed (as the remaining 15 patients were analyzed at a later time) and the results were reported in [24]. Patients with large tumours (3 cm or larger) were selected in this study to avoid uncertainties in tumour identification. All information regarding histopathological characteristics of the tumours, including type and grade, were determined from clinical biopsy pathology reports. Tumour size was defined as the sum of the long axis lengths of the tumour foci and was determined from diagnostic MR imaging reports. For performing supervised learning using linear discriminant analysis, tumours were histologically divided into two classes - grade I and grade II-III. This used the maximum number of available tumours in the study, since roughly 30 % of the tumours were identified by institutional pathologists as intermediate-to-high grade rather than a definitive grade II or grade III. Radiofrequency and B-mode ultrasound data were collected from the affected breast using a Sonix RP ultrasound scanner operating a 6 MHz-stimulated broadband array transducer (L14-5/38, Ultrasonix, Vancouver, Canada). RF Data were sampled at 40 MHz at a 512 line density, resulting typically in images with 6 cm width and 4-6 cm depth. Four to seven image planes of the tumour were selected at 1 cm intervals across the affected breast for analysis. In the same scan, one cross-sectional image of the normal tissue region of the breast was also obtained.

Regions-of-interest (ROIs) enclosing the central mass the tumour (approximately 90% of tumour volume) were selected across four to seven tumour cross-sections, and a cross-section of normal breast tissue was selected, under the guidance of an oncologist. The margins of the tumour were excluded in order to avoid any ambiguities in the boundary definitions. Each ROI was then segmented using a sliding window approach with 80 % overlap between adjacent windows. Each window had dimensions of 2 mm by 2 mm. The size of the window was selected to cover approximately 17 ultrasound wavelengths, larger than the minimum size (10 wavelengths) typically required to obtain reliable spectral parameters which are independent of window length [59].

In order to make the analysis method system-independent, processed US data were normalized on a sliding-window basis using reference data obtained from a tissue-mimicking phantom or a planar reflector. For linear regression analysis of the power spectrum, an in-house constructed tissue-

mimicking phantom was used, comprising of agar gel embedded with glass microspheres (modified from [68]). For SAS analysis, a plexiglas planar reflector was used as reference, as SAS estimation is sensitive to the spatial distribution of the scatterers in the reference medium, and a planar reflector has relatively simpler scattering properties compared to that of the phantom used in this study. Echo data from the polished plexiglas surface were obtained at 12 equally spaced depths from 1 to 6 cm, which covered all possible breast tumour depths. For a given tumour window, the corresponding reference window was selected by nearest neighbour interpolation. The data normalization process is discussed in more detail below.

**Table 3-1.** Patient characteristics. ER is estrogen receptor, PR is progesterone receptor, HER2 is the human epithelial growth factor receptor 2, IDC is invasive ductal carcinoma, and IMC is invasive micropapillary carcinoma. Tumour size refers to the longest diameter of the tumour.

Patient	Age	Tumour size (cm)	Grade	ER	PR	HER2	Type
1	55	8	I	-	+	+	IDC
2	53	9	II	+	+	-	IDC
3	41	4	III	+	+	+	IDC
4	65	10	II	-	-	-	IDC
5	50	5	III	+	+	+	IDC
6	33	3	I	+	+	-	IDC
7	46	8	III	-	-	-	IDC
8	41	9.7	II	+	+	+	IDC
9	48	4.9+3.2	II	+	+	-	IDC
10	36	5.8	II	+	+	-	IDC
11	40	4.4	III	-	-	-	IDC
12	62	14	III	-	-	-	IDC
13	59	6	II	-	-	-	IDC
14	65	6.7	II	+	-	-	IDC
15	38	9.2	II	+	+	-	IDC
16	53	12.7	III	-	-	-	IDC
17	48	9	II	+	+	+	IDC
18	50	13	III	-	-	-	IDC
19	49	8.9	III	-	-	+	IDC
20	46	15	III	-	-	-	IDC
21	40	3	III	-	+	+	IDC
22	56	3.2	II	-	-	+	IDC
23	49	2.8	III	-	-	+	IDC
24	47	5.2	II	+	+	-	IDC
25	52	4.1	II	+	+	-	IDC
26	44	9.9	II	+	+	+	IDC
27	38	2.2	II	+	+	-	IDC
28	58	1.9	III	-	+	-	IDC
29	36	12	I	+	+	-	IDC
30	37	N/A	III	+	+	-	IDC
31	38	8.8	III	+	+	+	IDC
32	73	7.6	III	+	+	+	IDC
33	47	12.5	II	+	+	-	IDC
34	57	7.9	III	-	-	-	IDC
35	53	4.7	II	+	+	-	IDC
36	56	2.2	II	+	+	-	IDC
37	84	4.7	II	-	-	-	IDC
38	33	10	III	+	+	+	IMC
39	39	3	III	-	-	-	IDC
40	45	6	I	+	+	+	IDC
41	60	N/A	II	+	-	+	IDC
42	45	3.8	II	+	+	-	IDC

### 3.3.3 Quantitative ultrasound analysis

All analyses of frequency-dependent backscatter were carried out within the -6 dB system transducer bandwidth, which was 3-8 MHz. The first step in the QUS analysis was computation of the ACE of the tumour, which was required for attenuation correction of the tumour power spectrum. The ACE was computed using the reference phantom method by estimating the rate of change in the spectral magnitude with depth and frequency relative to a reference medium with a known attenuation coefficient [46]. The reference medium was a well-characterized tissue-mimicking phantom with known attenuation coefficient and speed of sound. Plots of relative spectral amplitude versus depth were obtained by averaging the normalized window power spectra across laterally adjacent windows and then plotting the average amplitude at each frequency against the depth of the windows in the ROI. The ACE of the tumour was estimated by averaging the slopes of the linear fits to the amplitude versus depth data at all frequency points in the bandwidth. The newly found ACE was used to correct the tumour power spectrum for attenuation using the point attenuation compensation method [47]. Afterwards, spectral parameters, including MBF, SI, and SS were extracted from linear regression of the attenuation-corrected power spectrum within the -6 dB bandwidth, using established spectral analysis methods [17].

Using the same attenuation-corrected power spectrum, the BSC of the tumour was estimated using the reference phantom technique. Then, by MASD fitting of the Gaussian form factor to the BSC, parameters of the Gaussian form factor, ASD and AAC, were determined, as described in section 1.6 of the thesis. The SAS parameter was computed using the AR model and the SAC technique, as described in section 1.5 of the thesis.

### 3.3.4 Statistical textural analysis of quantitative ultrasound maps

In this study, a statistical texture analysis technique was applied which is based on the concept of GLCM. The GLCM represents, statistically, the angular relationship between neighbouring pixels as well as the distance between them [48]. Based on the statistical information provided by GLCM analysis, several textural features were determined including contrast (CON), correlation (COR), homogeneity (HOM), and energy (ENE), as defined in equations 1.20, 1.21, 1.22, and 1.231.211.22, respectively.

Parametric maps of MBF, SS, SI, SAS, ASD, and AAC each underwent a GLCM-based texture analysis process in order to extract four textural features. Texture properties could not be extracted from ACE, since a single value was computed from each ROI rather than computing a parametric map, as a large number of points (depths) were required to obtain accurate estimates of attenuation slope. In texture analysis, the contrast parameter represents a measure of difference between the lowest and highest intensities in a set of pixels. The energy parameter measures the frequency of occurrence of pixel pairs and quantifies its power (square of the frequency of gray-level transitions). The homogeneity parameter measures the incidence of pixel pairs of different intensities. As the frequency of pixel pairs with close intensities increases, homogeneity increases. The correlation parameter measures the intensity correlation between pixel pairs. Sixteen symmetric GLCMs were constructed for each parametric map, corresponding to four pixel-to-pixel distances (1 pixel, 2 pixels, 3 pixels, and 4 pixels) and four directions ( $0^\circ$ ,  $45^\circ$ ,  $90^\circ$ , and  $135^\circ$ ). The texture feature for each of the 16 symmetric GLCMs were computed and averaged to obtain a mean texture value. This resulted in 24 mean textural features (four features for each of the six parametric maps) which were subsequently applied, for distinguishing tumours from normal tissue, as well as for characterizing the tumours into their grade.

### 3.3.5 Tissue classification algorithm

Two levels of classifications were performed: tumour versus normal tissue, and grade I versus grade II-III tumours. For tumour versus normal tissue classification, I performed multivariate statistical analysis using the quadratic discriminant function. Combinations of ASD, AAC, and SAS were tested, since these QUS parameters provide useful physical insight about tissue microstructure and their means were found to be statistically different in tumours versus normal tissue. For classification of tumour grades, linear discriminant analysis was performed by employing sequential feature selection from the 31 QUS features (means and textures) and performing leave-one-patient-out cross-validation. Cross-validation allows one to determine how well the classification results generalize to an independent data set. The process involves dividing the data set into training and testing sets and training the classifier using the training set, then testing the classifier using the test set. The process is repeated until all data samples have been tested. The classification performances were evaluated in terms of area under the ROC curve, sensitivity, specificity, and accuracy.

## 3.4 Results

### 3.4.1 QUS analysis of tumour versus normal tissue

Relevant patient characteristics, including age, tumour size, tumour type, grade, and hormone receptor expressions (ER/PR/HER2) are summarized in Table 3-1. The patients had an average age of 49 (SD = 11) with mean tumour size (longest diameter) of 7.5 cm (SD = 4 cm). Tumours were predominantly of the invasive ductal carcinoma type (98%), with the exception of one case of invasive micropapillary carcinoma.

Each of the QUS parameters underwent paired and unpaired tests in order to determine the statistical significance of the difference between tumour and normal breast tissue ROI. A paired test determined whether mean parameter values in tumour ROIs and normal breast tissue ROIs are statistically significantly different, while maintaining the correspondence of the ROIs with the patient. On the other hand, an unpaired test determined whether mean parameter values in tumour ROIs and normal breast tissue ROIs are statistically significantly different, without accounting for ROI-patient correspondence. This evaluated the inter-patient variations of the QUS parameters. For MBF and ASD, paired/unpaired t-tests were performed between the tumour and normal tissue groups, since the data passed the normality test. For SS, SI, SAS, and AAC, Wilcoxon/Mann-Whitney (paired/unpaired) tests were performed to account for the non-normal distributions. These tests resulted in (paired, unpaired) p-values of <0.0001,0.0001\* (MBF), 0.0075,0.038\* (SS), 0.0001,0.0008\* (SI), <0.0001,0.0001\* (SAS), 0.0042,0.0279\* (ASD), and <0.0001,0.0001\* (AAC), comparing tumour to normal tissue. All six parameters demonstrated statistically significant different means ( $p < 0.05$ ) between tumour and normal tissue, both in paired and unpaired terms. In terms of class separation, however, there was a large overlap of the distributions of the QUS parameters. To improve the class separation, I performed multivariate statistical analysis using the Fisher linear discriminant (FLD) classifier employing a quadratic discriminant function. Combinations of ASD, AAC, and SAS were tested, since these QUS parameters provide useful physical insight about tissue microstructure and their means were found to be statistically different in tumours versus normal tissue. Classification performance results demonstrated sensitivity and specificity reaching as high as 88% and 91%, using the combination of (ASD, AAC, SAS). Classification results using combinations of (ASD,AAC), (ASD,SAS), (AAC,SAS), and (ASD,AAC,SAS) are summarized in Table 3-2. Listed are four performance measures including

accuracy, sensitivity, specificity, and area under the receiver operator characteristic (ROC) curve (AUC). This table summarizes the accuracy of the linear classifier (FLD) in correctly classifying tumours and normal tissues based on the mean QUS values. Here, the true labels for tumours were determined from the biopsy-proven tumour location. Normal tissue labels were determined from the B-mode images as they are rather obvious to the naked eye and the selected image plane was distant from the biopsy-proven tumour location. The ROC analysis results suggest that the combination (ASD,SAS) perform the poorest and (ASD,AAC,SAS) provides the highest accuracy, sensitivity, and specificity combination, slightly outperforming the (AAC,SAS) combination in terms of accuracy (1%). A 2-D scatter plot of the best pairwise combination, (AAC,SAS), including the quadratic curve that best divides the classes are presented in Figure 3-1.

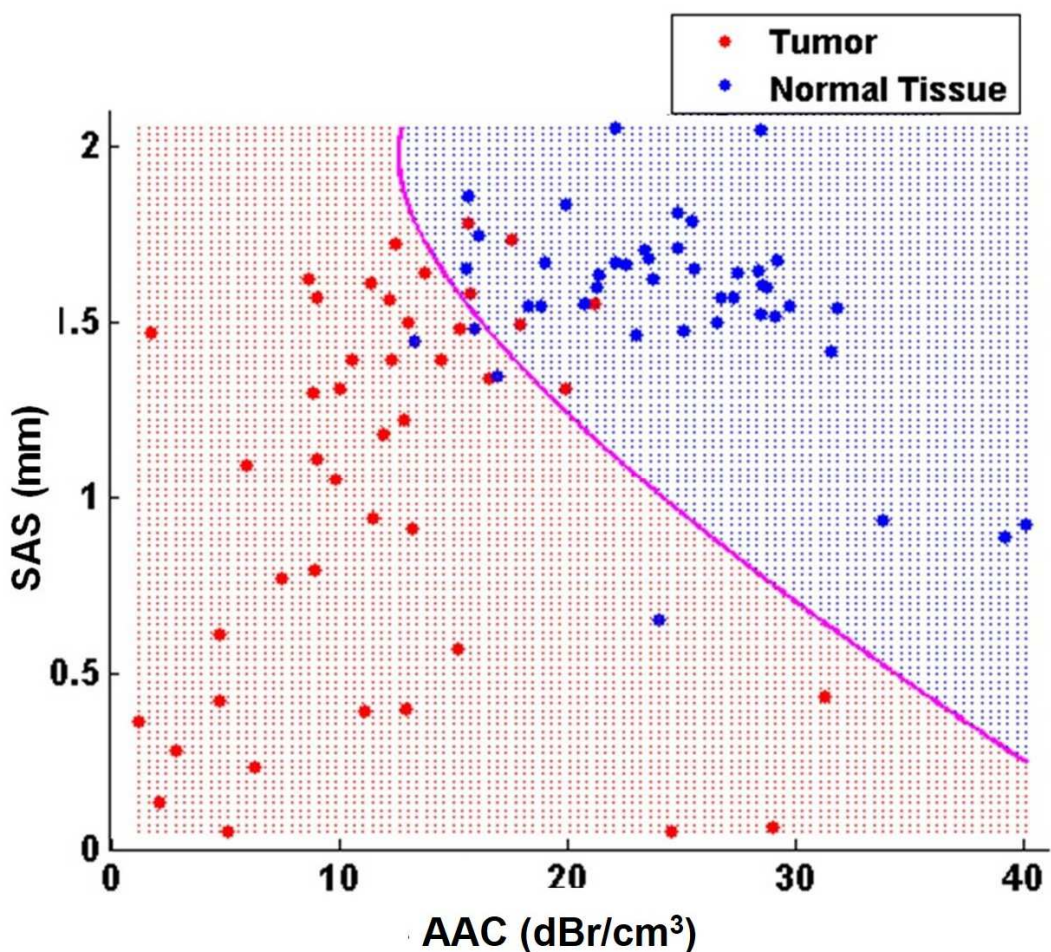


**Table 3-2.** Classifier performances using different combinations of advanced QUS parameters for tumour versus normal tissue classification - (ASD, AAC), (ASD, SAS), (AAC, SAS) and (ASD, AAC, SAS). AUC - area under the ROC curve.

	ASD, AAC	ASD, SAS	AAC, SAS	ASD,AAC,SAS
Accuracy (%)	85	73	88	89
Sensitivity (%)	88	56	86	88
Specificity (%)	81	91	91	91
AUC	0.92	0.82	0.96	0.96

### 3.4.2 QUS analysis of tumour grades

Linear discriminant analysis results obtained from three cases: using the means of all parametric maps, using the texture features of all parametric maps, and using both the means and textures of all parametric maps, are summarized in Table 3-3. GI Prediction rate was defined as the percent ratio of correctly classified GI samples to all GI samples and GII-III prediction rate was defined as the ratio of correctly classified GII-III samples to all GII-III samples. Accuracy was defined as the ratio of all correctly classified samples to all samples. All results were obtained after leave-one-out cross-validation. The results demonstrated that using only the means of the parametric maps yields lower accuracy (79%) compared to using the textural features (82%). Furthermore, combining means and textural features further improved the accuracy of the classification (86%). In all cases, lower GI prediction rate was obtained, compared to GII-III prediction rate. Table 3-4 presents the structure vector, which consists of the optimal parameters obtained from sequential feature selection from all QUS means and textures and their coefficients. The shown coefficients represent the correlation between each parameter and the obtained discriminant function. A higher absolute value indicates a higher relevance of the feature to the discrimination of the classes. It is evident from Table 3-4 that, the COR feature was the most frequently appearing feature with relatively strong contribution to the discriminant function, as it appeared for SAS ( $R^2=0.213$ ), SS ( $R^2=0.194$ ), and AAC ( $R^2=0.179$ ). Another observation was that all SAS texture features and means proved to contribute to the discrimination of tumour grades, indicating that SAS played an important role in the tumour grade classification.

Receiver-operator characteristic (ROC) curves for the three cases, obtained from the cross-validated data set, are presented in Figure 3-2. The ROC curve approaches the optimal point (upper-left corner) as better feature sets are selected (means, textures, and combined means/textures, respectively).

I selected the linear classifier for tumour grade classification due the large feature vector available. For large feature vectors, quadratic classifiers perform poorly, as indicated in the literature [69]. Based on the classification results, a hybrid parameter was determined- which represents the linear combination of a subset of QUS means and textures that provide the optimal classification accuracy (row 3 of Table 3-3). This parameter is equivalent to the output of the optimal linear discriminant function whose structure vector is provided in Table 3-4. Figure 3-3 presents a 1-dimensional scatter plot of the hybrid parameter values for all patients grouped in terms of their tumour grade. The class threshold of the linear discriminant function was defined as zero, such that any data sample with a score greater than zero was classified as a grade I tumour and any data sample with a score less than zero was classified as grade II-III tumour. The difference between the mean hybrid values (discriminant function scores) of grade I and grade II-III tumours was determined to be statistically significant ( $p < 0.05$ ).

**Figure 3-4 shows representative B-mode images, hybrid parameter images, and hematoxylin and eosin histology sections of grade I, II, and III tumours. For QUS means, QUS window values were used to compute the linear discriminant function in each window. For QUS textures, all windows were assigned a constant texture value for each texture parameter (CON, COR, ENE, HOM), since the GLCM was computed from the ROI rather than the window. Since QUS means had a lower weight in the discriminant function compared to texture parameters (even after standardization), the resulting parametric image had a relatively small standard deviation, as seen in Figure 3-4Figure 3-4.** Representative images of grade I, II, and III breast tumours. (A) B-mode images of the tumour regions, where the tumours appear as hypoechoic masses. (B) Corresponding hybrid QUS biomarker images of the tumours obtained from optimized linear combination of original QUS means and textures. A common scale bar was used to include the range for all three tumours (C) Same images as (B) but with the use of individual scale bars to show the tumour heterogeneity (D) Hematoxylin and eosin stained histopathology images of the tumours. Scale bars: 1 cm (US), 100  $\mu$ m (hist).

B. Figure 3-4B presents the hybrid image in a common scale to help realize the differences between the tumours, while Figure 3-4C presents the hybrid images in individually optimized scales, to help visualize the internal deviations. Whereas the conventional B-mode images presented all breast tumours as complex hypoechoic masses with little differences in terms of grade and difficult to visualize features, the hybrid images demonstrated a clear trend of decreasing hybrid value with

increasing tumour grade. Histology images show cancerous glands as purple stained structures, the stroma as pink stained structures, and adipose tissue as white structures. The images depict cancerous tissue with increasingly disordered clusters of cancerous glands and decreasing stromal density with increasing grade.

**Table 3-3.** Summary of classification performances for optimal parameters obtained from sequential feature selection from all means, all textures, and all means and textures. All results were obtained by leave-one-out cross-validation.

	GI prediction rate (%)	GII-III prediction rate (%)	Overall Accuracy (%)	AUC
<b>Optimal means</b>	57	82	79	0.71
<b>Optimal textures</b>	43	88	82	0.74
<b>Optimal means and textures</b>	<b>71</b>	<b>88</b>	<b>86</b>	<b>0.76</b>

**Table 3-4.** Discriminant function structure vector for optimal QUS means and textures. Coefficients represent the correlation between each parameter and the obtained discriminant function. Parameters are listed in order of decreasing absolute coefficient.

Rank	Parameter	Coefficient
1	$SAS_{ENE}$	0.236
2	$SAS_{COR}$	0.213
3	$SS_{COR}$	0.194
4	$AAC_{COR}$	0.179
5	$SI_{HOM}$	0.143
6	$AAC_{mean}$	-0.131
7	$ASD_{HOM}$	0.126
8	$SAS_{HOM}$	0.116
9	$AAC_{ENE}$	-0.098
10	$ACE_{mean}$	0.093
11	$ASD_{ENE}$	-0.086
12	$SAS_{mean}$	-0.069
13	$AAC_{HOM}$	0.061
14	$SAS_{CON}$	0.057
15	$SS_{ENE}$	0.048
16	$MBF_{ENE}$	-0.048
17	$SS_{CON}$	-0.046
18	$SI_{CON}$	-0.038

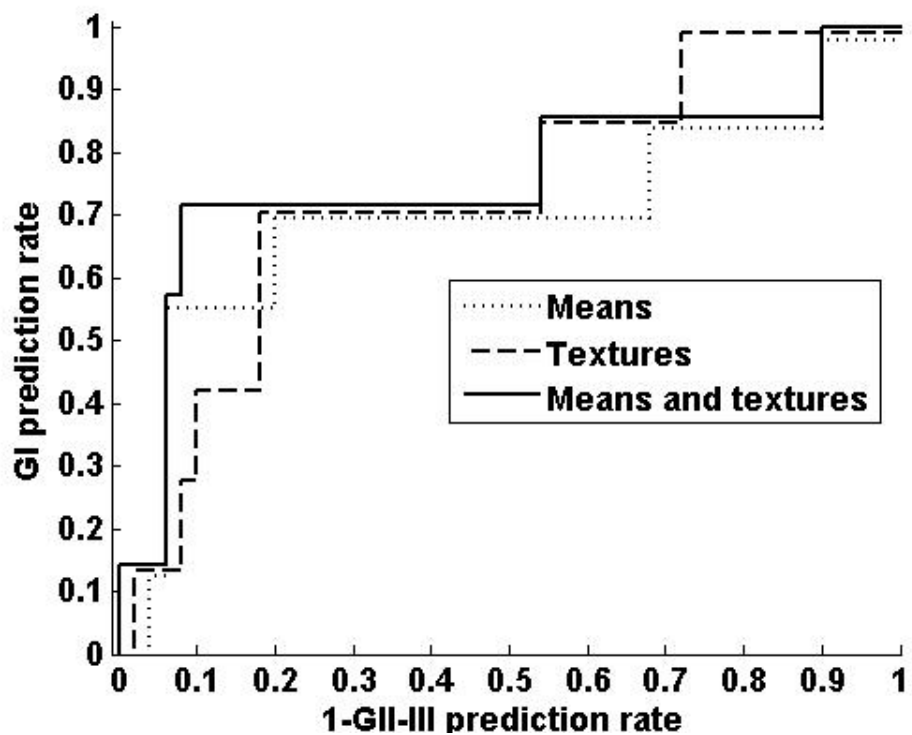


**Figure 3-2.** Receiver operator characteristics curves for the different parameter sets. Set A: means and textures of MBF, SS, SI, and SAS, plus ACE. Set B: means and textures of ASD, AAC, and SAS, plus ACE. Set C, all parameter means and textures included.

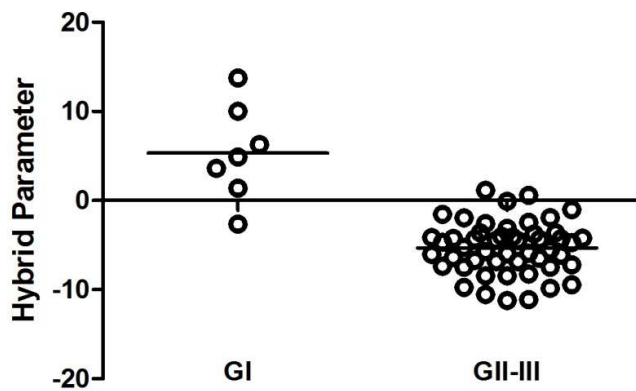


**Figure 3-3.** One-dimensional scatter plot of the hybrid QUS Biomarker versus tumour aggressiveness. Each point represents the hybrid QUS value of each patient. The horizontal lines represent the means of the groups.

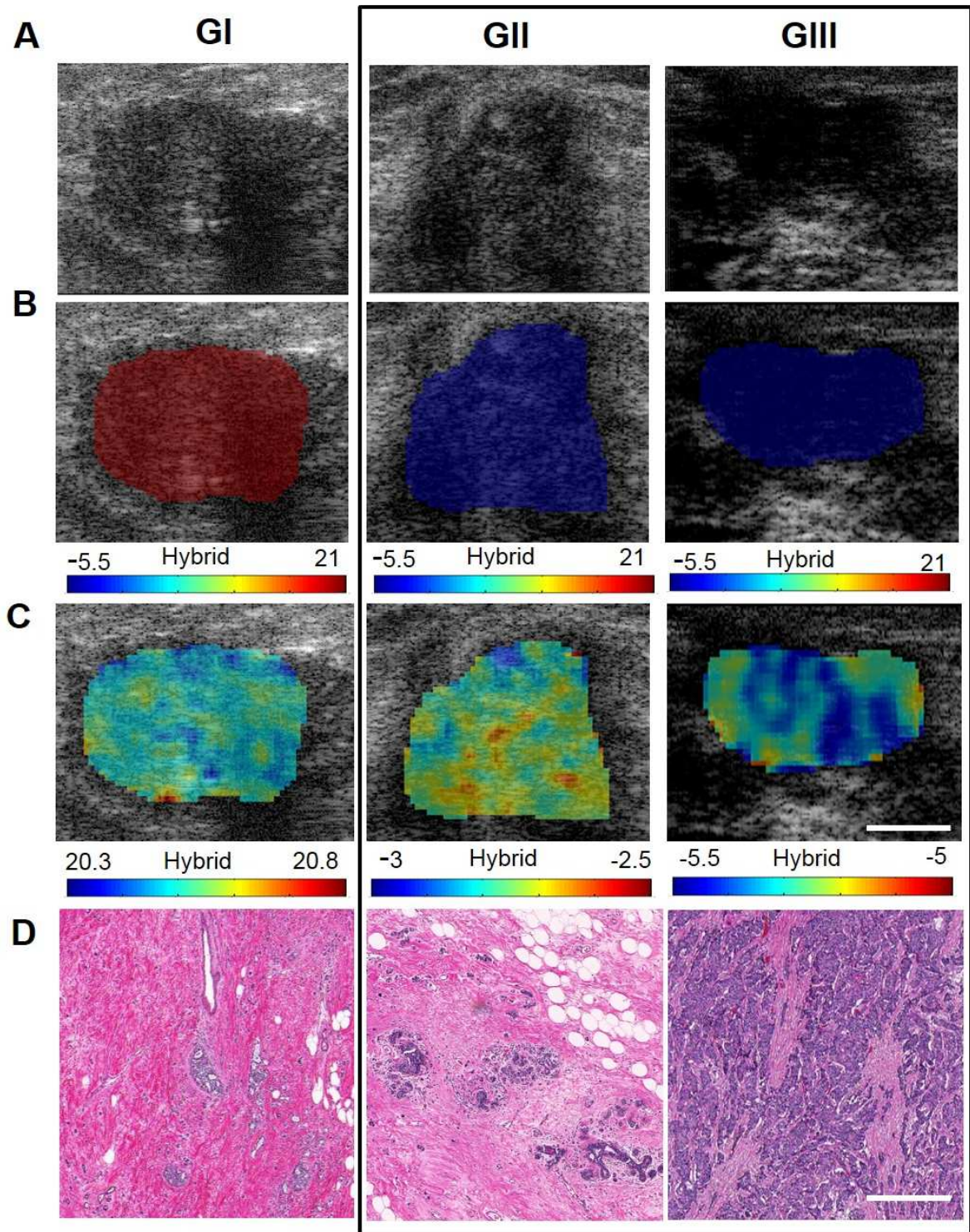


**Figure 3-4.** Representative images of grade I, II, and III breast tumours. (A) B-mode images of the tumour regions, where the tumours appear as hypoechoic masses. (B) Corresponding hybrid QUS biomarker images of the tumours obtained from optimized linear combination of original QUS means and textures. A common scale bar was used to include the range for all three tumours

- (C) Same images as (B) but with the use of individual scale bars to show the tumour heterogeneity
- (D) Hematoxylin and eosin stained histopathology images of the tumours. Scale bars: 1 cm (US), 100  $\mu$ m (hist).

### 3.5 Discussion

In summary, multiparametric analysis of advanced scattering parameters extracted from the RF ultrasound signal backscattered from breast tumours can sensitively (88%) and specifically (91%) distinguish tumours from proximal normal breast tissue. While the mean values of QUS parametric maps were all poor in differentiating tumour grades, textural analysis techniques on QUS parametric maps better discriminated between grade I and grade II-III breast tumours. After acquiring several planes of RF data from tumours of patients with LABC, features such as mean, CON, COR, ENE, and HOM were extracted from QUS parametric maps computed from tumour ROIs within the breast. An optimal feature set was selected using sequential feature selection and linear discriminant analysis was performed on the set with cross-validation, using true labels identified histopathologically from biopsy specimens. Three types of feature sets were considered: feature selection from means, textures, and the combinations of means and textures. The most accurate classification was obtained when the combination of QUS means and textures were used (86% accuracy).

Quantitative ultrasound has been investigated in the past as an aid to characterize breast tumours *in vivo* and to differentiate malignant breast tumours from benign masses [21], [42], [66], [70]. Specifically, the work of Oelze et al. [21] has demonstrated the ability to differentiate mouse mammary carcinoma from benign rat fibroadenomas using mean values of scatterer size and acoustic concentration parametric maps obtained from a 20 MHz ultrasound system. On the other hand here, the differentiation between lower grade tumours (analogous to benign fibroadenomas) and mid-to-high grade tumours (analogous to mammary carcinoma) was best seen using the textural features of AAC and ASD, giving accuracy as high as 86%. Mean values yielded less than optimal separation (79 %). Similarly, when Nasief et al. [70] investigated QUS parameters such as scatterer size, attenuation, and heterogeneity index to differentiate clinically benign breast tumours from malignant ones, only subtle differences could be found, since only mean values were considered. The parametric images here (Figure 3-4. Representative images of grade I, II, and III breast tumours. (A) B-mode images of the tumour regions, where the tumours appear as

hypoechoic masses. (B) Corresponding hybrid QUS biomarker images of the tumours obtained from optimized linear combination of original QUS means and textures. A common scale bar was used to include the range for all three tumours (C) Same images as (B) but with the use of individual scale bars to show the tumour heterogeneity (D) Hematoxylin and eosin stained histopathology images of the tumours. Scale bars: 1 cm (US), 100  $\mu$ m (hist).

), however, suggested clear distinctions between tumours of different grades when textures of QUS parameters were included.

In the tumour versus normal tissue study, the difference in the classification performance obtained using SAS, AAC and SAS, AAC, ASD was not assessed in a statistical sense. The 1% increase in accuracy may not be statistically significant. In the future, one could perform bootstrapping in order to obtain a number of classification accuracies for each feature set, and perform a significance test between the two-feature QUS and three-feature QUS models. Nevertheless, the obtained accuracies with the two-feature and three-feature QUS models were sufficiently high to warrant clinical application of our method as an aid for radiologists in tumour identification in breast ultrasound images.

Previous studies on the application of textural analysis techniques for ultrasound-based breast tissue characterization have been limited to those aimed to differentiate predominantly between benign and malignant masses using plain B-mode images [66]. Such studies have in the past raised concerns regarding reproducibility, mainly due to instrument dependency and lack of parameter normalization [65], [66]. Consequently, the results obtained in those studies could vary from one imaging system to another, since the GLCMs were computed from B-mode images. Here, a GLCM computed from a quantitative ultrasound parametric map obtained from normalized power spectra (which are phantom-calibrated) would be in principle instrument independent. In this study, texture analysis of the QUS parametric maps of different grades of breast tumours demonstrated a strong separation when the combination of texture features (CON, COR, ENE, HOM) of the parametric maps were used (82% accuracy). A further improvement in classification was achieved when the means of parametric maps were combined with the textures (86% accuracy).

It is acknowledged that relatively lower G1 prediction rates were obtained compared to GII-III prediction rates. This is likely due to the presence of imbalanced data, where there are many more

grade II-III cases than grade I cases, producing a bias in the classification results. Compensation for imbalanced datasets is an active area of research and requires thorough investigation in a separate study. Nevertheless a leave-one-out analysis here was able to fairly accurately identify grade I tumours compared to grade II-III tumours which are often managed differently in terms of clinical care.

As previously mentioned, acoustic concentration is the product of scatterer number density and acoustic impedance difference between the scatterer and the background, and acoustic impedance is the product of sound speed and density. Thus, the fact that parameters related to the scatterer spacing and acoustic concentration including SAS, AAC, MBF, and SI formed the major portion of the discriminant function (Table 3-4) compared to parameters related to the scatterer size (i.e. SS and ASD) suggests that the spatial organization and material properties of the tumour microstructure play a more important role than its size in the discrimination of tumour histological grades. This was not surprising since the breast tumour is a complex tissue containing blood vessels, adipose tissue, and stroma, in addition to cancerous glands. Thus, scatterer size may not refer to the size of glands alone, but to a mixture of structures. The results here stimulate investigation into a better scattering model, for example, one which accounts for dense packing of cells in tumours. The structure factor model has been suggested recently as a scattering model which provides theoretical solution for the BSC accounting for high scatterer concentrations reflected in tumour tissues [71]. The search of a better attenuation estimation algorithm (i.e. one that accounts for tissue heterogeneity) is also warranted.

In summary, breast tumour grading is an important part of breast cancer diagnosis and provides valuable information for treatment planning. In this light, non-invasive methods such as texture-based QUS analysis can provide beneficial diagnostic information which can be applied before and during the course of treatment. This study demonstrated a high potential for textural characteristics of QUS parametric maps to be used in the diagnosis and grading of breast tumours. The best tissue classification could be achieved when the combination of mean and textural properties of MBF, SS, SI, SAS, ASD, and AAC parametric maps were used. This work provides a framework for future clinical studies in which the proposed classification scheme is evaluated on larger cohorts of patients in order to further assess its capabilities for an accurate breast tumour diagnosis and grading, non-invasively.

## 4 Quantitative ultrasound assessment of breast tumour response to chemotherapy

## 4.1 Overview

**Purpose:** This study demonstrated the ability of quantitative ultrasound parameters in providing an early prediction of tumour response to neoadjuvant chemotherapy in patients with locally advanced breast cancer.

**Methods:** Ultrasound data consisting of raw RF data were collected from 58 locally advanced breast cancer patients prior to chemotherapy treatment and at 4 times during their treatment (weeks 0, 1, 4, 8, and prior to surgery) using 6-MHz ultrasound. Quantitative ultrasound parameters including linear regression spectral parameters (midband fit, spectral slope, 0-MHz intercept), scatterer spacing, attenuation coefficient estimate, and backscatter coefficient parameters (average scatterer diameter and average acoustic concentration) were determined. Ultrasound data were compared with the ultimate clinical and pathological response of the patient's tumour to treatment and patient recurrence-free survival.

**Results:** Midband fit, 0-MHz intercept, and attenuation coefficient estimate parameters increased statistically significantly in patients with treatment-responding tumours compared to nonresponding patients as early as 1 week after the start of the treatment. In contrast, tumour size change was not found to be significantly different in responders and non-responders. Discriminant analysis using the K nearest neighbour classifier demonstrated that the best classification performance could be achieved using the combination of midband fit, spectral slope, and scatterer spacing, with an accuracy of  $60 \pm 10\%$  at week 1,  $77 \pm 8\%$  at week 4 and  $75 \pm 6\%$  at week 8. Furthermore, when the QUS measurements at each time (week) were combined with pre-treatment (week 0) QUS information, the classification accuracies improved ( $70 \pm 9\%$  at week 1,  $80 \pm 5\%$  at week 4, and  $81 \pm 6\%$  at week 8). Finally, the QUS classification model demonstrated a significant difference in survival rates of responding and nonresponding patients at weeks 1 and 4 ( $p=0.035$ , and  $0.027$ , respectively).

**Conclusion:** This study demonstrates for the first time, using new parameters tested on a relatively large patient cohort and leave-one-out classifier evaluation, that a hybrid QUS biomarker including attenuation-corrected midband fit, spectral slope, and scatterer spacing, can detect the response of LABC tumours to neoadjuvant chemotherapy with 80% accuracy as early as after 4 weeks. The findings of this study also incorporated novel pre-treatment ultrasonic scattering properties of a tumour improving results. This work demonstrates the potential of quantitative ultrasound and

machine learning methods for predicting the response of breast tumours to chemotherapy early and guiding personalized medicine with regards to the treatment planning of refractory patients.

## 4.2 Introduction

Conventional methods of clinical tumour response assessment involve tracking changes in tumour size, using the guidelines provided by RECIST [6]. Such measurements are ascertained using anatomical-based imaging modalities such as X-ray imaging, magnetic resonance imaging (MRI), or conventional diagnostic ultrasound. However, these size-based metrics typically provide late indications of response as measurable changes in tumour size do not occur until several weeks to months after the initiation of the chemotherapy treatment, despite positive response [7]. Currently no routine clinical imaging is carried out to assess tumour size or response during breast chemotherapy administration in a neoadjuvant setting. This study determined the ability of quantitative ultrasound parameters extracted from raw (radiofrequency) tumour-based ultrasound data in predicting patient-based tumour responses early in the course of neoadjuvant chemotherapy.

Tumour shrinkage is known to be the late cumulative effect of cell death induced by anti-cancer therapy. Previous studies which have used early biomarkers obtained from tumour biopsy samples have demonstrated that increased tumour apoptosis occurring early in the course of therapy was associated with good clinical response, and consequently an improved patient survival [8]. Thus, the introduction of a non-invasive functional imaging biomarker that can be used to monitor the early response of a tumour to anticancer therapy can potentially help facilitate personalized treatment for cancer patients.

Ultrasound, commonly used clinically for screening, diagnosis, and image-guided procedures, due to its low cost, quick imaging time, high resolution, and ionizing radiation-free nature, has recently been explored by investigators as a potential imaging modality for tumour response monitoring [28]. This was achieved in that study using QUS, which used a quantitative analysis of the frequency content of the RF signals backscattered from breast tumours in patients undergoing chemotherapy. According to the theoretical formulation of ultrasound scattering, the tissue power spectrum is affected by parameters such as the size and number density of the constituent

scatterers. Thus, based on inherent differences in the microstructures of different tissues, parameters obtained from the tissue power spectrum, including MBF, SI, and SS, have enabled the characterization of abnormalities of different tissues such as those in breast, prostate, liver, eye, myocardium, and lymph nodes [14], [16], [18]–[20], [22], [24]. These parameters of interest are estimated from a linear regression analysis of the tissue power spectrum within the usable bandwidth (usually corresponding to  $-6$  dB range), representing the slope (SS) and intercept (SI) of the line, as well as the value of the line at the center of the frequency bandwidth (MBF). Alternatively, some studies have found higher-order model derived parameters such ASD and AAC to be useful in studying tissues, including differentiating mouse models of breast cancer from benign breast masses, grading clinical breast cancer, and detecting cancerous human lymph nodes [16], [21], [24]. In regards to applications in treatment monitoring, Sadeghi-Naini *et al.* [28] posited that at a clinically relevant frequency range ( $<10$  MHz), spectral parameters such as MBF, SI, and SS are sensitive to changes in tumour microstructure which occur as a result therapeutic effects, and therefore can correlate to early signatures of tumour response. Using linear discriminant analysis, they demonstrated that the combination of MBF and SI parameters provided 100% sensitivity and 83% specificity in the detection of response of tumours to chemotherapy. More recently, Tadayyon *et al.* [72] demonstrated that estimating the acoustic attenuation of the patient's tumour and correcting the power spectra accordingly, not previously done [28], increased the sensitivity of MBF to response detection by 12% and specificity by 17%. Moreover, the performance measures reported by Sadeghi-Naini *et al.* were obtained without cross-validation and due to the small sample size ( $N = 25$ ), clinical feasibility was limited. Here, I propose a new approach for QUS prediction of breast tumour response to neoadjuvant chemotherapy tested on a relatively large database of breast US data ( $N = 58$ ), incorporating attenuation estimation and correction of the power spectra. The study here performed discriminant analysis using a more advanced classifier - k nearest neighbour (KNN) classifier. The KNN classification was performed using leave-one-patient-out cross-validation, not performed in previous studies. In addition to classical spectral parameters (MBF, SS, and SI) previously investigated, I have also investigated the utility of advanced BSC parameters (ASD and AAC), SAS, as well as ACE in predicting the therapeutic response of breast tumours.

## 4.3 Methods

### 4.3.1 Ultrasound data acquisition and processing

This prospective study was reviewed and approved by the institution's research ethics board. After obtaining informed consent, ultrasound RF data were collected from the affected breast of patients (N=58) with LABC prior to neoadjuvant chemotherapy treatment initiation and at four times during the course of the treatment - week 1, week 4, week 8, and prior to surgery (mastectomy/lumpectomy). Patients recently diagnosed with locally advanced invasive breast cancer within one week, including invasive ductal carcinoma, invasive lobular carcinoma, and other forms of invasive cancer, including all grades, were referred from the diagnostic clinic to our study. This included patients with tumours larger than 5 cm and/or tumours with locoregional lymph node, skin, and chest wall involvement as per guidelines reported in [73]. All clinical and ultrasound data obtained for this study was dated back to patients treated between January 2009 and August 2013. Treatment regimens varied from 5-fluorouracil, epirubicin and cyclophosphamide followed by docetaxol (FEC-D), to Adriamycin followed by paclitaxel (AC-T), to taxol followed by herceptin varying from weekly to tri-weekly cycles. Individual patient treatment regimens are provided in Table A.1 of Appendix.

Breast ultrasound data were collected by an experienced breast sonographer with 10 years of experience using a clinical scanner (Sonix RP, Ultrasonix, Vancouver, Canada) employing a 6 MHz linear array transducer (L14-5-60), sampling at a rate of 40 MHz, with the focus set at the midline of the tumour and maximum depth set to 4-6 cm, depending on tumour size and location. Standard B-mode imaging was used for anatomical navigation and acquisition location was determined based on the tumour location reported in biopsy findings. Approximately 3-5 (mean of 4) image planes were acquired from the tumour, depending on the tumour size. Rectangular regions of interest (ROI) were selected in the center of the tumour, covering approximately 90% of the tumour, within each image plane and segmented into smaller blocks, called RF blocks. The data used for quantitative ultrasound spectral analysis were the RF blocks, consisting of 20 scan lines each 10 wavelengths long. This approximately corresponded to a  $2 \text{ mm} \times 2 \text{ mm}$  block (assuming a speed of sound of 1540 m/s). Each RF block overlapped its neighbour by 80% in both axial and lateral directions. Normalized power spectrum was computed for each RF block using a phantom reference, and a parametric image was computed over each tumour ROI for each QUS parameter.

The QUS parameters investigated were MBF, SS, SI, SAS, ACE, ASD, and AAC. Depth-dependent spectral signal corrections were performed using a homogeneous tissue-mimicking phantom prior to parameter estimation, thus eliminating effects of tumour depth and size. In addition to acquiring ultrasound data, tumour size reported by oncologists by physical examination in the follow-up visits was also examined. Size reports were corroborated by ultrasound imaging results but clinical physical examination documentation was used for tumour size measures.

#### 4.3.2 Quantitative ultrasound data analysis

All spectral analyses were carried out using the data from the -6 dB system transducer bandwidth, which was 3-8 MHz. The first step in the QUS analysis was computation of the ACE of the tumour, which was used for attenuation correction of the tumour power spectrum. The ACE was computed using the reference phantom method by estimating the rate of change in the spectral magnitude with depth and frequency relative to a reference medium with a known attenuation coefficient [46]. The reference medium was a well-characterized tissue-mimicking phantom with known attenuation coefficient and speed of sound. Plots of relative spectral amplitude versus depth were obtained by averaging the normalized block power spectra across laterally adjacent blocks and then plotting the average amplitude at each frequency against the depth of the blocks in the ROI. The mean ACE of the tumour was estimated by averaging the slopes of the linear fits to the amplitude versus depth data at all frequency points in the bandwidth. The newly found ACE was used to correct the tumour power spectrum for attenuation using the point attenuation compensation method [47]. Afterwards, spectral parameters, including MBF, SI, and SS were determined from linear regression of the attenuation-corrected power spectrum within the usable (-6 dB) bandwidth. SI and SS are the intercept and slope parameters of the line of best fit, and MBF is the magnitude of the spectral fit at the center of the frequency bandwidth.

Using the same attenuation-corrected power spectrum, the BSC of the tumour was estimated using the reference phantom technique [74]. Then, by least-squares fitting of the Gaussian form factor to the BSC, arguments of the Gaussian form factor, ASD and AAC, corresponding to the maximum coefficient of determination,  $R^2$ , were determined. Details about scatterer size estimation can be found elsewhere [34].

Whereas spectral linear regression and BSC models are based on incoherent scattering, cepstral analysis techniques permit coherent scattering properties of tissues to be derived and coherent structures to be identified [75]. For cepstral analysis, the power spectrum of the tumour was determined by modeling the tumour echo signal as an autoregressive signal and using Burg's algorithm to estimate its power spectrum [76]. The power spectrum was then normalized to that of a planar reflector. By computing the autocorrelation of the normalized power spectrum, the SAS parameter was determined from the frequency at which the peak occurred in the autocorrelation. The implementation of this technique followed the technique used by Tadayyon *et al.* to estimate SAS in breast tumours and normal tissues, which demonstrated a separation between breast tumours of different histological grades [24].

After computing all 7 QUS features for all patients, discriminant analysis was performed using the KNN classifier and using all possible combinations of QUS features. The KNN classifier determines the class of a point in the feature space based on the class which forms the majority of the points neighbouring the point of interest and based on the distance between those points and the point of interest [77].

#### 4.3.3 Classification and statistical analyses

All QUS results were compared with the clinical standard response of each patient, determined based on the RECIST guideline. This was determined at the end of their several-month treatment by measuring the reduction in gross tumour size based on dynamic contrast enhanced magnetic resonance images (DCE-MRI) cross-verified with whole-mount breast histopathology obtained post-operatively. Since the focus of this study was a binary classification of response, the standard four categories of response defined in the RECIST guideline were merged into two categories by grouping complete and partial responses into “response” and grouping stable and progressive disease responses into “nonresponse”. A recent study demonstrated that residual tumour cellularity is an important prognostic factor in breast cancer neoadjuvant treatment, which should be taken into account in conjunction with the RECIST metric of bulk tumour shrinkage (BTS) [78]. Accordingly in this study, a patient was deemed to be a clinical responder if the sum of the lengths of the tumour foci was reduced by more than 30% or if in the non-mass enhancing

area, the pathologically determined residual tumour cellularity was low. A patient was deemed to be a clinical non-responder if the sum of the lengths of their tumour foci was reduced by less than 30% or the residual tumour cellularity remained high.

The mean changes in each QUS parameter were compared between the clinical responder and non-responder groups at each time. Initially, a Shapiro-Wilk normality test was used to test each parametric data set for normality. Since all data sets passed the normality test, a student's unpaired t-test (right-tailed,  $\alpha=0.05$ ) was used to test for statistical significance of the difference between group means. In order to determine the clinical feasibility of using QUS as a cancer therapy monitoring system, multi-feature response classification was performed using the KNN algorithm based on Euclidean distances. Rather than the absolute values, the changes in the QUS parameters relative to their pre-treatment value (week 0) were used as classification features, which are denoted here by the prefix  $\Delta$  (i.e.  $\Delta\text{MBF}$ ). This baseline normalization was necessary in order to minimize inter-patient variability of each parameter. The imbalance in the data set was compensated for by randomly sampling (with replacement) from the responder group so as to have equal number of responders and non-responders ( $N=16$ ). All patients in the non-responder group were used for training and testing the classifier ( $N=16$ ). Classification was performed 10 times (10 different responder group samples) with leave-one-patient-out evaluation. Since the number of QUS features was small ( $n=7$ ), an exhaustive search method was used for obtaining the optimal subset of features. During the exhaustive search a leave-one-patient-out cross-validation was performed to obtain classification results. This accounted for the classifier's generalization ability and inter-subject variability, as suggested in the literature [79]. The accuracy was used as the objective function to maximize. The metrics used for measuring classification performance were sensitivity, specificity, and accuracy.

## 4.4 Results

Patient characteristics, including age, initial tumour size, tumour subtypes, and bulk tumour shrinkage for responders and non-responders are summarized in Table 4-1. All patients were females aged between 29 and 67 years with a mean age of 50 years. Tumour size ranged from 2 to 13 cm, with a mean size of 6.3 cm. The tumours were mainly of the invasive ductal carcinoma

type not otherwise specified (90% of cases). The remaining 10% of cases were comprised of invasive lobular carcinoma (5%) and other types of breast cancer (5%). The ultimate clinical response rate to chemotherapy in the sample population was 72% and responders demonstrated a tumour shrinkage of  $68 \pm 47\%$  whereas the non-responders demonstrated mean bulk shrinkage of  $-16 \pm 57\%$ . Bulk tumour shrinkage was defined as the relative reduction in the sum of tumour diameters from pre-treatment to pre-operation. Size measurements were ascertained using breast DCE-MRI obtained at these two times. Detailed individual patient characteristics and responses are provided in Tables A.1 and A.2 of Appendix.

Representative images of a responding breast tumour and a nonresponding breast tumour before treatment start and 4 weeks after treatment start (1-2 cycles of chemotherapy) are presented in Figure 4-1 and Figure 4-2. For each tumour, B-mode images, MBF images overlaid on the B-modes, power spectra before and 4 weeks after the start of treatment, and magnified hematoxylin and eosin (H&E) stained histology sections of whole-mount breast specimens obtained post-surgery (mastectomy/lumpectomy) are shown. These data were selected for illustration as MBF was a parameter which demonstrated statistically significant changes at early weeks (1 and 4). Whereas B-mode images showed no appreciable changes in the tumour 4 weeks into treatment, a marked increase in MBF could be observed in the responding tumour region as a result of 4 weeks of chemotherapy treatment (1-2 cycles). The nonresponding tumour, on the other hand, demonstrated no change or decrease in MBF. The before/after superimposed power spectra demonstrate the same concept graphically, where MBF is marked by a circle in the middle of the regression line (Figure 4-1 and Figure 4-2, C left). There is a small offset between the MBF values in the MBF images and MBF values in the power spectra. This is due to the fact that the shown power spectrum plots were obtained by averaging the power spectra from all RF blocks within the ROI, whereas the MBF values in the MBF images were obtained from representative individual power spectra of individual RF blocks within the ROI. The histology image of the responding tumour indicates a stroma-filled tissue (pink staining) with small isolated patches of glands (purple staining), demonstrating therapeutic effects. On the other hand, the histology of the nonresponding tumour shows a gland-dominated tumour with low stromal collagen density, indicating little to no therapeutic effect.

Figure 4-3 compares QUS parameters and the RECIST-based tumour size reduction for tracking changes in the tumour during chemotherapy. Average QUS data obtained from responding and nonresponding groups are plotted versus treatment time in Figure 4-3A-G. Patients were grouped based on their ultimate clinical/pathological responses. The vertical axes represent changes in QUS parameters relative to week 0 (pre-treatment). Parameters related to the intensity of the frequency-dependent backscatter (i.e.  $\Delta$ MBF,  $\Delta$ SI,  $\Delta$ AAC) demonstrated, on average, an increase with treatment time for responders. Based on unpaired t-test comparison of responder and non-responder groups, two-tailed with 95 % confidence, this increase was statistically significant at weeks 1, 4, and 8 for  $\Delta$ MBF ( $p = 0.042, <0.005, <0.005$ , respectively), and at weeks 1, 4, and 8 for  $\Delta$ SI ( $p = 0.034, 0.010, <0.005$ , respectively). Patients in the responding group demonstrated a greater increase in  $\Delta$ ACE compared to non-responders, which were statistically significant at weeks 1 and 4 ( $p <0.005$  and 0.042, respectively). On the other hand,  $\Delta$ SS,  $\Delta$ ASD, and  $\Delta$ SAS values did not show any significant changes between responders and non-responders at any time during the treatment. As expected, the mean tumour size reduction shown in Figure 4-3H was not significantly different in responders versus non-responders at any time ( $p = 0.89, 53$ , and 0.42 at week 1, 4, and 8, respectively) except at the end of the several-month treatment ( $p = 0.0011$  at pre-op). Whereas a 30% mean size reduction occurred in responders at week 4 (Figure 4-3H), non-responders also had a mean reduction of almost 30% at week 4, and the difference between the groups was not statistically significant. After week 4, whereas responding tumours continued shrinking, nonresponding tumours regrew to 20 % larger than their original size between week 8 and pre-op, which had approximately an 8 to 10 week gap.

In order to compare the effectiveness of different QUS parameters in differentiating responding tumours from nonresponding ones, the KNN algorithm was run for each QUS parameter separately and classification accuracy was computed. Table 4-2 summarizes the performance of individual QUS parameters in predicting response in terms of classification accuracy and statistical significance ( $p$ -value) for weeks 1, 4, and 8. The classification results are based on a 2-neighbour search area and using the Euclidian distance metric, which provided the optimal classification. The results demonstrated that the MBF parameter was most effective in response detection at all weeks

(accuracy =  $61 \pm 8\%$ ,  $65 \pm 5\%$ , and  $85 \pm 5\%$ , for weeks 1, 4, and 8, respectively), followed by SI (accuracy =  $55 \pm 8\%$ ,  $65 \pm 11\%$ ,  $74 \pm 6\%$ , respectively). Overall, performances improved at week 8 compared to those of weeks 4 and 1.

Table 4-3 presents the RECIST classification results versus KNN classification results using the best combination of QUS parameters obtained through exhaustive search feature selection. Sensitivity was defined as the ratio of the number of true responders to total number of responders (expressed as a percentage). Specificity was defined as the ratio of the number of true non-responders to the total number of non-responders in percentage. Accuracy was determined as the percentage of total number of correctly classified patients to the total number of patients. The first row presents the RECIST-based response classification, which was performed by classifying each patient based on 30 % reduction at each follow-up visit and comparing the prediction with their “true” response, assumed to be the ultimate clinical/pathological response. The second row presents the QUS results obtained when the pre-treatment QUS data was excluded from the discriminant analysis, whereas the third row presents the results when the pre-treatment data was included in the discriminant analysis. The fourth row presents the p-values of the significance of the difference between the accuracies of the second and third rows. An asterisk indicates a significant difference. Leave-one-patient-out cross-validation was performed on the KNN classifier to obtain the overall sensitivity, specificity, and accuracy values on all 58 tests (58 patients). All possible combinations of the 7 QUS parameters ( $\Delta MBF$ ,  $\Delta SS$ ,  $\Delta SI$ ,  $\Delta SAS$ ,  $\Delta ACE$ ,  $\Delta ASD$ ,  $\Delta AAC$ ) were investigated for feature selection. The best combination of parameters when pre-treatment information was excluded, was determined to be [ $\Delta MBF$   $\Delta SS$   $\Delta SAS$ ] (accuracy =  $60 \pm 10\%$ ,  $77 \pm 8\%$ ,  $75 \pm 6\%$ , at weeks 1, 4, 8, respectively). Combinations of 4 or more parameters have not been reported since no improvement was observed beyond 3 parameters. A separate feature selection was performed for the case when the pre-treatment values were included. As expected, the RECIST method showed poor discrimination between responders and non-responders at all times during the treatment (accuracies of 30%, 52%, and 68% at weeks 1, 4, and 8, respectively). In contrast, the QUS method achieved the best performance using the set [ $MBF_{wk0}$   $\Delta MBF_{wk4}$   $SS_{wk0}$   $\Delta SS_{wk4}$   $SAS_{wk0}$   $\Delta SAS_{wk4}$ ] with accuracies of  $70 \pm 9\%$ ,  $80 \pm 5\%$ , and  $81 \pm 6\%$  at weeks 1, 4, and 8, respectively. The inclusion of pre-treatment information demonstrated a

statistically significant up to 10 % improvement in the accuracies at weeks 1 and 8 (p-value = 0.03, 0.04, respectively).

In order to compare the predictions of QUS and histopathology on the recurrence free survival (RFS) of the patients, Kaplan-Meier survival analysis was performed and the results are presented in Figure 4-4. The median follow-up time was 25 months. The RFS curves were divided into responder and non-responder groups. A log-rank test was performed to compare the RFS rates between the responders and non-responders using the method described in [80]. The RFS curves obtained from QUS biomarkers demonstrated statistically significant differences between the response groups at weeks 1 and 4 (log-rank p-value = 0.035, 0.027, respectively) as did the RFS curves obtained from histopathology information (log-rank p-value = 0.0002). However, RFS curves obtained from QUS biomarkers at week 8 did not show significant difference between the response groups (log-rank p-value = 0.26).

**Table 4-1.** Summary of patient characteristics. IDC = invasive ductal carcinoma, ILC = Invasive lobular carcinoma, BTS = bulk tumour shrinkage (percent change in tumour size).

<b>Characteristic</b>	<b>Total (N=58)</b>	
	<b>No.</b>	<b>%</b>
<b>Age (y)</b>	49 ± 10	
<b>Tumour subtype</b>		
IDC	52	90
ILC	3	5
Other	3	5
<b>Responders</b>	42	72
BTS (%)	68 ± 47	
<b>Non-responders</b>	16	28
BTS (%)	-16 ± 57	

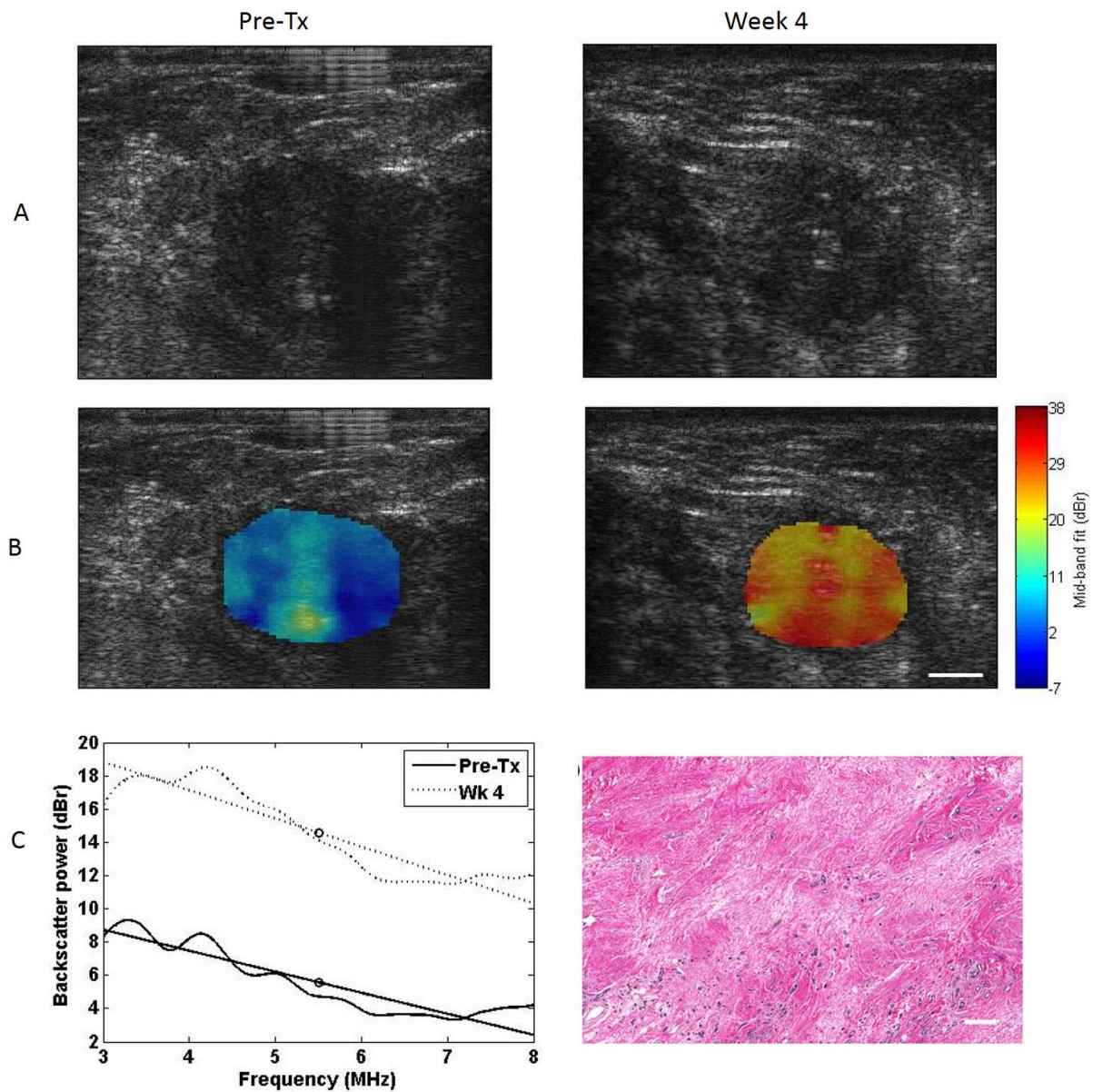


Figure 4-1. Representative B-mode images (A), MBF images (B), power spectra (C left) before and 4 weeks after the start of chemotherapy treatment and hematoxylin and eosin histology histology images (C right) of an example responding breast tumour. Data in the left column represent pre-treatment data, obtained prior to treatment initiation, and data in the right column represent week 4 data. US scale bar represents 1 cm, histology scale bar represents 100 µm.

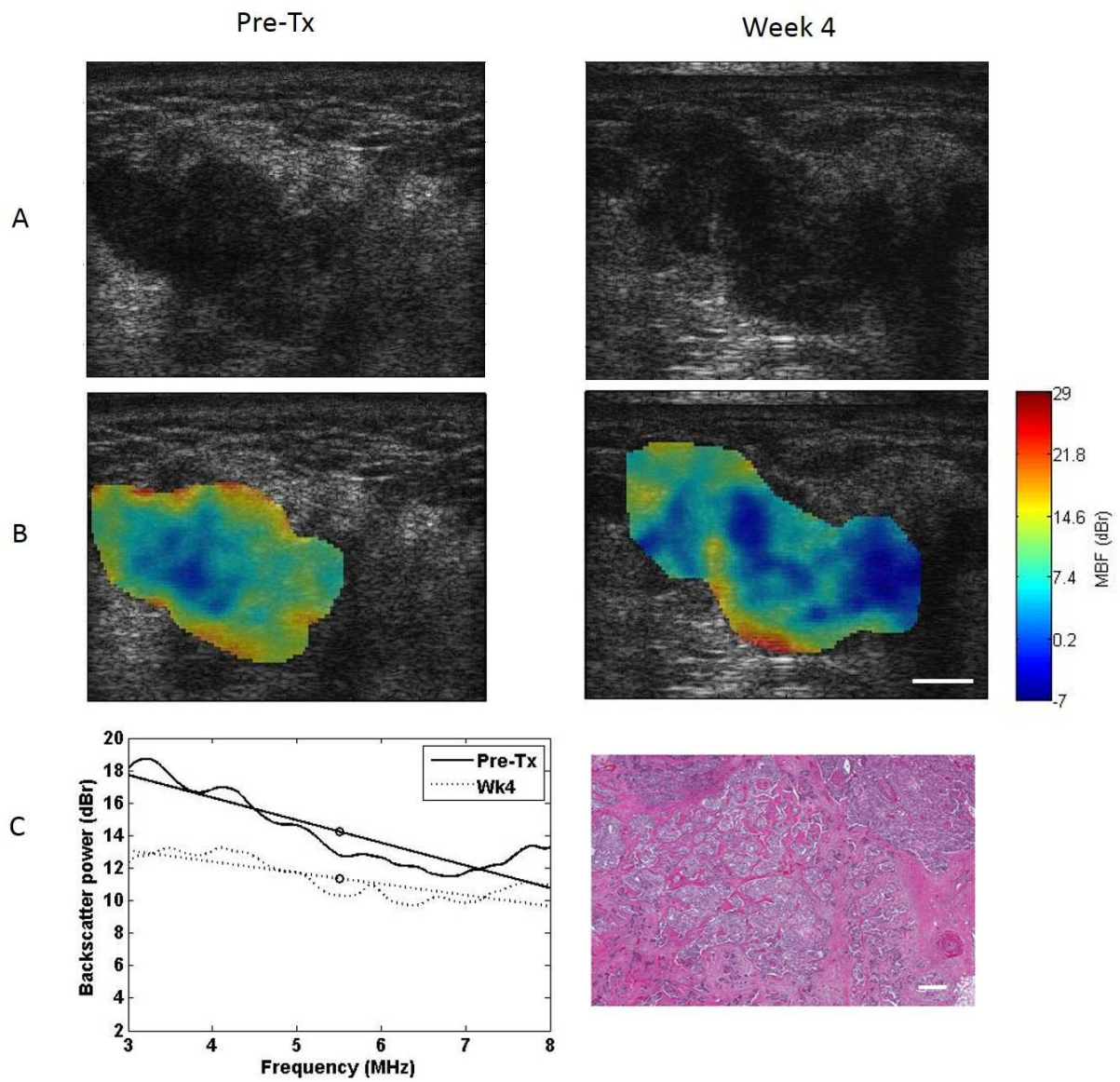
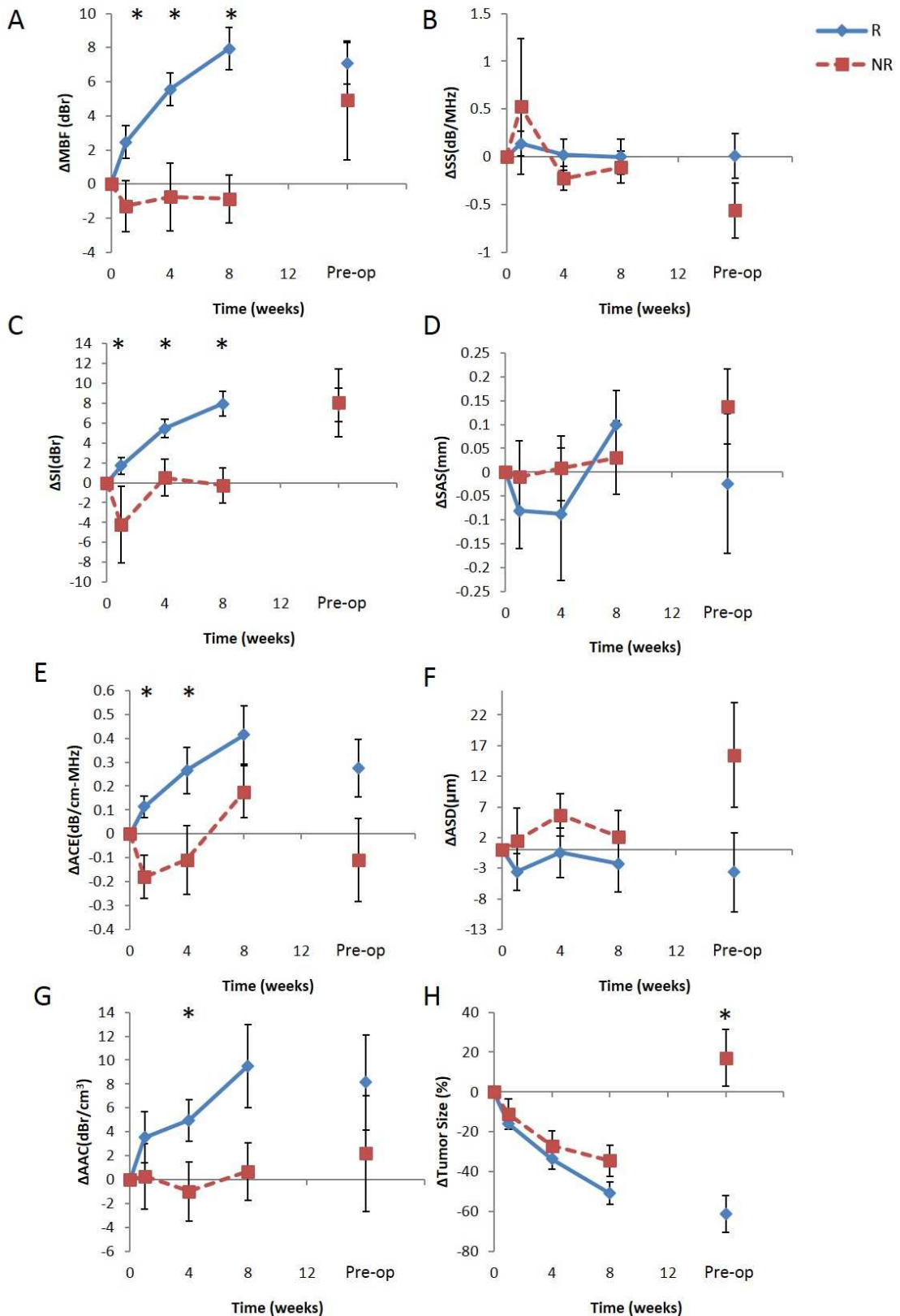


Figure 4-2. Representative B-mode images (A), MBF images (B), power spectra (C left) before and 4 weeks after the start of chemotherapy treatment and hematoxylin and eosin histology histology images (C right) of an example nonresponding breast tumour. Data in the left column represent pre-treatment data, obtained prior to treatment initiation, and data in the right column represent week 4 data. US scale bar represents 1 cm, histology scale bar represents 100  $\mu$ m.



**Figure 4-3.** Comparison between QUS parameters (A-G) and the RECIST-based tumour size reduction (H) for tracking patient tumours during chemotherapy. QUS and RECIST values were averaged over responder (blue diamond) and non-responder (red square) groups, and plotted over the treatment time. Patients were grouped based on their pathological clinical response determined post-chemotherapy. All values were normalized to week 0 by subtraction. Error bars represent standard error of the mean.

**Table 4-2.** A comparison of the classification performances (accuracy) of different QUS parameters using the KNN classifier, at weeks 1, 4 and 8. The bold entry indicates the best performance. Reported values are mean and standard deviation of the accuracies obtained by running the classification 10 times using 10 random samples of responders.

	Week 1 Accuracy	Week 4 Accuracy	Week 8 Accuracy
<b>ΔMBF</b>	<b><math>61 \pm 8</math></b>	<b><math>65 \pm 5</math></b>	<b><math>85 \pm 5</math></b>
ΔSS	$53 \pm 8$	$62 \pm 7$	$63 \pm 15$
ΔSI	$55 \pm 8$	$65 \pm 11$	$74 \pm 6$
ΔACE	$54 \pm 8$	$64 \pm 4$	$60 \pm 10$
ΔSAS	$62 \pm 7$	$58 \pm 8$	$69 \pm 7$
ΔASD	$54 \pm 9$	$61 \pm 9$	$60 \pm 13$
ΔAAC	$58 \pm 8$	$64 \pm 9$	$69 \pm 8$

**Table 4-3.** A comparison of the classification results obtained based on tumour size alone (RECIST criteria), based on changes in QUS parameters, and based on changes in QUS parameters plus week 0 QUS parameters. ΔQUS represents [ΔMBF ΔSS ΔSAS] and QUS<sub>w0</sub> represents [MBF<sub>w0</sub> SS<sub>w0</sub> SAS<sub>w0</sub>]. The last row presents the p-value significance of the difference between the mean accuracies of ΔQUS and ΔQUS + QUS<sub>w0</sub> models. Reported values are mean and standard deviation of the accuracies obtained by running the classification 10 times using 10 bootstrap samples from responder group. For QUS results, sensitivity and specificity numbers have denominator of 16 and accuracy numbers have denominator of 32.

	Classification Results									
	Week 1			Week 4			Week 8			
	Sens	Spec	Acc	Sens	Spec	Acc	Sens	Spec	Acc	
<b>RECIST</b>	No.	5/32	9/15	14/47	19/36	6/12	25/48	26/33	4/11	30/44
	%	16	60	30	53	50	52	79	36	68
<b>ΔQUS</b>	No.	$10 \pm 2$	$9 \pm 1$	$19 \pm 3$	$13 \pm 2$	$12 \pm 2$	$25 \pm 3$	$12 \pm 1$	$12 \pm 1$	$24 \pm 2$
	%	$61 \pm 13$	$59 \pm 9$	$60 \pm 10$	$79 \pm 10$	$76 \pm 11$	$77 \pm 8$	$78 \pm 8$	$72 \pm 9$	$75 \pm 6$
<b>ΔQUS + QUS<sub>w0</sub></b>	No.	$12 \pm 2$	$10 \pm 2$	$11 \pm 1$	$13 \pm 1$	$13 \pm 1$	$26 \pm 2$	$12 \pm 1$	$13 \pm 1$	$26 \pm 2$
	%	$76 \pm 11$	$64 \pm 11$	$70 \pm 9$	$80 \pm 9$	$79 \pm 5$	$80 \pm 5$	$78 \pm 9$	$83 \pm 7$	$81 \pm 6$
<b>p-value</b>				0.03*			0.33			0.04*

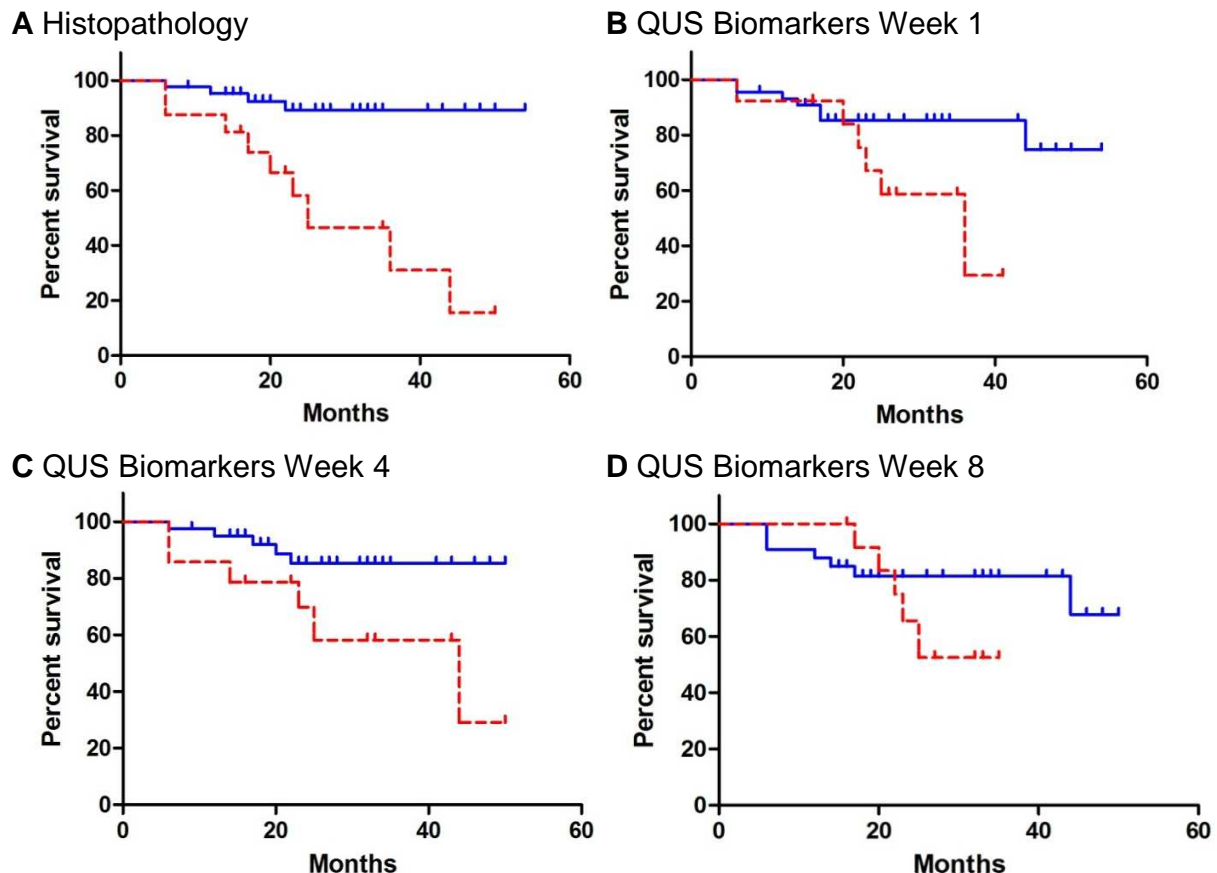


**Figure 4-4.** Kaplan-Meier survival curves for responding (solid line) and nonresponding (dashed line) patients. (A) Patients were classified based on clinical/histopathological information. (B,C,D) Patients were classified based on the QUS biomarkers (including week 0 data) obtained at weeks 1, 4, and 8, respectively.

Table 4-4 lists the misclassified patients at week 4 after classifying the patients using the optimal classification scheme. A leave-one-out classification was performed using the optimal set [ $\Delta MBF \Delta SS \Delta SAS MBF_{w0} SS_{w0} SAS_{w0}$ ] and using all patients, rather than using a random subsample of responders. This was done in order to ensure that all patients were tested. Among the 58 patients at week 4, 14 were misclassified. Observations indicate that 3 of these 14 patients, specifically patients 2, 8, and 10 had HER2 positive breast tumours who were incorrectly predicted as nonresponders at week 4. For better classification performance, one could make HER2 positive patients part of the exclusion criteria. However, this would severely limit the number of eligible patients since HER2 positive patients represent 31% (18/58) of the patients who were subject of this study. The remaining 11 misclassified patients who were HER2 negative had both types of

misclassifications (responder and non-responder). Again, making HER2 negative patients (69%) part of the exclusion criteria would severely limit the number of eligible patients. No other pattern was observed about the misclassified patients. A larger cohort of patients should be analyzed (100+ patients) in order to better understand the outliers.

**Table 4-4.** Clinical/histopathological characteristics of misclassified patients at week 4. The majority were HER2 negative patients (indicated in bold), and the few HER2 positive patients (indicated in italics) all received HER2 receptor-targeted treatments such as Herceptin and Trastuzumab.

Pt No.	Initial Tumour dimensions (AP x ML x SI)	Histology	Grade	ER	PR	HER2	Treatment	Predicted Response
1	<b>13 x 11</b>	IDC	<b>III</b>	-	-	-	<b>AC + paclitaxel</b>	NR
2	<i>6x7x3</i>	<i>IMC</i>	<i>NA</i>	+	+	+	<i>paclitaxel + Herceptin</i>	<i>NR</i>
3	<b>3x3.5x1.5</b>	IDC	<b>III</b>	-	-	-	<b>FEC-D</b>	NR
4	<b>4.9 x 4.9 x 4.1</b>	IDC	<b>III</b>	+	+	-	<b>AC + docetaxel</b>	NR
5	<b>5.2 x 4 x 4</b>	IDC	<b>II</b>	+	+	-	<b>FEC + docetaxel</b>	NR
6	<b>8 x 10</b>	IDC	<b>II</b>	+	+	-	<b>Dose-dense AC + paclitaxel</b>	R
7	<b>4.4 x 3.9 x 5.8</b>	IDC	<b>II</b>	+	+	-	<b>AC + paclitaxel</b>	R
8	<i>2.4 x 2.7 x 3.2</i>	<i>IDC</i>	<i>II</i>	-	-	+	<i>AC + paclitaxel, trastuzumab</i>	<i>NR</i>
9	<b>6.4 x 3.2 x 8.7</b>	ILC	<b>II</b>	+	+	-	<b>FEC-D</b>	R
10	<i>5.4 x 5 x 8</i>	<i>IDC</i>	<i>II</i>	+	+	+	<i>AC + docetaxel, paclitaxel, trastuzumab</i>	<i>NR</i>
11	<b>3.3 x 3.4 x 3.4</b>	IDC	<b>III</b>	-	-	-	<b>TC</b>	NR
12	<b>2.7 x 3.2 x 2.0</b>	IDC	<b>III</b>	+	+	-	<b>ACT</b>	R
13	<b>2.3 x 2.5 x 2.5 &amp; 1.0 x 1.0 x 0.7</b>	IDC	<b>III</b>	-	-	-	<b>AC + paclitaxel</b>	R
14	<b>10 x 5 x 10.5</b>	IDC	<b>III</b>	-	-	-	<b>dose dense AC + taxol</b>	NR

## 4.5 Discussion

This study demonstrated, for the first time, using a relatively large patient database and using a leave-one-patient out classifier evaluation, that multi-parametric quantitative ultrasound applied at a clinically relevant frequency range (<10 MHz) can be used to non-invasively predict breast tumour response to chemotherapy as early as after 1-2 cycles (1-4 weeks) with reasonable accuracy (80%), long before a tumour size change provided discriminative information (many months later (pre-op)). Additionally, RFS analyses performed demonstrated that when the ultrasound biomarkers [MBF, SS, SAS], which include pre-treatment values along with the change at a specified time during treatment, were used to predict the RFS, responder and non-responder RFS rates were statistically significantly different when classifying patients based on data at weeks 1 and 4. Although the results of this study were not used to modify the treatments of the patients, the findings suggest that ultrasound biomarkers can predict the RFS rates of responding and nonresponding patients within weeks almost as accurately as patient ultimate clinical response based on clinical and histopathology information obtained many months later. The reason for the poor separation of the RFS rates of the groups predicted from week 8 QUS data was likely due to initial responses to chemotherapy challenge inherently being more predictive but could be influenced due to the relatively small sample size or other physiological changes.

Previously developed theories about ultrasound detection of cell death support the findings in this study, where just as the parameters related to the backscatter intensity and acoustic concentration (i.e. MBF and SI) increased in tumours undergoing cell death *in vivo* [27], MBF, SI, and AAC values increased in clinically responding tumours in this study. Classification analysis determined that MBF was the most effective parameter in the classification at weeks 4 and 8 (Table 4-2). This is likely due to the fact that MBF is affected by frequency-dependent attenuation whereas SI and AAC are not (they are affected by depth-dependent attenuation). Since changes in ACE obtained at weeks 1 and 4 were statistically significant in responders compared to those of non-responders ( $p = 0.004$  and  $0.039$ , respectively), it is likely that the attenuation correction of the tumour spectra helped in accentuating the MBF parameter to response detection. Furthermore, the MBF changes in the responding-tumour patient population became highly statistically different from those of nonresponding tumours at week 8 ( $p < 0.005$ ). The increase in the ACE observed in responding tumours over treatment time was concordant with the increase in attenuation coefficient with cell death extent observed in previous high-frequency QUS cell treatment characterization studies [62].

Classification analysis demonstrated that increasing the number of QUS parameters submitted to the classification scheme improved the classification, but not beyond three parameters. Whereas previous studies found classical parameters (MBF and SI) to be sensitive to detecting breast tumour response at 4 weeks, I found that MBF, SI, ACE, and AAC all have comparable accuracies in predicting tumour response (65 %, 65 %, 64 %, and 64 % respectively at week 4). Combining the changes and pre-treatment values of MBF, SS, and SAS provided the best prediction of response ( $70 \pm 9\%$  at week 1,  $80 \pm 5\%$  at week 4, and  $81 \pm 6$  and week 8). This may be due to structural tumour properties before chemotherapy being linked to tumour aggressiveness and consequently the likelihood of not responding to chemotherapy.

Other imaging methods have been used in research to assess the therapeutic responses of locally advanced breast tumours, including diffuse optical spectroscopy (DOS) [12], positron emission tomography (PET) [7], and dynamic contrast-enhanced magnetic resonance imaging (DCE-MRI) [7]. Despite a favorable sensitivity in detecting breast tumour response at 4 weeks, DOS has limited tissue penetration depth without complex reconstruction methods, thereby limiting its application to superficial tumours. DCE-MRI remains expensive and requires a contrast agent which can be toxic to patients with kidney diseases and PET requires the injection of radioactive tracer isotopes, limiting repeated usability and imparting potential long term health complications. On the other hand, ultrasound is relatively inexpensive and safe and its imaging methods with respect to quantitative ultrasound rely on the inherent changes in tissue microstructure to generate tissue contrast, requiring no external contrast agents. Recently, a genetic method of monitoring metastatic breast cancer has been proposed, demonstrating circulating tumour DNA as an effective biomarker for this purpose [81]. However, the method is invasive in its nature, and DNA quantification and genetic sequencing are costly and time consuming. The method here does not rely on tumour specific genetic markers but is sensitive to the biophysical changes which accompany cell death – the induction of which is the goal of cancer chemotherapy. Evidence demonstrates that patients who respond well to chemotherapy may benefit from longer regimens of efficacious chemotherapy and suggest that ineffective treatments should be changed [82].

## **Limitations**

Currently the standard of care for patients receiving neoadjuvant chemotherapy only includes pre-treatment and post-treatment imaging, using typically DCE-MRI, but does not routinely include intra-treatment imaging for tumour size assessment. Furthermore, ultrasound imaging is not reliable for tumour size measurement due to attenuation artefacts which cast shadows on the distal end of deep-set tumours. However, this had minimal effect on QUS assessment, since the ROIs were selected in the center of the tumour (~ 90 % coverage), avoiding regions of artefacts. Although tumour size was recorded in this study as measured by the physician during follow-up physical examinations, this method has limited reproducibility since measurements were made by different physicians. Thus, measurements reported here should be assumed approximate.

A point of note is that within the six optimal parameters which were found for treatment response discrimination,  $\Delta\text{MBF}$  (week 0 and 4) parameter was the most accurate single classifying parameter, but  $\Delta\text{SS}$  (week 0 and 4) and  $\Delta\text{SAS}$  (week 0 and 4), were less accurate than other parameters investigated, according to data in Table 4-2. However, since each of these parameters describe independent features of the underlying tissue microstructure, the discriminating power increased when these parameters were combined. Particularly, MBF describes the acoustic concentration, SS describes the size of the scatterers, and SAS describes the distance between regularly-spaced scatterers. Although the large number of selected features (six) compared to the number of observations ( $N=58$ ) may raise concerns of overfitting, the leave-one-patient-out analysis performed on the data has been known to minimize overfitting [83].

The QUS results obtained indicated poor separation between responders and non-responders at the pre-operative scan time. This is expected and likely due to the large time gap between the end of neoadjuvant treatment and surgery (usually several weeks), where minimal or no cell death had occurred at the time of data acquisition. Additionally, tumour ROI selection in pre-operative images was difficult in complete pathologic responders who had no residual tumour, and were therefore excluded from the analysis. As expected the early investigated times at weeks 1 and 4 indicated the best separation between responders and non-responders. These were selected to span cycles of chemotherapy and it remains unknown if other times sooner or later would be useful for analyses. Despite this the sensitivity and specificity and consequent accuracy were significant for predicting ultimate patient clinical response.

## **Conclusions**

In summary, this study demonstrated for the first time, using a relatively large patient cohort and leave-one-out classifier evaluation, that the hybrid QUS biomarker [ $\Delta$ MBF,  $\Delta$ SS,  $\Delta$ SAS] can, with good sensitivity and specificity, detect the response of LABC tumours to neoadjuvant chemotherapy as early as after 1 cycle (1 week) of administration. Extending efficacious treatments and switching ineffective ones early based on indications of QUS biomarkers may likely result in improved RFS. The findings of this study also provided insight into pre-treatment ultrasonic scattering properties of a tumour potentially contributing to a prediction about its therapeutic resistance before the initiation of therapy.

## 5 Summary and future directions

## 5.1 Summary and conclusions of thesis

Breast cancer is the most common cancer among Canadian women [1] and its heterogeneity of response necessitates personalization of therapy [73]. Although neoadjuvant chemotherapy prior to surgery is the clinically favourable option for patients with locally advanced breast cancer, different patients respond differently to the same chemotherapy and currently, the response is not known until completion of a therapy spanning several months. Various chemical- and image-based biomarkers have been developed to probe early changes in tumour function/metabolism. Biochemical methods include analysis of apoptotic index, Ki-67, and Bcl-2 from tumour biopsy samples. Image-based methods include DW-MRI, FDG-PET, and DOI imaging. This thesis evaluated—for the first time—the capacity of ultrasound (particularly quantitative ultrasound) in detecting early changes in tumour microstructure related to cell death response to chemotherapy in a clinical setting. Ultrasound has a number of advantages including relatively low cost, short imaging time, high resolution, radiation-free nature, and intrinsic tumour contrast which does not require injection of any contrast agents.

Chapter 2 demonstrated *in vivo* that certain ultrasonic scattering properties estimated from backscatter coefficients are linearly correlated to the cell death fraction (CDF). Whereas previous studies had demonstrated a correlation between linear regression spectral parameters (i.e. MBF and SI) and CDF at the clinically relevant frequency range [27], this thesis demonstrated, in the same frequency range, that normalizing advanced QUS parameters such as AAC to initial tumour volume will result in improved correlation to CDF ( $r^2$  for  $\Delta$ AAC was 0.399, for  $\Delta$ AAC<sub>VN</sub> was 0.639). This suggests that QUS parameters are affected by initial tumour volume, which is associated with the presence and prevalence of hypoxic and/or necrotic cores within the tumour (larger tumours often have hypoxic, necrotic cores). The findings of this study provided a framework for QUS analysis in the subsequent clinical studies in Chapters 3 and 4. Specifically, the scattering model to use for estimating ASD and AAC was determined (the spherical Gaussian model), and the CDF related to QUS changes was evaluated early (4 to 48 hours) from chemotherapy onset, in order to mimic the changes expected in clinical breast tumours within a few days of initiating a course of chemotherapy.

In Chapter 3, the QUS characteristics of clinical breast tumours versus normal breast tissue and different grades of breast tumours were investigated. The true labels were obtained from biopsy

information. It was demonstrated that the combination of AAC and SAS can be used to differentiate breast tumours from surrounding breast tissue with 88% using a quadratic discriminant function. Furthermore, grade I breast tumours could be differentiated from grade II–III tumours using the combination of means and textures of QUS parametric images of MBF, SS, SI, SAS, ACE, ASD, and AAC with an accuracy of 86%. The accuracy was based on leave-one-patient-out cross-validated classification results. In a clinical setting, the incorporation of QUS assessment of the breast during or after an ultrasound-guided breast biopsy session potentially may permit cross-verification of the histological findings.

In Chapter 4, the QUS characteristics of LABC patients undergoing neoadjuvant chemotherapy were investigated using a multiparameter approach employing machine learning methods. Patients were classified as responders or nonresponders, where the true response was based on clinical/histopathological information obtained at the end of the treatment. Employing the k-nearest neighbour classifier and leave-one-patient-out evaluation, it was determined that the combination of MBF, SS, and SAS can be used to differentiate responders and nonresponders with accuracies of  $60 \pm 10\%$ ,  $77 \pm 8\%$ , and  $75 \pm 6\%$  at weeks 1, 4, and 8 respectively. Furthermore, when pre-treatment QUS measurements were included in the classification, the accuracies improved ( $70 \pm 9\%$ ,  $80 \pm 5\%$ , and  $81 \pm 6\%$ , at weeks 1, 4, and 8 respectively). Tumour biomarker studies have demonstrated that increased tumour apoptosis is associated with positive response, which is associated with improved patient survival. Thus, the clinical implication of this finding is that patients undergoing neoadjuvant chemotherapy of LABC can potentially benefit from a weekly QUS assessment in order to evaluate the early response of the tumour and alter the regimen if the tumour was nonresponsive.

There are, however, limitations to the proposed method which clinicians should be aware of. First, the method is not 100% sensitive nor 100% specific at classifying responding patients versus nonresponding patients. It was shown in Chapter 4 that patients with HER2-negative breast cancers and those receiving HER2-targeted treatments may not benefit from this approach as our investigated QUS parameters are not sensitive nor specific to this type of cancer or treatment type. Investigation is underway to discover new QUS features that may be more sensitive and specific to response prediction. Some potentially effective approaches are GLCM-based texture analysis which were demonstrated in chapter 3 to be effective in characterizing LABC tumour subtypes when combined with mean QUS features. Additionally, increasing the number of patients in such

a study may permit the classifier to better learn the data and result in higher sensitivity and specificity. If performance does not improve, our QUS methods may be used in conjunction with other methods such as DW-MRI, PET, and/or DOS to potentially improve the response detection performance compared to using any one method alone.

Another limitation of our proposed technique is that the definition of true response is based on bulk tumour shrinkage post-treatment as well as residual tumour cellularity. However, accurate measurement of tumour shrinkage requires accurate delineation of tumour boundaries, which becomes especially difficult as the tumour undergoes morphological changes in response to treatment. Additionally, tumour cellularity (high or low) can be subjective depending on the pathologist examining the specimen. Researchers are developing more accurate and functional response markers such as Ki-67 and AI, which have been demonstrated as predictive of both response and disease-free survival [8][9]. Thus, a better understanding of the relation between our measured QUS features and the tumour's biological changes may be gained if correlation analyses were performed between QUS features and these biomarkers.

## 5.2 Future directions

The idea of extending QUS-based response monitoring to other cancer sites is promising. One potential site would be the prostate. The standard of care for patients with hormone refractory prostate cancer is chemotherapy, due to its demonstrated prolonged survival [84]. However, no imaging method for monitoring the response of these patients to chemotherapy is available in the clinical setting, although molecular analysis based on circulating tumour cells has been proposed as a potential method [85]. Quantitative ultrasound imaging has demonstrated superior capability in delineating prostate cancers compared to conventional B-mode images, for guidance of prostate biopsies and treatments [86]. Thus, there is promise that similar QUS techniques can also be used to track changes in the prostate tumour during chemotherapy.

One of the challenges in this thesis was the lack of three-dimensional ultrasound data. Three-dimensional (3D) imaging is important in medicine for visualizing the extent of disease and its surrounding anatomy. Availability of 3D ultrasound data from the whole breast would facilitate identification and tracking of the tumour from one scan session to another, especially when substantial changes in tumour morphology occur during treatment. 3D reconstruction from

freehand ultrasound scanners is difficult due to the irregular spacing and orientation of the image planes. Reconstruction algorithms have been proposed with limited success [87]. An alternative solution is the use of 3D ultrasound imaging systems, such as ultrasound computed tomography (Figure 5-1) and rotating concave transducer technologies (Figure 5-2).

The issue of variability in ROI selection arose on multiple occasions during the manuscript review processes. Since tumour ROIs were selected manually, the user variation of the ROI selection results in variations in QUS features and difficult reproducibility. An automated breast tumour segmentation process might alleviate such issues. Numerous algorithms have been proposed, such as local texture analysis and clustering approaches [88], [89]. Such approaches have demonstrated high sensitivity and specificity in terms of similarity to the radiologist's manual delineations (92% sensitivity and 93% specificity for the clustering approach, 95% sensitivity and 92% specificity for the local texture approach). However, these methods were tested on high-contrast tumours in ultrasound images. Some breast tumours have low ultrasound contrast, for which segmentation results were not reported in those studies, and will likely fail. Perhaps the optimal choice would be to have a semiautomated tumour ROI selection, where the low-contrast tumours are selected manually.

In regards to the ground truth determinations of patient responses, a limitation exists: the ground truth is based on preoperative MRI and histopathological findings on the postsurgical breast specimen. These data are obtained at the end of the several-month neoadjuvant treatment whose effectiveness is under assessment. No ground truth is available at times concordant with QUS assessment (i.e. weeks 1, 4, and 8). One way to address this issue and improve the experimental design is to use existing molecular biomarkers such as apoptotic index (AI) and proliferation (Ki-67) as reference measures of response, as suggested in one study [8]. One can measure Ki-67 by immunocytochemical analysis and AI by flow cytometric analysis of fine needle aspiration biopsy samples obtained coincident with the QUS imaging sessions. This can help identify the biological changes occurring in the tumour to which QUS parameters are sensitive. If the changes in QUS parameters were correlated with AI, then the expectation that QUS changes are correlated with therapy-induced tumour cell death in the human breast will be confirmed.

The quantitative ultrasound treatment monitoring technique used in this thesis has recently received interest from the health care and research communities and fundraising is underway to

launch a multicentre trial. This technology has been branded as WaveCheck. With ongoing patient recruitment at Sunnybrook Health Sciences Centre in Toronto, Ontario, Canada, the long-term goal is to obtain convincingly high sensitivity and specificity in patient response prediction using a large database of over 100 patients, and in conjunction with results of the multicentre trial, obtain Health Canada approval of the technology for clinical use. Patients with locally advanced breast cancer are usually very young and their poor outcomes result in the loss of many years of life with significant implications for their families and society. With this technology in place to objectively measure tumour response based on measuring functional changes, ineffective therapies affecting the primary disease and potential metastases could be changed to more efficacious ones that improve treatment outcomes.

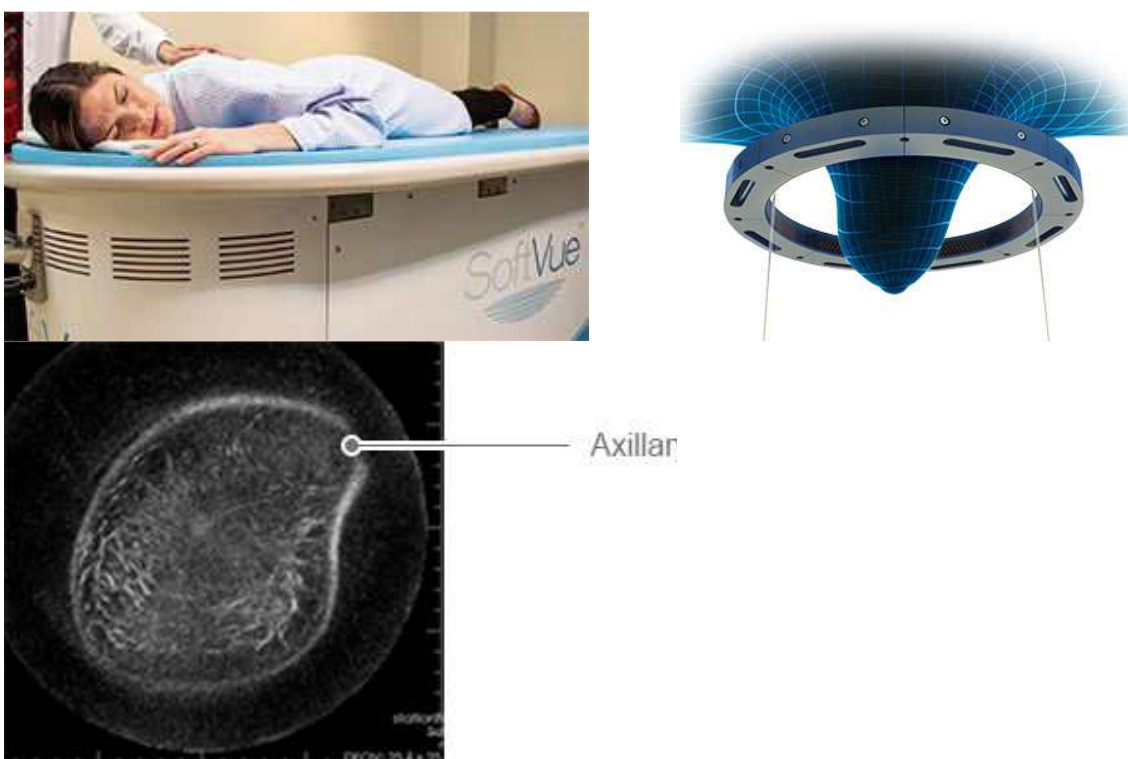


**Figure 5-1.** SoftVue Ultrasound computed tomography system. The system comprises of over 2000 transducer elements arranged in a ring which operate both in transmission and reflections modes. Adapted from Delphinus Medical Technologies (<http://www.delphinusmt.com/our-technology/softvue-system>)

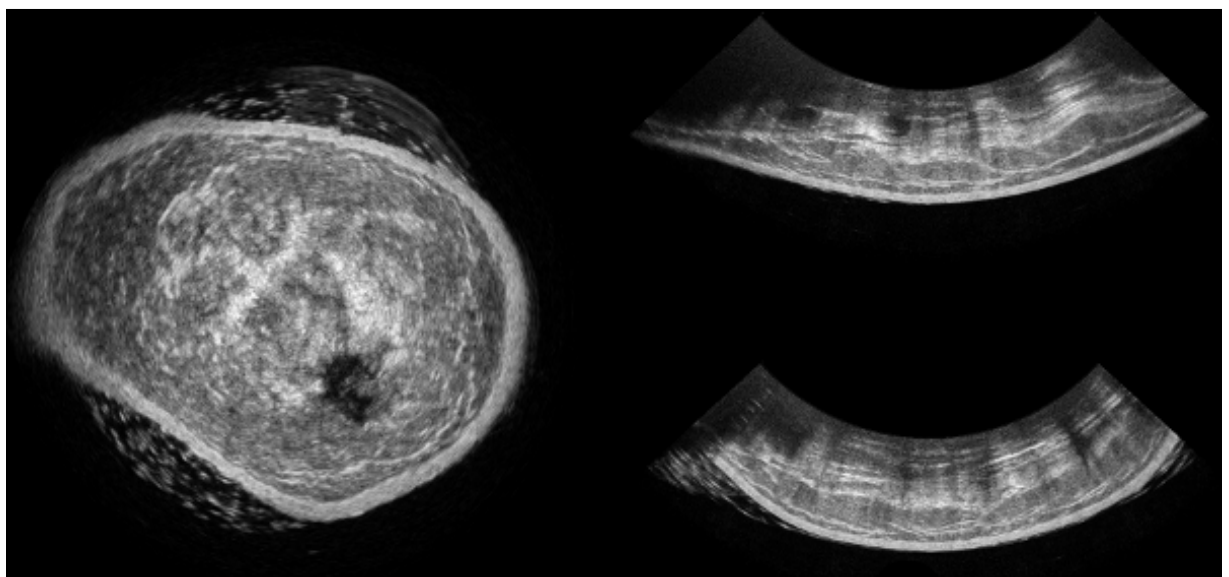


**Figure 5-2.** Using a patented 360 degree rotating concave ultrasound transducer, SonixEmbrace Research captures realistic, uncompressed images of a breast, while the patient lies in a comfortable, prone position. The system captures gigabytes of raw data, which is ideal for cancer detection research and treatment monitoring. Adapted from Analogic Ultrasound (<http://www.analogicultrasound.com/research/clinical/applications/breast-cancer>)

# Appendix

## Analytical solution for the scattering from solid spheres

James Faran derived the equation of the scattered pressure by a solid sphere of radius  $a$  in a fluid-like medium that is insonified by a plane harmonic wave,  $P_i = P_0 e^{-jk_3 r \cos \vartheta}$ . With the assumption of distant observation point ( $r \gg a$ ), the solution was obtained by spherical wave decomposition, yielding,

$$|P_{sc}(k, r)| \approx \frac{P_0}{k_3 r} \left| \sum_{n=0}^{\infty} (2n+1) \sin(\eta_n) e^{j\eta_n} P_n \cos \vartheta \right| \quad \text{for } r \gg a \quad \text{A1}$$

where  $k_3$  is the wave number defined as  $\frac{2\pi f}{c_3}$ , where  $c_3$  is the speed of sound in the medium surrounding the scatterer,  $r$  is the observation point,  $n$  is the order number,  $\vartheta$  is the angle of incidence,  $P_n$  is the Legendre polynomial, and  $\eta_n$  is defined by,

$$\eta_n = \tan^{-1} \frac{\tan(\delta_n(x_3)) [\tan(\phi_n) + \tan(\alpha_n(x_3))]}{[\tan(\phi_n) + \tan(\beta_n(x_3))]} \quad \text{A2}$$

$$\delta_n = \tan^{-1} \left[ -\frac{j_n(x_3)}{n_n(x_3)} \right] \quad \text{A3}$$

$$\alpha_n = \tan^{-1} \left[ -\frac{x j'_n(x_3)}{j_n(x_3)} \right] \quad \text{A4}$$

$$\beta_n = \tan^{-1} \left[ -\frac{x n'_n(x_3)}{n_n(x_3)} \right] \quad \text{A5}$$

$$\phi_n = \tan^{-1} \left[ -\frac{\rho_3}{\rho_1} \tan \xi_n(x_1, \sigma) \right] \quad \text{A6}$$

$$\xi_n(x_1, \sigma) = \tan^{-1} \left[ -\frac{\frac{x_2^2}{2} \left[ \frac{x_1 j'_n(x_1)}{x_1 j'_n(x_1) - j_n(x_1)} - \frac{2(n^2+n) j_n(x_2)}{(n^2+n-2) j_n(x_2) + x_2^2 j_n''(x_2)} \right]}{\frac{x_1^2}{x_1 j'_n(x_1) - j_n(x_1)} \left[ \frac{\sigma}{1-2\sigma} j_n(x_1) - j_n''(x_1) \right] - \frac{2(n^2+n) [j_n(x_2) - x_2 j'_n(x_2)]}{(n^2+n-2) j_n(x_2) + x_2^2 j_n''(x_2)}} \right] \quad \text{A7}$$

$$x_1 = k_1 a$$

$$x_2 = k_2 a$$

$$x_3 = k_3 a$$

A8

where  $\sigma$  is the Poisson's ratio of the scatterer,  $j_n$  and  $n_n$  are the spherical Bessel functions of the first and second kind, respectively, the primes denote derivatives,  $a$  is the scatterer radius,  $k_1$  is the wavenumber calculated from the compressional wave speed in the scatterer, and  $k_2$  is the wavenumber calculated from the shear wave speed in the scatterer. Note that equation A7 includes Hickling's correction [90] where the factor  $\frac{\sigma}{1-2\sigma}$  is placed inside the brackets rather than outside. Using the definition of the backscatter coefficient,

A9

$$\sigma_{bsc} = \frac{R^2}{V} \frac{\langle I_{sc} \rangle}{I_{inc}}$$

where  $R$  is the distance to the scattering volume, and  $V$  is the scattering volume. Knowing the number of scatterers per unit volume,  $\bar{n}$ , average scattered intensity,  $\langle I_{sc} \rangle$ , and incident intensity,  $I_{inc}$ ,

$$\langle I_{sc} \rangle = \bar{n} V \frac{P_{sc}^2}{2\rho_0 c} \quad A10$$

$$I_{inc} = \frac{P_0^2}{2\rho_0 c} \quad A11$$

One can obtain an expression of the backscatter coefficient of a solid spherical scattering sample as,

$$\sigma_b = \frac{\bar{n}}{k^2} \left| \sum_{n=0}^{\infty} (2n+1) \sin(\eta_n) e^{j\eta_n} P_n \cos \vartheta \right|^2 \quad A12$$

## Patient characteristics

Table A-1. Patient characteristics and administered chemotherapy regimens

Pt No.	Age	Initial tumour Dimensions (AP x ML x SI)	Histology	Grade	ER	PR	HER2	Treatment
1	55	5.4 x 5 x 2.3 cm	IDC	I	-	+	+	FEC and Taxol, Herceptin
2	53	7.4 x 7 cm	IDC with mucineous features	I	+	+	-	Epi and Taxotere
3	41	5.3 x 4.4 x 4.7 cm	IDC	II	+	+	+	Docetaxel, carboplatin, trastuzumab
4	65	RB 10x10cm	IDC	I	-	-	-	AC & Taxotere AC + docetaxel, trastuzumab
5	50	NA	IDC	III	+	+	+	AC + docetaxel, trastuzumab
6	33	3x3cm	IDC	I	+	+	-	AC & Taxol AC + docetaxel, paclitaxel, trastuzumab
7	33	5.4 x 5 x 8	IDC	II	+	+	+	AC + docetaxel, paclitaxel, trastuzumab
8	48	4.9 x 4.9 x 4.1	IDC	III	+	+	-	AC + docetaxel
9	36	4.4 x 3.9 x 5.8	IDC	II	+	+	-	AC + paclitaxel
10	40	4.4 x 3.4	IDC	III	-	-	-	AC + paclitaxel FEC + docetaxel
11	62	12 x 14	IDC	II-III	-	-	-	AC + paclitaxel AC + cisplatin,
12	59	6 x 2.3 x 4.3	IDC	III	-	-	-	gemcitabine platinum
13	53	8.4 x 9.4 x 12.7	Metaplastic carcinoma	III	-	-	-	AC-Taxol and Herceptin
14	48	7 x 9 cm	IDC	II	+	+	+	AC + paclitaxel Docetaxel, trastuzumab
15	50	13 x 11	IDC	III	-	-	-	AC + paclitaxel AC + paclitaxel, trastuzumab
16	49	7.1 x 5.5 x 8.9	IDC	III	-	-	+	AC + paclitaxel, trastuzumab
17	40	3 x 2.4 x 3	IDC	III	+	+	+	AC + paclitaxel, trastuzumab
18	56	2.4 x 2.7 x 3.2	IDC	II	-	-	+	AC + paclitaxel, trastuzumab

19	49	2.4 by 2.8 x 1.4 cm	IDC	II	-	-	+	AC-Taxol and Herceptin
20	47	5.2 x 4 x 4	IDC	NA	+	+	-	FEC + docetaxel
21	52	4.1 x 3 x 2.5	IDC	NA	+	+	-	AC + docetaxel, paclitaxel
22	44	9.9 x 4.5 x 9.7	IDC	III	+	+	+	AC + paclitaxel, trastuzumab
23	38	9 x 6.6 x 6	IDC	NA	+	+	-	AC + paclitaxel
24	58	1.9 x 1.4 x 1.6	IDC with basal like features	III	-	-	-	AC + paclitaxel
25	35	5.9	IDC	III	-	-	-	AC-Taxol
26	38	8 x 8	IDC	III	-	-	+	Dose-dense AC + paclitaxel, trastuzumab
27	47	8 x 10	IDC	II	+	+	-	Dose-dense AC + paclitaxel
28	57	7.9 x 4.1 x 5.5	IDC	III	-	-	-	Dose-dense AC + paclitaxel
29	47	6.3 x 4.1 x 7.4	IDC	NA	-	-	+	Dose-dense AC + paclitaxel, trastuzumab
30	55	6.6 x 12.8 x 6.8	IDC	NA	+	+	-	AC + paclitaxel
31	32	6x7x3cm	IMC	NA	+	+	+	AC + paclitaxel + Herceptin
32	38	2.3 x 2.5 x 2.5 & 1.0 x 1.0 x 0.7	IDC	III	-	-	-	AC + paclitaxel
33	45	6.5 x 5 cm	IDC	I	+	+	+	AC-Taxol + Herceptin
34	55	10 x 5 x 10.5	IDC	III	-	-	-	dose dense AC + taxol
35	59	8 x 5.7 x3	IDc	II	+	+	+	FEC + docetaxel, trastuzumab
36	37	2.5 x 2 cm (TV x AP) (our US)	IDC	III	+	+	-	dose dense AC + taxol
37	50	9 x 7 x 3	IDc	II	+	+	-	AC + paclitaxel
38	54	2.3	IDC	NA	+	-	-	TC
39	55	1.6 x1.2cm	ILC @ 12H; IDC @ 2H	NA	+	+	-	FEC-D
40	50	7.3 x 2.5 x 7.3 cm (SI x TV x AP)		III	-	-	-	FEC-D
41	55	3.3 x 3.4 x 3.4	IDC	III	-	-	-	TC

42	44	3x3.5x1.5 cm (SI x AP x TV)	IDC with prominent lymphoid stroma	III	-	-	-
43	60	8.7 x 9 x 5.2 cm (Si x Ap x TV)	Invasive lobular carcinoma	NA	+	-	-
44	64	6.4 x 3.2 x 8.7 cm (US)	ILC(Invasive lobular carcinoma)	II	+	+	-
45	67	3.2 (AP) cm x 8.7	IDC	II	-	-	-
46	52	2.6 x 1.2 x 1.6cm (MRI) whole breast	IDC	II	-	-	-
47	47	replaced by tumour	IDC	III	-	-	-
48	56	10 x 10cm	IDC	II	+	+	+
49	45	2.3 x 2 cm	IDC	NA	+	+	+
50	59	4.9 x 2.1 x 1.4	IDC	II	+	+	-
51	66	3.5 x 5.2 x 2.1 cm	IDC	II-III	+	+	+
52	49	1.8 x 2.1 x 2.1	IDC	I	+	+	+
53	39	6.3cm	Invasive carcinoma with ductal & lobular features	NA	+	+	-
54	62	4.4 x 6.3 x 3.3 cm	IDC	III	-	-	-
55	58	5.2 x 5.2 x 4.4	IDC	I	+	+	+
56	58	2.3 by 4 by 2.3;1.6 by 1.8 x 1.6 cm	IDC	III	-	-	+
57	45	2.7 CC x 3.2 AP x 2.0 TV cm	IDC	III	+	+	-
58	29	4.2 x 2.9 x 2.7	IDC	III	+	+	-

Table A-2. Response of patients to administered regimens  
Residual tumour

Pt no.	size	DCIS Extent	Notes	Response
1	no residual	absent	Complete pathological response	good
2	7 x 5 x 3 cm	absent	Carcinoma with mucinous features; Very low cellularity	good
3	2.7 x 2.5 x 2.4	5 to 10	Tumour cellularity remains very high	poor
4	1.6 x 0.8 x 0.5 cm	<5		good
5	No residual	absent	Complete pathological response	good
6	1.4cm	NA	Good response	good
7	no residual	NA	Complete pathological response	good
8	1.4 x 1 x 1	20	Small volume of invasive tumour remaining	good
9	11.4	<5	Extensive residual disease	poor
			Complete pathological response, with only fibrous tumour bed remaining	
10	no residual	NA		good
11	No residual	NA	Complete pathological response	good
12	2.6 x 2.5 x 2.5	absent	Good response	good
13	whole breast	NA	Residual tumour took up all the breast; no response	poor
14	5cm	NA	she did not respond to first drug	poor
15	4cm	absent	Good response	good
			Complete pathological response, with only in situ disease remaining	
16	no residual	100 (2 x 1.5 x 1cm)	Complete pathological response, with only in situ disease	good
17	no residual	100%(0.2 x 0.2 cm)	remaining	good
18	0.2 x 0.2	absent	Very good response	good
19	1.4 x 2.4 x 1.4 cm	90	0.1 cm	good
			Invasive carcinoma grows in single cells and nest of few cells.	
			Although the overall size of invasive carcinoma is 6.5 cm, the cellularity is exceedingly low thus the overall volume of the tumour is	
			also very low. Probable or definite response	
20	6.5	5 to 10	Complete pathological response, with only in situ disease	good
21	no residual	100%(1x0.7x0.6cm)	remaining	good

	2 x 1 x 1 & 1.6 x 1 x			
22	0.5	80	Good response, tumour cellularity is low	good
23	2.9 x 2 x 1.5 & 2 x 1.5 x 1	60	Tumour cellularity is low Complete pathological response, with only fibrous tumour bed remaining	good
24	0.15	100%(1.5mm)	remaining	good
25	no residual	absent	complete response	good
26	No residual	absent	Complete pathological response	good
27	12.5 x 4.5 x 3.5	<5	No definite response No residual invasive carcinoma in the breast, only lymphovascular invasion remaining	poor
28	no residual	absent	Complete pathological response, only scattered in-situ component remaining	good
29		scattered (small amnt)	remaining	good
30	17	<5%	No definite response bed of scattered microscopic cancer foci; tumour focus is 0.6cm	poor
31	7.4cm 2.8(3.8) x 3.02.2) x 2.3(2.2) & 1.5 x 1.6	5 to 10	0.6cm	good
32	x 1.1	<5%	No definite response multiple foci of invasive carcinoma	poor
33	2.8 + 2 cm	30		poor
34	2foci (0.3+0.5mm)	absent		good
35	No residual	absent	no residual	good
36	2.2 x 1.5 x 1.1 cm, single focus	<5		poor
37	1.2	14.54545455	Small volume of invasive tumour remaining	good
38	5.5	6.666666667	scattered clusters	good
39	1.2 x 0.9 x 0.7 cm	<5	multiple foci of invasive carcinoma	poor
40	2.1cm	60	cellularity 20%; scattered small clusters of tumour cells	good
41	1.8 cm no residual carcinoma	absent	Single focus of invasive carcinoma; no def rep	good
42	2 foci of invasive carcinoma; 8.0 x 5.0 x 4.5 cm and 3.0 x	absent		good
43	2.5 x 1.7 cm	absent		poor
44	19cm	absent		poor

45	3.2 x 3 x 1.8 cm	absent	no definite response but marked chemo therapy effect	good
46	2.5 x 0.4 x 0.4 cm	5 to 10	low cellularity	good
47	4.5 x 3.1 x 2.9 cm	<5		good
48	8.4 x 5.1 x 2.8 cm	absent		good
49	no residual	0.9cm (100%)		good
50	2.8 x 2.5 x 1.5 cm	<5		good
51	4 x 3 cm	<5	Within the scar there	poor
52	no residual IDC	1.6cm (100%)	firm tumour;multiple foci of invasive carcinoma; extensive fibrosis; path says probable to definite response	good
53	1.7x1.5x1 cm	present (extent unknown)	single focus of invasive carcinoma	good
54	12.6 x 6 x 3 cm	5 to 10	The tumour bed is identified wih diffuse fibrosis but residual tumour is present in slices 8&9 (1.7cm each).The largest contiguous focus is 1cm while most areas have low volume tumour in a	poor
55	3.4cm	absent	background of fibrosis	good
56	no residual	absent	complete pathological response	good
57	3cm	<5	multiple foci of invasive carcinoma	poor
58	4cm	70	single focus of invasive carcinoma	poor

# Transducer characterization and validation of scatterer size and attenuation estimation

## Overview and background

This chapter is intended to address two aims: to characterize the imaging transducers and to develop algorithms for *in vivo* estimation of BSC, ASD, and ACE using a reference phantom. The transducers were characterized by computing their point-spread functions to estimate their beam width, depth of focus, and frequency response (i.e. center frequency and bandwidth).

Average scatterer diameter is an important parameter in tissue characterization and has been used to characterize various tumours in mouse models, including mouse mammary carcinomas, rat mammary fibroadenomas, and sarcomas [21], [57]. There, the BSC was estimated from the normalized power spectrum using a quartz plate as the calibration material. ASD was then estimated by minimizing the average standard deviation (MASD) between the estimated BSC and the theoretical BSC (based on the Gaussian form factor) as the method was described in section 1.6 of the thesis. Such method of ASD estimation may be ideal for single-element focused transducers (as was the case for those studies) where placement of tumour ROIs in the focal zone of the transducer is always possible. However, in the case of clinical ultrasound assessment of breasts with large tumours with variable locations, a quartz plate-based spectral calibration may be less accurate. Alternatively, I used a reference phantom to perform spectral calibration (normalization), which better compensates for depth-dependent instrumentation factors [74].

There are mainly four spectral analysis-based methods of attenuation estimation *in vivo*, namely the centroid shift method, hybrid method, reference phantom method, and spectral log difference method [91], [92]. The centroid shift and hybrid methods involve computing the downshift in centre frequency of the power spectrum with depth. The reference phantom method involves computing the spectral difference (i.e. log difference between the sample and a reference phantom with known attenuation coefficient) at different depths (windows) within the ROI at each frequency within the transducer bandwidth and averaging over the frequency points. The spectral log difference method is similar to the reference phantom method, except, instead of using the spectra from windows within the ROI, only the spectra from the proximal and distal windows of the ROI are used to estimate the attenuation coefficient. The centroid method requires depth-dependent spectral calibration using a planar reflector, which can be a difficult task. On the other

hand, reference phantom methods are more practical for use with clinically-relevant frequency (below 10 MHz) array transducers where a large range of depths need to be covered (up to 5 cm). In the literature, the reference phantom method has been frequently applied for characterization of tissues such as the breast and cervix [22], [46]. For this reason, the reference phantom method was employed in this thesis work for in vivo estimation of attenuation coefficients in breast ultrasound data.

## Methods

### Ultrasound imaging systems

For all work completed for this thesis, two standard commercially available ultrasound imaging systems were used. All phantom validation data covered here, and clinical breast data covered in chapters 3 and 4, were acquired with the Sonix RP system (Ultrasonix, Vancouver, Canada), employing a 6 MHz linear array transducer (L14-5W/60). This will be referred to as the clinical transducer. The low-frequency imaging of tumour-bearing mice covered in Chapter 2 was performed using the Sonix RP system employing a 7 MHz transducer (L14-5W/38). The high-frequency data covered in chapter 2 were acquired with a small-animal imaging system, Vevo 770 (Visual Sonics, Toronto, Canada) employing a 25-MHz single-element focused transducer (RMV 710B).

### Transducer characterization

The point-spread function of the transducers were computed using Field II Ultrasound Simulation Program (<http://field-ii.dk/>). The point-spread function was obtained by placing an ideal point target at the focus of the transducer and computing the received sound field. From this field, one can compute the beam width (lateral resolution) from the lateral beam profile, as well as the frequency response by analysis of the Fourier transform of the axial waveform. In order to obtain the depth of focus, pulse-echo measurements were obtained at several locations along the depth of the sound field using a Plexiglas surface.

## Phantom construction

Note that a different phantom with smaller size of glass beads was used for animal imaging (chapter 2) than human imaging, since the animal study involved high-frequency ultrasound that required smaller glass beads as reference. For human imaging studies, a reference phantom was constructed in-house, using 20 % gelatin medium and soda-lime glass beads adapted from [93]. The glass beads were purchased from Cospheric (Santa Barbara, CA) and had a size range of 53–63  $\mu\text{m}$  with density of 2.52 g/cc (model: SLGMS-2.52 53-63um). The bead radius was optically measured to be  $35 \pm 1.7 \mu\text{m}$  (Figure A-1). Figure A-1 depicts the size distribution of the beads using a size histogram, with a best-fit normal distribution superimposed on the graph. The bead size data passed the Shapiro-Wilk normality test, and therefore a normal distribution was assumed. Glass beads were suspended with concentration of 2.2 grams per litre of gelatin medium, and the phantom was left to rotate in a rotisserie overnight to allow the beads to mix uniformly in the gel. Material properties of the phantom and its ingredients are presented Table A-3. The size of the glass beads was selected based on the minimum scatterer size that can be detected by the transducer (6 MHz center frequency) and the expected size of the scattering structures in the human breast. The minimum detectable scatterer size has been reported in the literature to be  $ka = 0.5$  [34], where  $a$  is the scatterer radius and  $k$  is the wavenumber. For a 6 MHz transducer  $ka = 0.5$  corresponds to  $a = 17.5 \mu\text{m}$ . The beads ( $a = 35 \mu\text{m}$ ) for the phantom were selected such that they would be large enough to be ultrasonically detectable and simultaneously small enough to reflect tissue microstructure (i.e. glands or cell aggregates in the breast). For convenience, henceforth, this phantom will be referred to as the CS57 (bead manufacturer initials followed by mean bead size).

Table A-3. Material properties of CS57 phantom and its ingredients. Concentration is relative to agar solution.

Material	Sound speed (m/s)	Mass density (g/cc)	Concentration (g/L)
Soda lime	5572	2.52	2.2
Agar	1540	1.04	NA
Phantom	1540	1.04	NA

## Attenuation coefficient estimation *in vivo*

In order to validate any attenuation coefficient estimation algorithm, the results must be compared against a reference measurement. Here, the reference measurement was made using the insertion loss technique described in section 2.5. Figure A-2 describes the process pictorially. A polished plexiglas was placed in degassed water and the L14-5/60 was focused at the surface of the Plexiglas and the echo was recorded. This signal was referred to as the non-attenuated signal. Next, the CS57 was placed between the transducer and the Plexiglas and the new echo was recorded at three locations (elevations) along the CS57, while maintaining the same distance between the plexiglas and transducer. This signal was referred as the attenuated signal. The amplitude spectra of the attenuated and non-attenuated signals were computed (for each location in the CS57) and a line was fitted to the log difference of the spectra within the – 6dB bandwidth. The slope of this line, normalized to the thickness of the CS57, was computed for each location in the CS57, to give the attenuation coefficient at that location. Ideally for a homogeneous material, the attenuation coefficient will be constant throughout the material. However, due to the presence of inhomogeneities in the CS57, the attenuation coefficient was measured at three locations and consequently averaged. The *in vivo* estimation of ACE uses information about the window spectra of a sample ROI relative to the window spectra of a reference ROI whose attenuation coefficient is known. The slopes of the linear fit to the relative window spectra versus depth are calculated at each frequency and averaged over all frequencies in the bandwidth in order to estimate the ACE at each phantom location. In a similar manner to the insertion loss method, the ACE values were estimated from three locations in the CS57 and were consequently averaged.

## Backscatter coefficient and scatterer size estimation

As mentioned previously, one can estimate ASD from the MASD between the theoretical and measured BSCs. In order to estimate the BSC of the CS57 at low frequency, RF data were acquired from the CS57 at three different depths using the L14-5/60: F-0.5cm, F, F+0.5cm, where F was the focal depth (1.75 cm). Plexiglas echo data were obtained at the three corresponding depths for spectral normalization. Equation **Error! Reference source not found.** was used to compute the BSC from the RF data. For the theoretical BSC, Faran's solution for scattering of rigid spheres was computed for a range of scatterer radii ( $a$ ) of 10-70  $\mu\text{m}$  (mean size of the glass beads was 35  $\mu\text{m}$ ) [29] and scatterer sound speed and density of 5571 m/s and 2.52 g/cc, respectively, and background sound speed and density of 1540 m/s and 1.02 g/cc, respectively. The speed of sound

and density values were based on values reported in previous studies involving a similar phantom [32]. Finally, the MASD between each theoretical BSC and measured BSC was computed.

## Results

### Transducer characterization

Results of sound field simulations and experiments on the clinical transducer are presented in Figure A-3. The detected image (Figure A-3A) shows a diffuse structure radiating from the focus (14 mm). The lateral beam profile (Figure A-3B) shows a peak at the lateral center of the sound field and a - 6dB line shows a -6 dB beamwidth of 0.36 mm (-0.18 to 0.18 mm). The axial waveform (Figure A-3C) was used to obtain the reference power spectrum (Figure A-3D), from which a Gaussian-fitted center frequency of 6.3 MHz and a -6 dB bandwidth of 3-9 MHz were obtained. The actual bandwidth used for data analysis was later adjusted to 3-8 MHz since the experimentally measured phantom spectra showed large fluctuations above 8 MHz which was likely related to noise. The depth of focus plot (Figure A-3E) shows the axial location of maximum pressure (30 mm) and the -6 dB depth of focus is shown to start at 18 mm and extend beyond the maximum depth of the image (4 mm). Pulse-echo measurements were limited to the most commonly used imaging depth for data collections (clinical and phantom), which was 40 mm. Sound fields were computed similarly for the other transducers using Field II and the resulting parameters including center frequency, bandwidth, and lateral resolution are provided in Table A-4.

Table A-4. Transducer specifications obtained from manufacturer and from simulations. Entries with asterisks represent data obtained from simulations and entries without asterisks represent data obtained from manufacturer specifications. DF = dynamic focusing.

Transducer model	Number of Elements	Center Frequency (MHz)	-6 dB Bandwidth (MHz)	Axial Resolution (μm)	Lateral Resolution (μm)	Focal Length (mm)
L14-5W/38	128	~7*	3-9*	220*	360*	DF
L14-5W/60	128	~6*	3-8*	260*	360*	DF
RMV 710B	1	~25*	16-31*	70	140	15

## Attenuation coefficient estimation *in vivo*

Results of attenuation coefficient estimation using insertion-loss and reference phantom methods are presented in Figure A-4 and Figure A-5, respectively. Figure A-4 B and C present the echo signals versus time for the non-attenuated and attenuated cases, respectively. As expected, it can be observed that the insertion of the CS57 in the ultrasound propagation path has resulted in amplitude diminishment (increased attenuation) as well as earlier echo arrival (increased speed of sound). In terms of the spectra (Figure A-4 D and E) the attenuated spectrum is smaller in amplitude and downshifted in center frequency compared to that of the non-attenuated case, which is another effect of attenuation. From the linear fit on the log difference between the two amplitude spectra and the known thickness of the CS57, the attenuation coefficient can be computed, following equation 1.18. This value was determined to be  $0.40 \pm 0.03$  dB/cm-MHz. The mean and standard deviation were obtained by averaging the ACE values obtained from three different locations (elevations) in the phantom.

Results of the attenuation coefficient estimation using the reference phantom method are presented in Figure A4. In Figure A-4A a B-mode image of the CS57, with the transducer focus placed at the center of the phantom, and the ROI used for attenuation estimation can be observed. The ROI was segmented into  $2 \times 2$ mm windows (Figure A-4B) and depth-dependent changes in spectral amplitude were computed. As expected from a homogeneous material, a reasonably strong linear correlation was found between the spectral difference and depth at 5.5MHz, with  $R^2=0.74$ , as shown in Figure A-4C. The ACE of this CS57 was determined to be  $0.47 \pm 0.08$  dB/cm-MHz. The mean and standard deviation were obtained by averaging the ACE values obtained from three different locations (elevations) in the CS57.

The obtained attenuation coefficient values of the CS57 using the two methods are shown in a bar plot in Figure A-5. An unpaired t-test (two-tailed, 95% confidence interval) was performed to compare the means of the ACEs obtained using the two methods, which revealed no statistically significant difference ( $p=0.23$ ).

## Backscatter coefficient and scatterer size estimation *in vivo*

Results of measurement and theoretical prediction of the BSC and estimation of ASD of the CS57 are presented in Figure A-6. Before performing the MASD fitting, a scaling factor was applied to the theoretical BSC in order to match frequency-averaged values of the measured and theoretical BSCs, as follows,

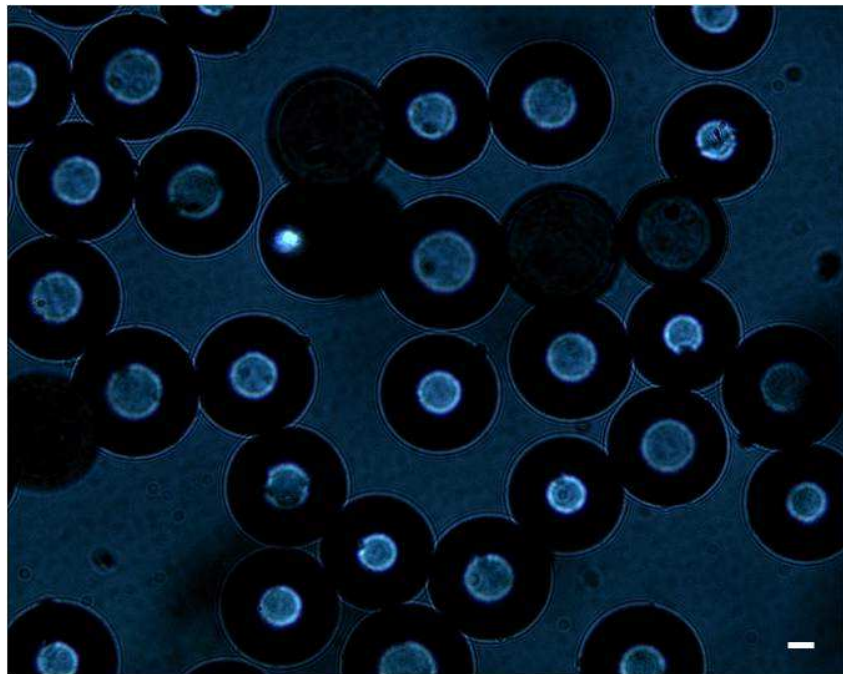
$$\begin{aligned}\sigma_{bs}(k_i) &= \tau\sigma_b(k_i) \\ &= \tau \frac{\bar{n}}{9} k^4 a^6 \gamma^2 F(k, a)\end{aligned}$$

where,

$$\tau = \frac{\sum_{i=1}^N \widehat{\sigma_b}(k_i)}{\sum_{i=1}^N \sigma_b(k_i)}$$

As observed in Figure A-6A, the theoretical prediction of the BSC for 35  $\mu\text{m}$  rigid spherical scatterers fits the measured BSC with a  $R^2$  of 0.74. The BSC measurement shown here was computed from RF echo data collected from the center of the CS57, however BSCs were computed from two other locations (elevations) in the CS57 in order to estimate standard deviations in ASD estimates. Figure A-6B presents a plot of  $R^2$  versus input scatterer radius (model input) for a range of 10-70  $\mu\text{m}$ , demonstrating that the best fit (maximum  $R^2$ ) between the theoretical prediction and measurement of the BSC occur when the scatterer radius is 36  $\mu\text{m}$ . Note that in the reference phantom technique (equation 1.14) of BSC estimation, the MASD metric is used to determine the ASD rather than  $R^2$ . Nevertheless, both metrics result in the same ASD. The  $R^2$  value was shown here since the values always range between 0 and 1 and therefore are more intuitive, compared to the MASD metric.

**A**



**B**

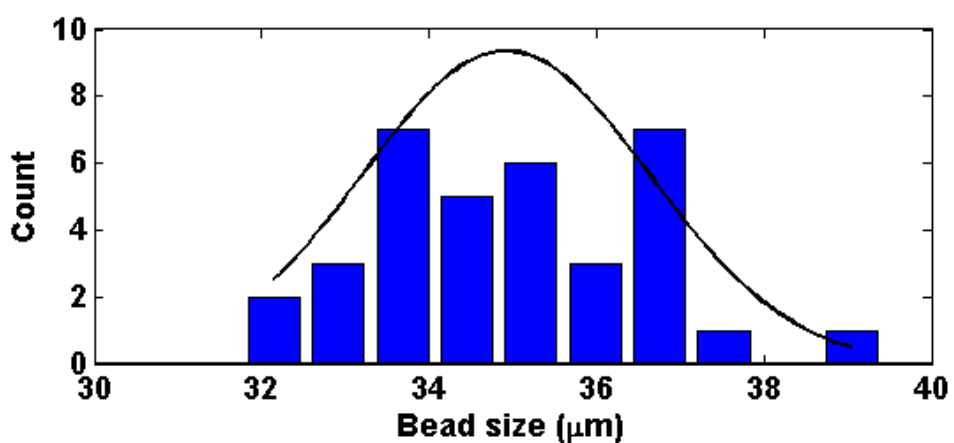


**Figure A-1.** (A) Microphotograph of glass beads embedded in the gelatin-based phantom. Diameters were measured manually using the ruler in ImageJ software (National Institutes of Health, USA). Scale bar: 20  $\mu\text{m}$ . (B) Bead size (radius) distribution with a least-squares-fitted normal distribution (black line). Bin size: 0.77  $\mu\text{m}$  (to obtain 10 equally spaced bins in the measurement range)

A

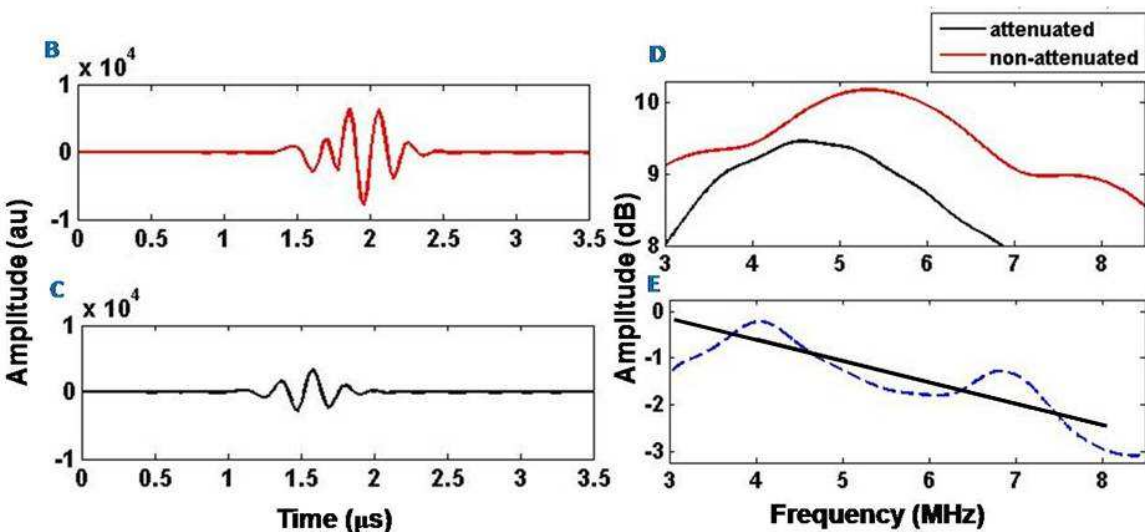
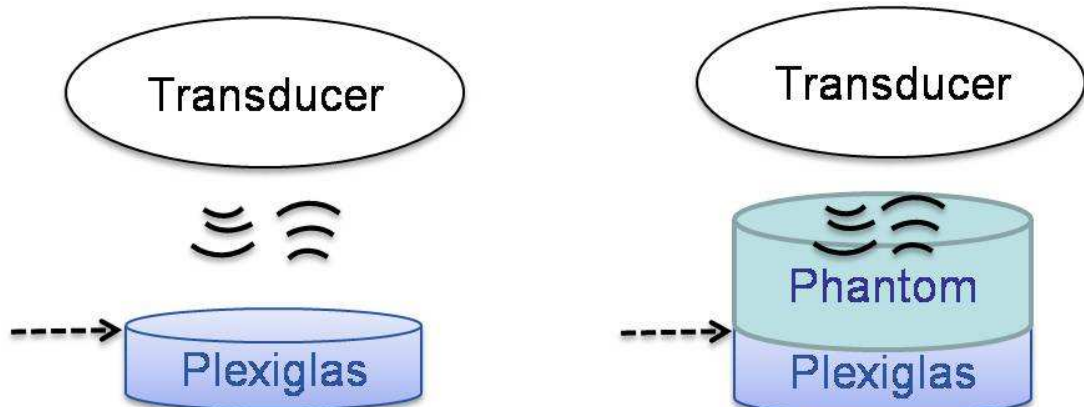
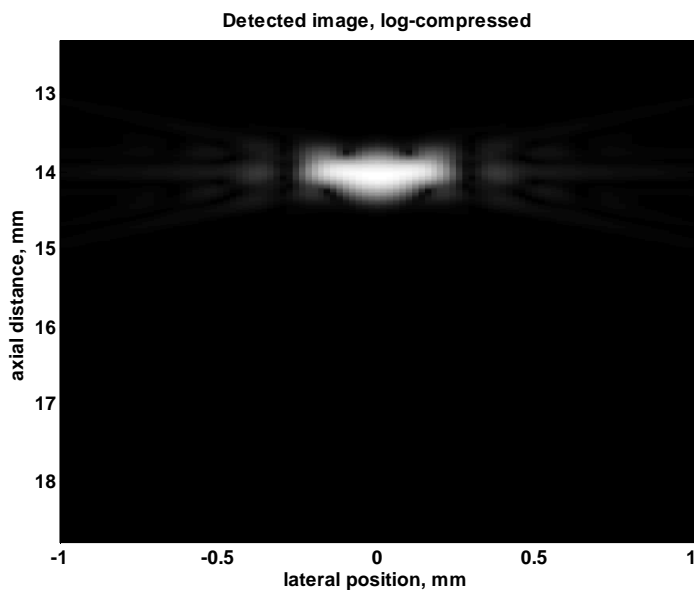
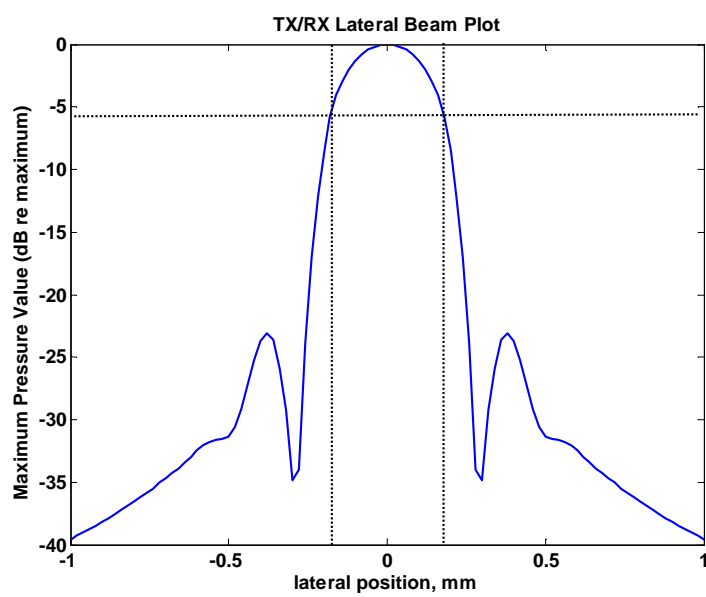


**Figure A-2.** Process of attenuation coefficient measurement using the insertion-loss technique in reflection mode. (A) Diagrams showing (left) reflection from a polished Plexiglas surface inside water medium and (right) reflection from the Plexiglas after passing through the attenuating medium (the phantom). (B) Non-attenuated pulse versus time, (C) Attenuated pulse versus time, (D) amplitude log spectra of the two pulses, and (E) Difference between attenuated log spectrum and non-attenuated log spectrum (dashed plot) with linear fit (solid plot) applied to the – 6 dB bandwidth (3–8 MHz).

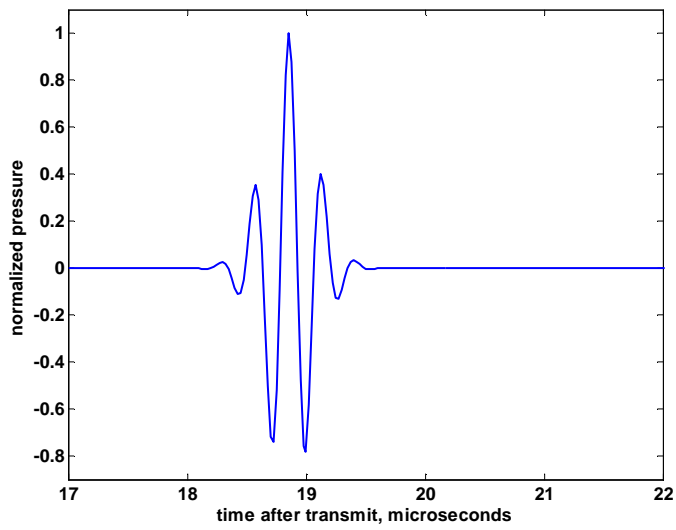
A



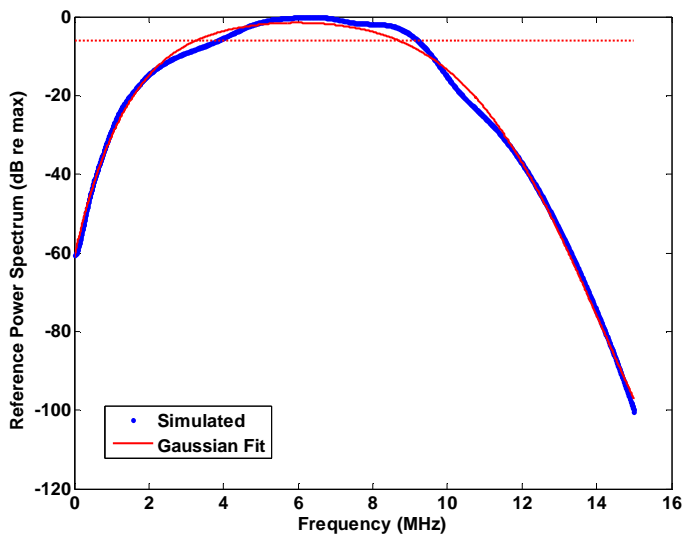
B



C



D



E

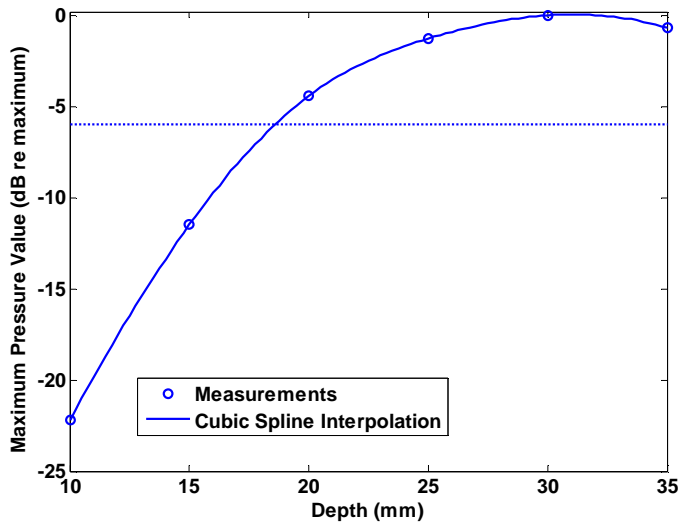


**Figure A-3.** Point spread function of the L14-5W/60 transducer using a one-cycle 10 MHz square pulse excitation. (A) Detected B-mode image. (B) Plot of maximum pressure value versus lateral position at the focal depth (14 mm). The transient line indicates the - 6B beam width. (C) Received pressure versus time at the lateral center of the sound field. (D) Power spectrum of the plot in (C), with Gaussian fit shown in red and -6 dB bandwidth (3-8 MHZ) shown by the transient line. (E) Maximum pressure versus depth obtained by translating the transducer axially through the sound field. The data for this plot were obtained experimentally using a Plexiglas surface to generate the echoes.

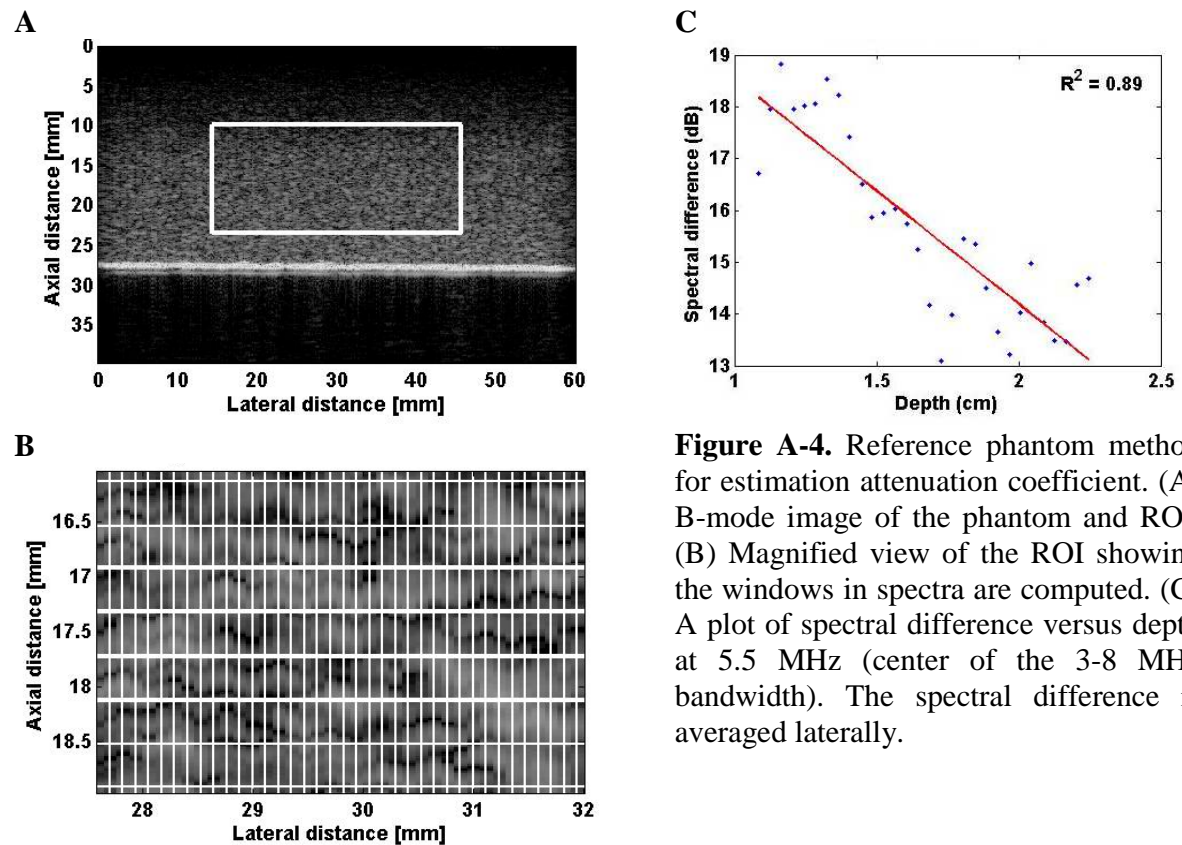


**Figure A-4.** Reference phantom method for estimation attenuation coefficient. (A) B-mode image of the phantom and ROI. (B) Magnified view of the ROI showing the windows in spectra are computed. (C) A plot of spectral difference versus depth at 5.5 MHz (center of the 3-8 MHz bandwidth). The spectral difference is averaged laterally.

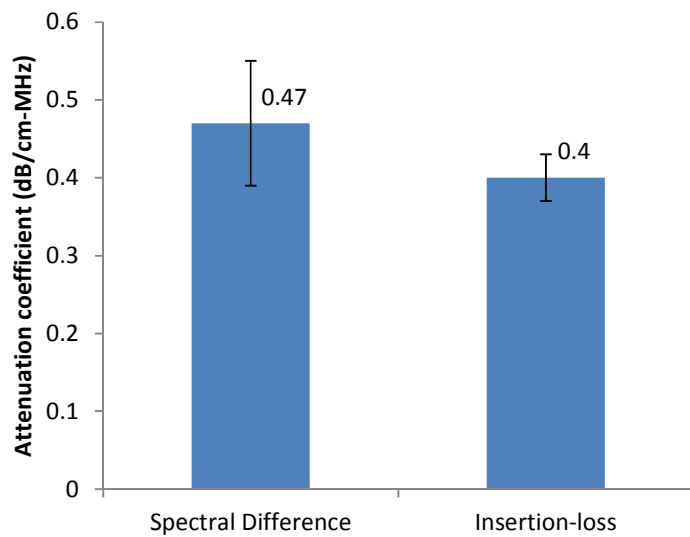
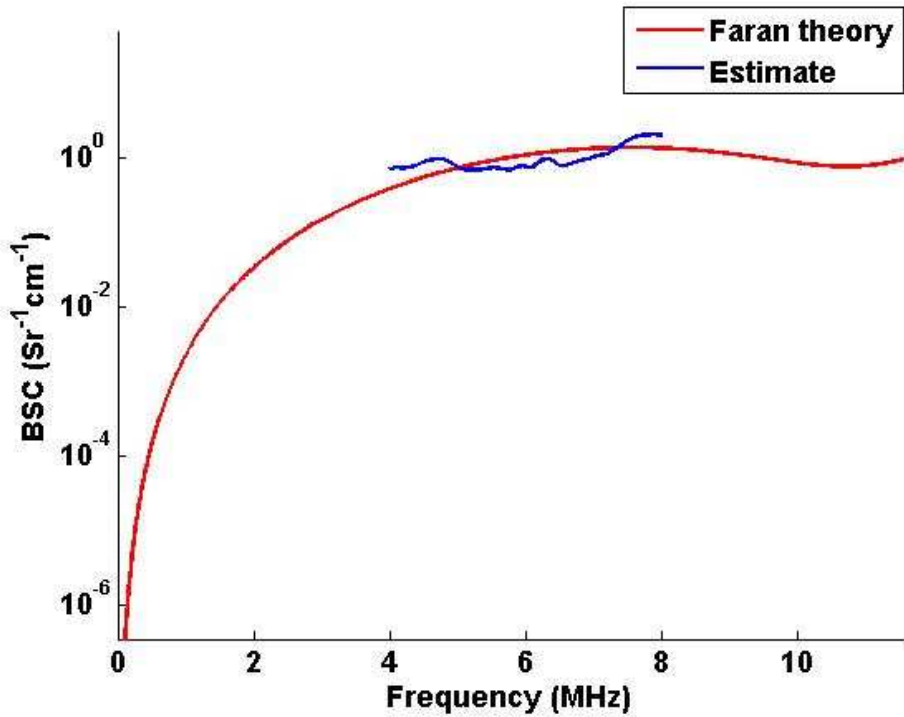


**Figure A-5** Comparison of attenuation coefficients values of the reference phantom estimated using the insertion-loss and reference phantom methods. Error bars represent standard deviation.

A



B

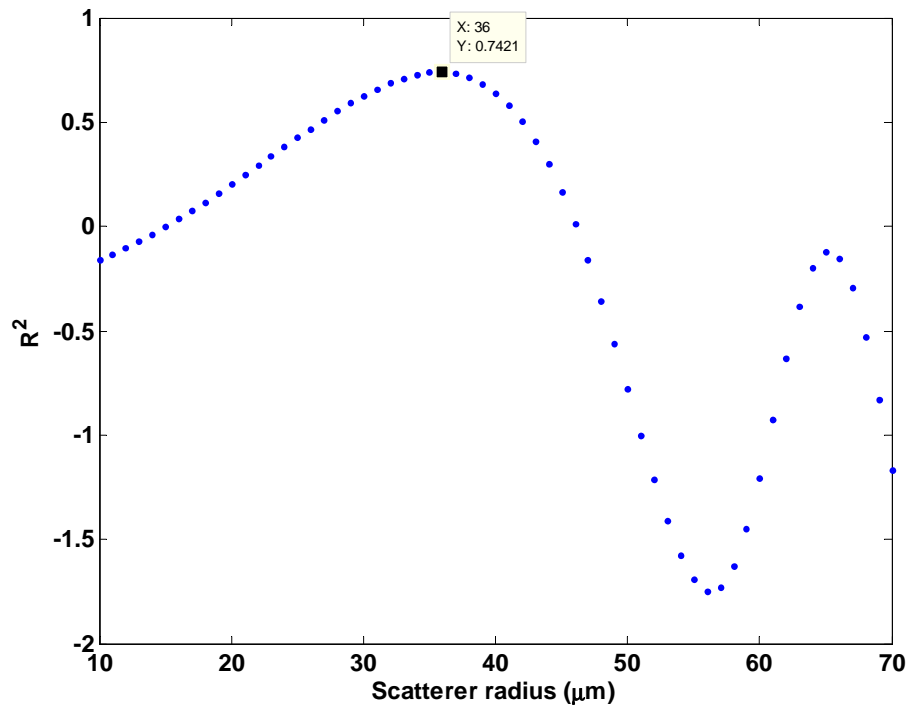


**Figure A-6.** BSC and scatterer size estimation of glass beads in a phantom. (A) Theoretical prediction (red) and measurement (blue) of the BSC as a function of frequency. (B) Coefficient of determination ( $R^2$ ) versus scatterer radius (model input).

## Discussion

In this chapter, sound field characterization was described, construction of a reference scattering phantom was described, the reference phantom method was implemented and validated for *in vivo* estimation of tissue attenuation coefficients, and the scatterer size estimation algorithm was validated. Whereas the axial resolution of the clinical transducer is approximately 260 µm, it was demonstrated that sub-resolution scatterers (35 µm) could be detected from measurement of the frequency-dependence of the backscatter signal from a glass microsphere-embedded phantom. It must be noted that the estimations of ACEs and ASDs are based on a homogeneous acoustic scattering region, and in general, breast tumours present as non-homogeneous acoustic scattering in ultrasound. In such cases, there will be large fluctuations in the spectral amplitude difference with depth, which may result in negative attenuation coefficient estimates (which is physically impossible), and the inclusion of tissue interfaces may result in poor scatterer model fits for ASD estimation. One way to avoid negative ACE is to select multiple smaller ROIs within the tumour, where the backscatter intensities are relatively homogeneous, and use the average ACE obtained from the smaller ROIs. However, ASDs are estimated from 2 x 2 mm windows that make up the tumour ROI. Thus, it is assumed that the windows are small enough to have homogeneous scattering properties for ASD estimation.

## References

- [1] Canadian Cancer Society's Advisory Committee on Cancer Statistics, "Canadian Cancer Statistics 2013," Toronto, 2013.
- [2] B. Yalcin, "Overview on locally advanced breast cancer: defining, epidemiology, and overview on neoadjuvant therapy.," *Exp. Oncol.*, vol. 35, no. 4, pp. 250–2, Dec. 2013.
- [3] A. Kornecki, "Current status of breast ultrasound.," *Can. Assoc. Radiol. J.*, vol. 62, no. 1, pp. 31–40, Feb. 2011.
- [4] A. Karella and S. Vedantham, "Breast cancer imaging: A perspective for the next decade," *Med. Phys.*, vol. 35, no. 11, p. 4878, 2008.
- [5] G. J. Whitman and E. A. Strom, "Workup and Staging of Locally Advanced Breast Cancer," *Seminars in Radiation Oncology*, vol. 19, no. 4. pp. 211–221, Oct-2009.
- [6] E. A. Eisenhauer, P. Therasse, J. Bogaerts, L. H. Schwartz, D. Sargent, R. Ford, J. Dancey, S. Arbuck, S. Gwyther, M. Mooney, L. Rubinstein, L. Shankar, L. Dodd, R. Kaplan, D. Lacombe, and J. Verweij, "New response evaluation criteria in solid tumours: revised RECIST guideline (version 1.1).," *Eur. J. Cancer*, vol. 45, no. 2, pp. 228–47, Jan. 2009.
- [7] K. Brindle, "New approaches for imaging tumour responses to treatment.," *Nat. Rev. Cancer*, vol. 8, no. 2, pp. 94–107, Feb. 2008.
- [8] J. Chang, M. Ormerod, T. J. Powles, D. C. Allred, S. E. Ashley, and M. Dowsett, "Apoptosis and proliferation as predictors of chemotherapy response in patients with breast carcinoma.," *Cancer*, vol. 89, no. 11, pp. 2145–52, Dec. 2000.
- [9] R. Nishimura, T. Osako, Y. Okumura, M. Hayashi, Y. Totoyozumi, and N. Arima, "Ki-67 as a prognostic marker according to breast cancer subtype and a predictor of recurrence time in primary breast cancer," *Exp. Ther. Med.*, vol. 1, no. 5, pp. 747–754, 2010.
- [10] U. Sharma, K. K. A. Danishad, V. Seenu, and N. R. Jagannathan, "Longitudinal study of the assessment by MRI and diffusion-weighted imaging of tumor response in patients with

locally advanced breast cancer undergoing neoadjuvant chemotherapy,” *NMR Biomed.*, vol. 22, no. 1, pp. 104–113, 2009.

- [11] M. Schelling, N. Avril, J. Nährig, W. Kuhn, W. Römer, D. Sattler, M. Werner, J. Dose, F. Jänicke, H. Graeff, and M. Schwaiger, “Positron emission tomography using [(18)F]Fluorodeoxyglucose for monitoring primary chemotherapy in breast cancer.,” *J. Clin. Oncol.*, vol. 18, no. 8, pp. 1689–95, Apr. 2000.
- [12] O. Falou, H. Soliman, A. Sadeghi-Naini, S. Iradjji, S. Lemon-wong, J. Zubovits, J. Spayne, R. Dent, M. Trudeau, J. F. Boileau, F. C. Wright, M. J. Yaffe, and G. J. Czarnota, “Diffuse Optical Spectroscopy Evaluation of Treatment Response in Women with Locally Advanced Breast Cancer Receiving Neoadjuvant Chemotherapy,” *Transl. Oncol.*, vol. 5, no. 4, pp. 238–246, 2012.
- [13] D. J. Coleman, F. L. Lizzi, R. H. Silverman, L. Helson, J. H. Torpey, and M. J. Rondeau, “A model for acoustic characterization of intraocular tumors.,” *Invest. Ophthalmol. Vis. Sci.*, vol. 26, no. 4, pp. 545–50, Apr. 1985.
- [14] E. J. Feleppa, A. Kalisz, J. B. Sokil-Melgar, F. L. Lizzi, T. Liu, A. L. Rosado, M. C. Shao, W. R. Fair, Y. Wang, M. S. Cookson, V. E. Reuter, and W. D. W. Heston, “Typing of prostate tissue by ultrasonic spectrum analysis,” *IEEE Trans. Ultrason. Ferroelectr. Freq. Control*, vol. 43, no. 4, pp. 609–619, Jul. 1996.
- [15] M. Yang, T. M. Krueger, J. G. Miller, and M. R. Holland, “Characterization of anisotropic myocardial backscatter using spectral slope, intercept and midband fit parameters,” *Ultrason. Imaging*, vol. 29, no. 2, pp. 122–34, Apr. 2007.
- [16] J. Mamou, A. Coron, M. L. Oelze, E. Saegusa-Beecroft, M. Hata, P. Lee, J. Machi, E. Yanagihara, P. Laugier, and E. J. Feleppa, “Three-dimensional high-frequency backscatter and envelope quantification of cancerous human lymph nodes.,” *Ultrasound Med. Biol.*, vol. 37, no. 3, pp. 345–57, Mar. 2011.
- [17] F. L. Lizzi, M. Ostromogilsky, E. J. Feleppa, M. C. Rorke, and M. M. Yaremko, “Relationship of Ultrasonic Spectral Parameters to Features of Tissue Microstructure,”

*IEEE Trans. Ultrason. Ferroelectr. Freq. Control*, vol. UFFC-33, no. 3, pp. 319–329, May 1986.

- [18] F. L. Lizzi, D. L. King, M. C. Rorke, J. Hui, M. Ostromogilsky, M. M. Yaremko, E. J. Feleppa, and P. Wai, “Comparison of theoretical scattering results and ultrasonic data from clinical liver examinations,” *Ultrasound Med. Biol.*, vol. 14, no. 5, pp. 377–385, Jan. 1988.
- [19] E. J. Feleppa, F. L. Lizzi, D. J. Coleman, and M. M. Yaremko, “Diagnostic spectrum analysis in ophthalmology: a physical perspective.,” *Ultrasound Med. Biol.*, vol. 12, no. 8, pp. 623–31, Aug. 1986.
- [20] C. J. Bruce, C. Pislaru, and J. F. Greenleaf, “Characterization of reperfused infarcted myocardium from high-frequency intracardiac ultrasound imaging using homodyned K distribution,” *IEEE Trans. Ultrason. Ferroelectr. Freq. Control*, vol. 49, no. 11, pp. 1530–1542, Nov. 2002.
- [21] M. L. Oelze, W. D. O’Brien, Jr, J. P. Blue, and J. F. Zachary, “Differentiation and Characterization of Rat Mammary Fibroadenomas and 4T1 Mouse Carcinomas Using Quantitative Ultrasound Imaging,” *IEEE Trans. Med. Imaging*, vol. 23, no. 6, pp. 764–771, Jun. 2004.
- [22] K. Nam, J. A. Zagzebski, and T. J. Hall, “Quantitative assessment of in vivo breast masses using ultrasound attenuation and backscatter.,” *Ultrason. Imaging*, vol. 35, no. 2, pp. 146–61, Apr. 2013.
- [23] L. Sannachi, H. Tadayyon, A. Sadeghi-Naini, W. Tran, S. Gandhi, F. Wright, M. Oelze, and G. Czarnota, “Non-invasive evaluation of breast cancer response to chemotherapy using quantitative ultrasonic backscatter parameters.,” *Med. Image Anal.*, vol. 20, no. 1, pp. 224–236, Nov. 2014.
- [24] H. Tadayyon, A. Sadeghi-Naini, L. Wirtzfeld, F. C. Wright, and G. Czarnota, “Quantitative ultrasound characterization of locally advanced breast cancer by estimation of its scatterer properties.,” *Med. Phys.*, vol. 41, no. 1, p. 012903, Jan. 2014.

- [25] B. Banihashemi, R. Vlad, B. Debeljevic, A. Giles, M. C. Kolios, and G. J. Czarnota, “Ultrasound imaging of apoptosis in tumor response: novel preclinical monitoring of photodynamic therapy effects.,” *Cancer Res.*, vol. 68, no. 20, pp. 8590–6, Oct. 2008.
- [26] R. M. Vlad, S. Brand, A. Giles, M. C. Kolios, and G. J. Czarnota, “Quantitative ultrasound characterization of responses to radiotherapy in cancer mouse models.,” *Clin. cancer Res. an Off. J. Am. Assoc. Cancer Res.*, vol. 15, no. 6, pp. 2067–75, Mar. 2009.
- [27] A. Sadeghi-Naini, O. Falou, H. Tadayyon, A. Al-Mahrouki, W. Tran, N. Papanicolau, M. C. Kolios, and G. J. Czarnota, “Conventional Frequency Ultrasonic Biomarkers of Cancer Treatment Response In Vivo,” *Transl. Oncol.*, vol. 6, no. 3, pp. 234–243, Jun. 2013.
- [28] A. Sadeghi-Naini, N. Papanicolau, O. Falou, J. Zubovits, R. Dent, S. Verma, M. Trudeau, J. F. Boileau, J. Spayne, S. Iradji, E. Sofroni, J. Lee, S. Lemon-Wong, M. Yaffe, M. C. Kolios, and G. J. Czarnota, “Quantitative ultrasound evaluation of tumor cell death response in locally advanced breast cancer patients receiving chemotherapy.,” *Clin. Cancer Res.*, vol. 19, no. 8, pp. 2163–74, Apr. 2013.
- [29] J. J. Faran, “Sound Scattering by Solid Cylinders and Spheres,” *J. Acoust. Soc. Am.*, vol. 23, no. 4, p. 405, Jul. 1951.
- [30] V. C. Anderson, “Sound Scattering from a Fluid Sphere,” *J. Acoust. Soc. Am.*, vol. 22, no. 4, pp. 426–431, Jul. 1950.
- [31] M. F. Insana, R. F. Wagner, D. G. Brown, and T. J. Hall, “Describing small-scale structure in random media using pulse-echo ultrasound,” *J. Acoust. Soc. Am.*, vol. 87, no. 1, pp. 179–192, Jan. 1990.
- [32] J. J. Anderson, M. Herd, M. R. King, A. Haak, Z. T. Hafez, J. Song, M. L. Oelze, E. L. Madsen, J. Zagzebski, W. D. O’Brien, and T. J. Hall, “Interlaboratory comparison of backscatter coefficient estimates for tissue-mimicking phantoms.,” *Ultrason. Imaging*, vol. 32, no. 1, pp. 48–64, Jan. 2010.
- [33] R. S. C. Cobbold, *Foundations of Biomedical Ultrasound*. Oxford University Press, 2006.

- [34] M. F. Insana and T. J. Hall, “Parametric ultrasound imaging from backscatter coefficient measurements: Image formation and interpretation,” *Ultrason. Imaging*, vol. 12, no. 4, pp. 245–267, Oct. 1990.
- [35] L. X. Yao, J. A. Zagzebski, and E. L. Madsen, “Backscatter coefficient measurements using a reference phantom to extract depth-dependent instrumentation factors,” *Ultrason. Imaging*, vol. 12, no. 1, pp. 58–70, 1990.
- [36] A. Sadeghi-Naini, N. Papanicolau, O. Falou, H. Tadayyon, J. Lee, J. Zubovits, A. Sadeghian, R. Karshafian, A. Al-Mahrouki, A. Giles, M. C. Kolios, and G. J. Czarnota, “Low-frequency quantitative ultrasound imaging of cell death in vivo.,” *Med. Phys.*, vol. 40, no. 8, p. 082901, Aug. 2013.
- [37] T. Varghese and K. D. Donohue, “Characterization of tissue microstructure scatterer distribution with spectral correlation.,” *Ultrason. Imaging*, vol. 15, no. 3, pp. 238–54, Jul. 1993.
- [38] K. Suzuki, N. Hayashi, Y. Sasaki, M. Kono, A. Kasahara, Y. Imai, H. Fusamoto, and T. Kamada, “Evaluation of structural change in diffuse liver disease with frequency domain analysis of ultrasound.,” *Hepatology*, vol. 17, no. 6, pp. 1041–6, Jun. 1993.
- [39] U. R. Abeyratne and X. Tang, “Ultrasound scatter-spacing based diagnosis of focal diseases of the liver,” *Biomed. Signal Process. Control*, vol. 2, no. 1, pp. 9–15, Jan. 2007.
- [40] C. B. Machado, W. C. A. Pereira, M. Meziri, and P. Laugier, “Characterization of in vitro healthy and pathological human liver tissue periodicity using backscattered ultrasound signals.,” *Ultrasound Med. Biol.*, vol. 32, no. 5, pp. 649–57, May 2006.
- [41] S. M. Kay, *Modern Spectral Estimation-Theory and Application*. Prentice-hall, 1998.
- [42] Y. Bige, Z. Hanfeng, and W. Rong, “Analysis of microstructural alterations of normal and pathological breast tissue in vivo using the AR cepstrum.,” *Ultrasonics*, vol. 44, no. 2, pp. 211–5, Feb. 2006.
- [43] C. Li, N. Duric, P. Littrup, and L. Huang, “In vivo breast sound-speed imaging with ultrasound tomography.,” *Ultrasound Med. Biol.*, vol. 35, no. 10, pp. 1615–28, Oct. 2009.

- [44] F. T. D'Astous and F. S. Foster, "Frequency dependence of ultrasound attenuation and backscatter in breast tissue.," *Ultrasound Med. Biol.*, vol. 12, no. 10, pp. 795–808, Oct. 1986.
- [45] L. R. Taggart, R. E. Baddour, A. Giles, G. J. Czarnota, and M. C. Kolios, "Ultrasonic characterization of whole cells and isolated nuclei.," *Ultrasound Med. Biol.*, vol. 33, no. 3, pp. 389–401, Mar. 2007.
- [46] Y. Labyed, T. a Bigelow, and B. L. McFarlin, "Estimate of the attenuation coefficient using a clinical array transducer for the detection of cervical ripening in human pregnancy.," *Ultrasonics*, vol. 51, no. 1, pp. 34–9, Jan. 2011.
- [47] M. L. Oelze and W. D. O'Brien, Jr, "Frequency-dependent attenuation-compensation functions for ultrasonic signals backscattered from random media," *J. Acoust. Soc. Am.*, vol. 111, no. 5, pt1, p. 2308, 2002.
- [48] R. M. Haralick, K. Shanmugam, and I. Dinstein, "Textural Features for Image Classification," *IEEE Trans. Syst. Man. Cybern.*, vol. SMC-3, no. 6, pp. 610–621, Nov. 1973.
- [49] "Graycomatrix: Create gray-level co-occurrence matrix from image," 2015. [Online]. Available: <http://www.mathworks.com/help/images/ref/graycomatrix.html>.
- [50] R. M. Vlad, N. M. Alajez, A. Giles, M. C. Kolios, and G. J. Czarnota, "Quantitative ultrasound characterization of cancer radiotherapy effects in vitro.," *Int. J. Radiat. Oncol. Biol. Phys.*, vol. 72, no. 4, pp. 1236–43, Nov. 2008.
- [51] J. W. Hunt, A. E. Worthington, A. Xuan, M. C. Kolios, G. J. Czarnota, and M. D. Sherar, "A model based upon pseudo regular spacing of cells combined with the randomisation of the nuclei can explain the significant changes in high-frequency ultrasound signals during apoptosis.," *Ultrasound Med. Biol.*, vol. 28, no. 2, pp. 217–26, Feb. 2002.
- [52] M. C. Kolios, G. J. Czarnota, M. Lee, J. W. Hunt, and M. D. Sherar, "Ultrasonic spectral parameter characterization of apoptosis.," *Ultrasound Med. Biol.*, vol. 28, no. 5, pp. 589–97, May 2002.

- [53] G. J. Czarnota, M. C. Kolios, H. Vaziri, S. Benchimol, F. P. Ottensmeyer, M. D. Sherar, and J. W. Hunt, “Ultrasonic biomicroscopy of viable, dead and apoptotic cells.,” *Ultrasound Med. Biol.*, vol. 23, no. 6, pp. 961–5, Jan. 1997.
- [54] G. J. Czarnota, M. C. Kolios, J. Abraham, M. Portnoy, F. P. Ottensmeyer, J. W. Hunt, and M. D. Sherar, “Ultrasound imaging of apoptosis: high-resolution noninvasive monitoring of programmed cell death in vitro, in situ and in vivo,” *Br. J. Cancer*, vol. 819, no. 3, pp. 520–527, Oct. 1999.
- [55] S. Brand, E. C. Weiss, R. M. Lemor, and M. C. Kolios, “High frequency ultrasound tissue characterization and acoustic microscopy of intracellular changes.,” *Ultrasound Med. Biol.*, vol. 34, no. 9, pp. 1396–407, Sep. 2008.
- [56] R. H. Silverman, R. Folberg, M. J. Rondeau, H. C. Boldt, H. O. Lloyd, X. Chen, F. L. Lizzi, T. A. Weingeist, and D. J. Coleman, “Spectral parameter imaging for detection of prognostically significant histologic features in uveal melanoma.,” *Ultrasound Med. Biol.*, vol. 29, no. 7, pp. 951–9, Jul. 2003.
- [57] M. L. Oelze and W. D. O’Brien, “Application of three scattering models to characterization of solid tumors in mice.,” *Ultrason. Imaging*, vol. 28, no. 2, pp. 83–96, Apr. 2006.
- [58] G. J. Czarnota and M. C. Kolios, “Ultrasound imaging of apoptosis: role of chromatin structure and membrane configuration,” in *Proc Am Inst Ultra Med Annu Meeting*, 2001, p. 117.
- [59] K. A. Topp, J. F. Zachary, and W. D. O’Brien, Jr, “Quantifying B-mode images of in vivo rat mammary tumors by the frequency dependence of backscatter,” *J. ultrasound Med.*, vol. 20, no. 6, pp. 605–612, Jun. 2001.
- [60] J. J. Anderson, M.-T. Herd, M. R. King, A. Haak, Z. T. Hafez, J. Song, M. L. Oelze, E. L. Madsen, J. a Zagzebski, W. D. O’Brien, and T. J. Hall, “Interlaboratory comparison of backscatter coefficient estimates for tissue-mimicking phantoms.,” *Ultrason. Imaging*, vol. 32, no. 1, pp. 48–64, Jan. 2010.

- [61] K. Shung, *Diagnostic ultrasound: Imaging and blood flow measurements*. CRC Press, 2005.
- [62] S. Brand, B. Solanki, D. B. Foster, G. J. Czarnota, and M. C. Kolios, “Monitoring of cell death in epithelial cells using high frequency ultrasound spectroscopy.,” *Ultrasound Med. Biol.*, vol. 35, no. 3, pp. 482–93, Mar. 2009.
- [63] T. M. Kolb, J. Lichy, and J. H. Newhouse, “Comparison of the Performance of Screening Mammography , Physical Examination , and Breast US and Evaluation of Factors that Influence Them : An Analysis of 27,825 Patient Evaluations,” *Radiology*, vol. 225, no. 1, pp. 165–175, 2002.
- [64] W. A. Berg, J. D. Blume, J. B. Cormack, E. B. Mendelson, D. Lehrer, M. Böhm-Vélez, E. D. Pisano, R. A. Jong, W. P. Evans, M. J. Morton, M. C. Mahoney, L. H. Larsen, R. G. Barr, D. M. Farria, H. S. Marques, K. Boparai, and I. A. 6666, “Combined screening with ultrasound and mammography vs mammography alone in women at elevated risk of breast cancer: Results of the First-Year Screen in ACRIN 6666,” *JAMA*, vol. 299, no. 18, pp. 2151–63, May 2008.
- [65] A. V. Alvarenga, W. C. A. Pereira, A. F. C. Infantosi, and C. M. Azevedo, “Complexity curve and grey level co-occurrence matrix in the texture evaluation of breast tumor on ultrasound images,” *Med. Phys.*, vol. 34, no. 2, pp. 379–387, Feb. 2007.
- [66] Y.-Y. Liao, P.-H. Tsui, C.-H. Li, K.-J. Chang, W.-H. Kuo, C.-C. Chang, and C.-K. Yeh, “Classification of scattering media within benign and malignant breast tumors based on ultrasound texture-feature-based and Nakagami-parameter images,” *Med. Phys.*, vol. 38, no. 4, pp. 2198–207, 2011.
- [67] W. J. Krzanowski, *Principles of Multivariate Analysis: A User’s Perspective*. New York: Oxford University Press, 1988.
- [68] E. L. Madsen, J. A. Zagzebski, R. A. Banjavie, and R. E. Jutila, “Tissue mimicking materials for ultrasound phantoms.,” *Med. Phys.*, vol. 5, no. 5, pp. 391–4, 1978.

- [69] S. Tadjudin and D. A. Landgrebe, “Covariance estimation for limited training samples,” in *IGARSS '98. Sensing and Managing the Environment. 1998 IEEE International Geoscience and Remote Sensing. Symposium Proceedings. (Cat. No.98CH36174)*, 1998, vol. 5, pp. 2688–2690 vol.5.
- [70] H. Nasief, I. Rosado-Mendez, J. Zagzebski, and T. Hall, “Quantitative Ultrasound as an Aid to Differentiate Benign From Malignant Breast Masses,” in *AIUM (American Institute of Ultrasound in Medicine) Annual Convention*, 2013, p. S62.
- [71] E. Franceschini, R. Guillermin, F. Tourniaire, S. Roffino, E. Lamy, and J.-F. Landrier, “Structure factor model for understanding the measured backscatter coefficients from concentrated cell pellet biophantoms.,” *J. Acoust. Soc. Am.*, vol. 135, no. 6, pp. 3620–31, 2014.
- [72] H. Tadayyon, L. Sannachi, and G. J. Czarnota, “Quantitative ultrasound monitoring of breast tumor response to chemotherapy by analysis of frequency-dependent attenuation and backscattered power,” in *SPIE Medical Imaging*, 2014, p. 904009.
- [73] S. H. Giordano, “Update on locally advanced breast cancer,” *The Oncol.*, vol. 8, no. 6, pp. 521–530, Jan. 2003.
- [74] L. X. Yao, J. A. Zagzebski, and E. L. Madsen, “Backscatter Coefficient Measurements Using a Reference Phantom to Extract Depth-Dependent Instrumentation Factors,” *Ultrason. Imaging*, vol. 12, no. 1, pp. 58–70, Jan. 1990.
- [75] L. L. Fellingham and F. G. Sommer, “Ultrasonic Characterization of Tissue Structure in the In Vivo Human Liver and Spleen,” *IEEE Trans. Sonics Ultrason.*, vol. SU-31, no. 4, pp. 418 – 428, 1984.
- [76] K. A. Wear, R. F. Wagner, and B. S. Garra, “High resolution ultrasonic backscatter coefficient estimation based on autoregressive spectral estimation using Burg’s algorithm.,” *IEEE Trans. Med. Imaging*, vol. 13, no. 3, pp. 500–7, Jan. 1994.
- [77] T. Cover and P. Hart, “Nearest neighbor pattern classification,” *IEEE Trans. Inf. Theory*, vol. 13, no. 1, pp. 21–27, Jan. 1967.

- [78] R. Rajan, A. Poniecka, T. L. Smith, Y. Yang, D. Frye, L. Pusztai, D. J. Fiterman, E. Gal-Gombos, G. Whitman, R. Rouzier, M. Green, H. Kuerer, A. U. Buzdar, G. N. Hortobagyi, and W. F. Symmans, “Change in tumor cellularity of breast carcinoma after neoadjuvant chemotherapy as a variable in the pathologic assessment of response.,” *Cancer*, vol. 100, no. 7, pp. 1365–73, Apr. 2004.
- [79] A. K. Jain, R. P. W. Duin, and J. Mao, “Statistical pattern recognition: a review,” *IEEE Trans. Pattern Anal. Mach. Intell.*, vol. 22, no. 1, pp. 4–37, 2000.
- [80] R. Peto and J. Peto, “Asymptotically Efficient Rank Invariant Test Procedures,” *J. R. Stat. Soc. Ser. A*, vol. 135, no. 2, p. 185, 1972.
- [81] S.-J. Dawson, D. W. Y. Tsui, M. Murtaza, H. Biggs, O. M. Rueda, S.-F. Chin, M. J. Dunning, D. Gale, T. Forshaw, B. Mahler-Araujo, S. Rajan, S. Humphray, J. Becq, D. Halsall, M. Wallis, D. Bentley, C. Caldas, and N. Rosenfeld, “Analysis of circulating tumor DNA to monitor metastatic breast cancer.,” *N. Engl. J. Med.*, vol. 368, no. 13, pp. 1199–209, Mar. 2013.
- [82] G. von Minckwitz, J. U. Blohmer, S. D. Costa, C. Denkert, H. Eidtmann, W. Eiermann, B. Gerber, C. Hanusch, J. Hilfrich, J. Huober, C. Jackisch, M. Kaufmann, S. Kümmel, S. Paepke, A. Schneeweiss, M. Untch, D. M. Zahm, K. Mehta, and S. Loibl, “Response-guided neoadjuvant chemotherapy for breast cancer.,” *J. Clin. Oncol.*, vol. 31, no. 29, pp. 3623–30, Oct. 2013.
- [83] T. Hastie, R. Tibshirani, and J. Friedman, *The Elements of Statistical Learning: Data Mining, Inference, and Prediction*, 2nd ed. Springer, 2011.
- [84] D. P. Petrylak, C. M. Tangen, M. H. A. Hussain, P. N. Lara, J. A. Jones, M. E. Taplin, P. A. Burch, D. Berry, C. Moinpour, M. Kohli, M. C. Benson, E. J. Small, D. Raghavan, and E. D. Crawford, “Docetaxel and estramustine compared with mitoxantrone and prednisone for advanced refractory prostate cancer.,” *N. Engl. J. Med.*, vol. 351, no. 15, pp. 1513–20, Oct. 2004.

- [85] D. T. Miyamoto, L. V Sequist, and R. J. Lee, “Circulating tumour cells-monitoring treatment response in prostate cancer.,” *Nat. Rev. Clin. Oncol.*, vol. 11, no. 7, pp. 401–12, Jul. 2014.
- [86] E. J. Feleppa, “Ultrasonic tissue-type imaging of the prostate: implications for biopsy and treatment guidance.,” *Cancer Biomark.*, vol. 4, no. 4–5, pp. 201–12, Jan. 2008.
- [87] P. Coupé, P. Hellier, X. Morandi, and C. Barillot, “Probe trajectory interpolation for 3D reconstruction of freehand ultrasound,” *Med. Image Anal.*, vol. 11, no. 6, pp. 604–15, Dec. 2007.
- [88] B. Liu, H. D. Cheng, J. Huang, J. Liu, and T. XIanglong, “Fully automatic and segmentation-robust classification of breast tumors based on local texture analysis,” *Proc. 11th Jt. Conf. Inf. Sci.*, pp. 1–7, 2008.
- [89] J. Shan, H. D. Cheng, and Y. Wang, “A novel segmentation method for breast ultrasound images based on neutrosophic l-means clustering.,” *Med. Phys.*, vol. 39, no. 9, pp. 5669–82, Sep. 2012.
- [90] R. Hickling, “Analysis of Echoes from a Solid Elastic Sphere in Water,” *J. Acoust. Soc. Am.*, vol. 34, no. 10, pp. 1582–1592, 1962.
- [91] T. A. Bigelow, B. L. McFarlin, W. D. O’Brien, and M. L. Oelze, “In vivo ultrasonic attenuation slope estimates for detecting cervical ripening in rats: Preliminary results,” *J Acoust Soc Am.*, vol. 123(3), no. 3, pp. 1794–1800, Mar. 2008.
- [92] Y. Labyed and T. a Bigelow, “A theoretical comparison of attenuation measurement techniques from backscattered ultrasound echoes.,” *J. Acoust. Soc. Am.*, vol. 129, no. 4, pp. 2316–24, Apr. 2011.
- [93] D. P. Hruska and M. L. Oelze, “Improved parameter estimates based on the homodyned K distribution.,” *IEEE Trans. Ultrason. Ferroelectr. Freq. Control*, vol. 56, no. 11, pp. 2471–81, Nov. 2009.